An experimental and numerical investigation of the hydrodynamics of the ducted system of a "Van Rompay Turbine"

with the goal to capture energy from the current of an ocean, river, estuary or similar.

Master Thesis
M.N. van Ruiten
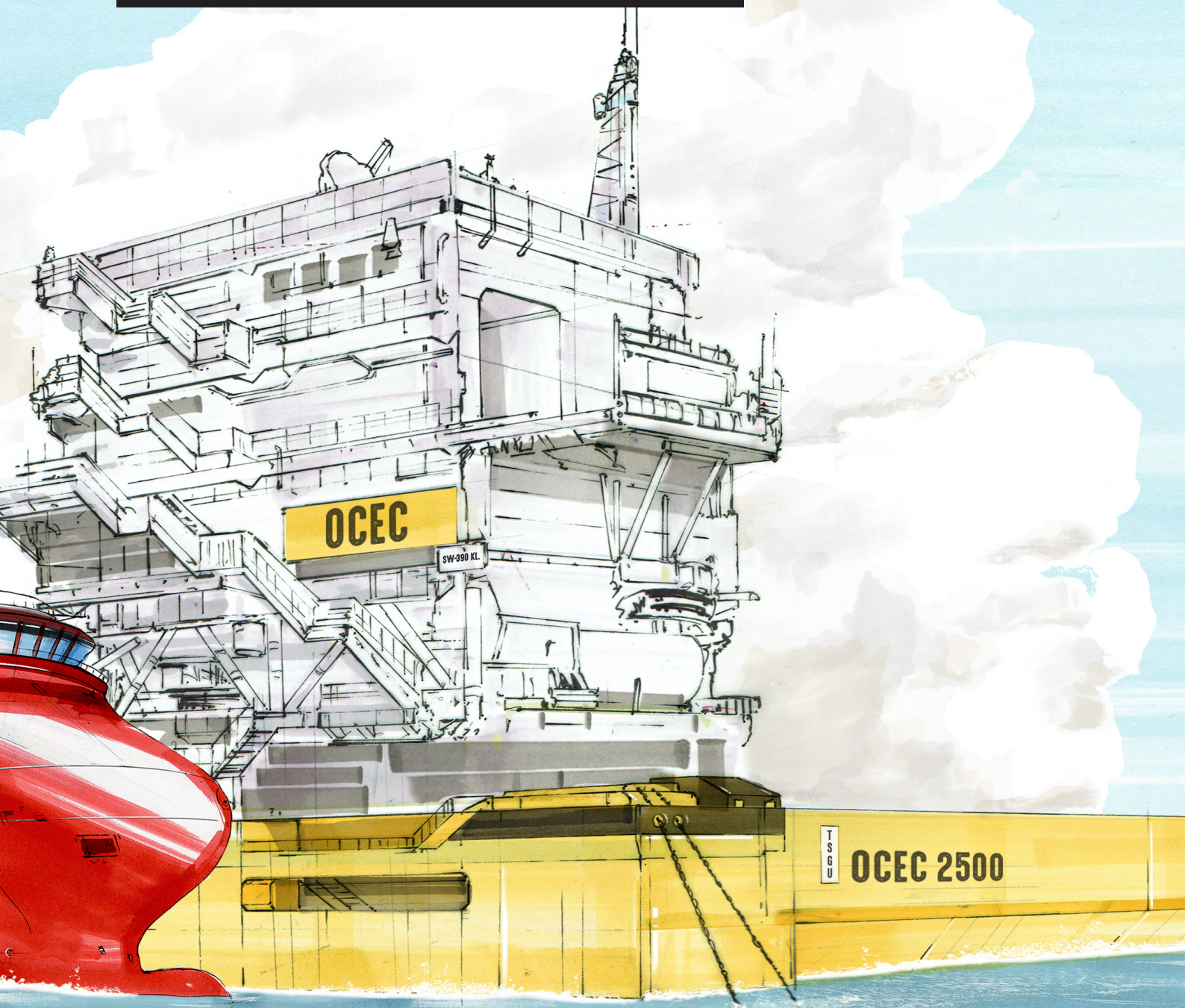
An experimental and numerical investigation of the hydrodynamics of the ducted system of a "Van Rompay Turbine"

with the goal to capture energy from the current of an ocean, river, estuary or similar.

Master Thesis

by

M.N. van Ruiten

in partial fulfillment of the requirements for the degree of

Master of Science
in Hydraulic Engineering

at the Delft University of Technology

Student number: 4454413
Date: August 25, 2021
Thesis committee: Prof. Dr. Ir. M. van Koningsveld,   Delft University of Technology, Chairman
                   Dr. Ir. A. Jarquin Laguna,   Delft University of Technology, Supervisor
                   Dr. Ir. J. P. Aguilar-López   Delft University of Technology, Co-supervisor
                   Boud van Rompay   CEO and Founder of Hydrex n.v.

Preface

This research focuses on an experimental and numerical investigation of the hydrodynamics of the ducted system of a Van Rompay Turbine with the goal to capture energy from the current of an ocean, river, estuary or similar. The project has been carried out to obtain the degree of Master of Science in Hydraulic Engineering from the Delft University of Technology.

In addition to the academic aspect of the project, I learned a lot about field experiments and how to organise them. Arranging reliable measuring instruments, managing the building of the prototype and finding a suitable test location were part of the organisational work. Some setbacks on the way to completing my graduation project had to be overcome. For example, the last minute rejection of the 3ME faculty at the TU Delft to test the prototype in the towing tank and delays in the planning due to ongoing jobs abroad within the company.

First and foremost, to my first supervisor Antonio Jarquin Laguna, thank you for all your efforts and support throughout this project. I am truly grateful for your willingness to take the role of first supervisor and provide me with excellent guidance and knowledge of the field.

Secondly, I would also like to express my gratitude to my second supervisor Juan Pablo Aguilar-López for helping me on a regular basis with the CFD simulations. Your positive attitudes and knowledge helped me a lot during this project. Thirdly, I would like to thank my chair, Mark van Koningsveld, to help me seeing things in an additional perspective and for further improving the quality of the work.

Lastly, I would like to thank Boud Van Rompay, CEO and founder of Hydrex, who made this project possible and helping me navigate through multiple hurdles along the way. I am truly grateful for your willingness to take my frequent calls, your valuable advice, and the many discussions about this project. I also want to thank the Hydrex team for their fantastic assistance during the experiments and for their work building the prototype. It was a pleasure to work with you.

<div align="right">

Martijn van Ruiten
Rotterdam, August 25, 2021

</div>

Abstract

Hydrokinetic energy is an environmentally friendly source of electricity and it has the advantage to be more predictable compared to other renewables. According to IRENA (2020), the capacity of converting hydrokinetic energy into electricity is expected to increase in the coming decades as many concepts are in the pipeline. One of these hydrokinetic energy concepts is the patented Van Rompay Turbine. The Van Rompay Turbine consists of a duct, an air chamber and a paddlewheel. The duct, which is based on a Venturi working principle, consists of a converging inlet, a throat and a diverging outlet. Above the throat, an air chamber is present to provide an air environment to reduce resistance for the paddlewheel. The goal of this research was to experimentally and numerically test a prototype (L:4.05m x W:1.17m x H:1.17m) of the ducted system.

Three inclination angles: 21°, 26° & 31°, for the converging inflow and diverging outflow segment were tested, referred to as the small, medium and large ramp size, respectively, to determine which size represents the lowest energy losses in the system. The small in -and outflow ramp represents the lowest energy losses compared to the medium and large ramp. Subsequently, on the small inflow ramp, five designs were tested, referred to as the straight, curved and the high, mid & low frequency waved designs; to again determine which design represents the lowest energy losses. Roughed waved wall designs are streamwise wavy walls with each a different wavelength and amplitude. The small ramp with a high, mid & low frequency waved design results in the lowest energy losses in comparison to the straight and curved designs for inlet velocities between 0 m/s and 0.4 m/s. For inlet velocities between 0.4 m/s and 0.5 m/s, the small ramp with a curved design represents the lowest energy losses in comparison to the straight and high, mid & low frequency waved designs.

The data points acquired during the experiments were scattered due to external factors increasing the uncertainty of the measurements. Besides this, the experimental investigations were tested over an inlet velocity between 0 m/s and 0.5 m/s, limiting the data analysis. For this reason, several CFD simulations were carried out to acquire data with no influence of external factors and to investigate the system for higher velocities. The CFD simulations were executed for the five different inflow ramp designs with an in -and outflow inclination angle of 21°. The CFD model solves the Reynolds-averaged Navier–Stokes (RANS) equations with a k-ϵ turbulence closure model. Based on these CFD simulations, the best performing design for the inflow ramp in terms of the lowest energy losses for an inlet flow velocity between 0 m/s and 0.75 m/s is the high frequency waved design. Regarding velocities between 0.75 m/s and 3 m/s, the curved design represents the lowest energy losses compared to the straight and high, mid & low frequency waved designs. After scaling up the ducted system in CFD simulations with a factor 2 and 10, the flow velocity reduces as there are more energy losses in the system. However, as larger systems have a marginal lower specific surface of contact between the water and the duct, an increase in available flow power could be found. The extent to which the ducted system can be scaled up depends on the space restrictions at the specific location. Besides, the minimal required inflow area of the free water flow should be met. It can therefore be concluded that the potentially available energy for generation also depends the location where the Van Rompay will be deployed.

Experiments need to be performed to study the hydrodynamic impact and the hydrodynamic efficiency of the paddlewheel to determine the power performance output and thus its potential value for the hydrokinetic energy market. It is recommended for future research to test the prototype at higher velocities and to test the prototype in a laboratory facility as these offer the benefits of controlled testing.

Contents

List of Figures

List of Tables

Nomenclature

Acronyms and Abbreviations

CFD   Computational Fluid Dynamics

DB   Bi-directional

IRENA   International Renewable Energy Agency

ITTC   International Towing Tank Conference

kW   Kilo Watt

Re   Reynolds Number

RMS   Root-mean-square

RPM   Rotations Per Minute

TKE   Turbulence Kinetic Energy

TRL   Technology Readiness Levels

TSR   Tip Speed Ratio [ωR/U]

UD   Unidirectional

Greek Symbols

ϵ Turbulence Dissipation Rate [m^2/s^3]

η Efficiency [%]

λ Wave Length [m]

μ Dynamic viscosity [Pa·s]

μ_T Turbulent viscosity [(N/m2)·s]

ν Kinematic Viscosity [m^2/s]

ω Angular Velocity [1/s]

ρ Density [kg/m3]

σ Turbulent Dissipation Rate [m^2/s^3]

Latin Symbols

$\hat{H}_j$ Enthalpy [J/kg]

A_s Swept Area of the Turbine [m^2]

A_1 Cross-section Inlet [m^2]

A_2 Cross-section Inside Turbine [m^2]

B Width [m]

C_P Power Coefficient [-]

D Height inlet Venturi System [m]

d Height throat Venturi System [m]

$E_{\Delta U}$ Work gained or lost to the system [J/kg]

E_k Kinetic energy [J/kg]

E_P Potential energy [J/kg]

F Volume force field [N/m^3]

H Wave Height [m]

i Immersed Depth [m]

k Turbulence Kinetic Energy [m^2/s^2]

L Characteristic Length [m]

l Shear rate viscosity [Pa·s]

m_j Mass [kg]

n Number of rotations [-]

P Power [W]

p Kinematic Pressure [N/m^2]

P_{water} Water Flow Power [W]

Q Heat rate [J]

R Rotor Radius [m]

r Torque Arm [m]

T Torque developed by turbine shaft [Nm]

t Blade Thickness [m]

V Volume [m^3]

v Flow velocity [m/s]

v_{Blade} Blade Velocity [m/s]

v_1 Inlet Flow velocity [m/s]

v_2 Flow velocity Inside Turbine [m/s]

W_s Rate of work done by the system [J]

1

Introduction

1.1. Global Energy Challenges

Energy is the power behind humanity. It improves our quality of life, and it is essential to economic and social development. However, much of the world's energy has a negative impact on the environment (Guimarães, 2021). Global energy demand is expected to increase substantially in the coming decades. This is mainly due to the projected growth in world population and the economic and industrial growth of developing countries such as China and India (Zohuri, 2020). The U.S. Energy Information Administration projects a world energy consumption growth of nearly 50% between 2018 and 2050 (IEA, 2020b).

Another challenge our planet is facing is to provide universal access to electricity. In 2019, the number of people without access to electricity was estimated at 770 million (IEA, 2020c). According to the International Energy Agency (2020a), this number is mostly caused by the developing areas in the world. These people are in need of the right solution to get easy access to energy to increase their living standards. Worldwide access to energy would benefit the economy, health and academic prospects. Micropower plants that can be installed in rural and underdeveloped areas based on renewable resources are a promising solution for this challenge (Blodgett et al., 2017).

1.2. The Energy Market

The primary energy sources have evolved over the past decades. From wood and other forms of natural biomass to coal for the steam engines and later on, petroleum and its by-products became the most prominent source of energy. Over time natural gas has become an important source as well. Oil, coal, and natural gas are still in use today and are the main contributors to the worldwide energy demand. More than 80% of the total energy supply is supplied by these sources (IEA, 2019).

Other prominent contributors to the global energy supply are biomass, nuclear energy and hydroelectric energy. Wind energy is winning ground over the last few years. Solar does the same, yet it has a less significant growth rate (IEA, 2020a). Tidal and wave energy do not impact the global energy supply up to this present day. The share is negligible as only 10.6MW operational capacity is installed (IRENA, 2020). This is displayed in Figure 1.1. Note that 'Other renewables' include geothermal, biomass, wave and tidal energy.
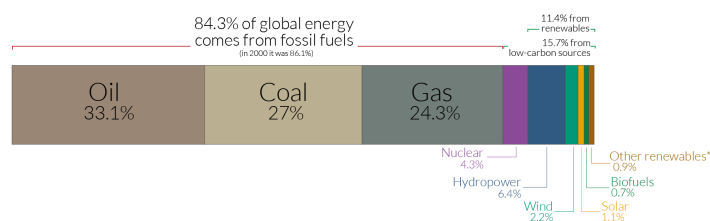
Figure 1.1: Global primary energy consumption by energy source (Ritchie, 2014; BP, 2020)

1

Fossil fuels like coal, oil and natural gas, cause more harm to our environment than renewable energy sources (UCS, 2008). However, renewable energy sources also have a negative impact on our environment (Francis and Peters, 1980; Saidur et al., 2011).

A sustainable and cost-effective solution for tackling the global energy challenges needs to be developed and cannot be entirely answered by these energy sources so far. Hydropower plants, by building big dams in the rivers, appear to be an exciting option to satisfy the challenges of meeting the increasing energy demand and providing universal access to electricity based on a renewable energy source.

1.3. Hydropower

Hydropower is the most contributory renewable energy source worldwide (Laghari et al., 2013). Regrettably, this energy source comes, similar to the other energy sources, with multiple environmental disadvantages. This is mainly due to building large dams that cause a big reservoir upstream and floods the adjacent areas. This poses a threat to inhabitants located close to the dam. These dams also involve a risk of dam failure with all possible consequences (Askari et al., 2015). Wildlife needs to survive the flooding, and when it does, the animals need to adapt to a new situation, questioning whether this wildlife has the skills and the know-how to do so. Building the dam also results in interruption of the longitudinal connectivity of a river, it changes the water discharge regime, and it will change the sediment transport (Kallis and Butler, 2001). Besides, not all rivers are suitable for implementing this. Moreover, the hydropower station and the dams are large and complex constructions, making them very expensive.

Hoover dam is one of the most famous hydropower plants worldwide. If the water level in the reservoir is low, consequently less energy is produced. Lake Mead, which is located upstream of the Hoover dam, experiences low waters for a long time (J. Robbins, 2019). In April 2020, Lake Mead had a capacity of 42.97% (US Bureau of Reclamation, 2020). Figure 1.2 shows dramatically how far water levels have dropped during the record low water levels in 2016. A High water level is required for energy production. In the case of energy production, water levels will drop further and subsequently, the dam will have less energy potential (Rosen, 2012). When they decide to produce energy, it takes a long time before the reservoir is filled again. Therefore, the dam is not used at full operation, and this results in lower energy production.

Figure 1.2: Drought in lake Mead - By T. Wood (J. Robbins, 2019)

1.4. Hydrokinetic Energy

An underwater turbine is already known, whereby a screw propeller or rotor is placed underwater. The kinetic energy, caused by currents that occur in oceans and rivers, is converted into electricity through a transformation of the water momentum into a mechanical motion, typically rotational or oscillatory (ITTC, 2014; Hydro Quebec, 2015). This method of energy production is called hydrokinetic energy. Hydrokinetic is a combination of hydro- + kinetic, which means the movement of water.

Such known installations present the disadvantage that the turbines and the generators connected to them must be carefully sealed to prevent the harmful effects of exposure to the water. This not only makes the

installation expensive but also difficult to maintain. Moreover, the rotating blades of the screw propeller and rotor form a hazard to marine life.

Nevertheless, hydrokinetic energy is more environmental friendly than conventional hydropower plants, and this market is therefore winning ground. Hydrokinetic energy has the advantage to be predictable compared to other renewable energy systems. This can be seen as a benefit which makes hydrokinetic energy a potential valuable renewable energy for the energy market.

Hydrokinetic energy systems leave the rivers and oceans unharmed, and it could provide energy on a big scale for billions of people worldwide. This could contribute to the industrialisation of countries for meeting the non-fossil fuel targets, for satisfying the electricity demand and for new market opportunities (Paish, 2002).

On a small scale, it could provide electricity for all human beings as it could be installed on a small scale in rural and underdeveloped areas or remote industrial sites where rivers or ocean currents are available. This could result in the establishment of many small river hydroelectric power stations (Quaranta and Revelli, 2018). Akinyemi and Liu (2015) states that these stations in return will create sustainable development, manufacturers and jobs in those areas.

At this moment, 10.6 MW of tidal stream technologies are active and the river current energy market is not yet developed. According to The International Renewable Energy Agency IRENA (2020) this capacity is expected to increase in the coming decades as many concepts are in the pipeline.

1.5. The Opportunity

Mankind is seeking feasible solutions to accelerate the race to a more sustainable future now that fossil fuels are becoming increasingly scarce and harm our planet (Murray et al., 2018). Hydrokinetic energy systems have increased interest in recent years due to their low impact on the environment and their predictability.

In this master thesis, the opportunity was given to test the ducted system of a patented hydrokinetic concept, named the "Van Rompay Turbine". The Van Rompay Turbine consists of a duct, an air chamber and a paddlewheel. The duct, which is based on a Venturi working principle, consists of a converging inlet, a throat and a diverging outlet. Above the throat, an air chamber is present to provide an air environment to reduce resistance for the paddlewheel. The goal of this research was to numerically and experimentally test a prototype (L:4.05m x W:1.17m x H:1.17m) of the ducted system. This concept is based on the patent owned by Van Rompay (2017).

2

Research Scope

Technology Readiness Levels (TRL) give an overview of the stages that need to be accomplished to develop a new technology towards the full economic operation. In Figure 2.1, an overview of the different stages is shown. These levels are more elaborated on in Appendix A.

R&I	Prototype	Demonstration	Pre-Commercial	Industrial Roll-Out
• Labs, tanks & modelling • Component testing & validation	• Single scale devices deployed in relevant sea conditions	• Full-scale devices deployed in relevant/ operational sea conditions	• Small arrays deployed in operational sea conditions	• Full-scale commercial ocean energy power plants or farms in operational conditions
TRL 1-4	**TRL 3-6**	**TRL 5-7**	**TRL 6-8**	**TRL 7-9**

Figure 2.1: TRL levels of an energy device (IRENA, 2020)

The scope of this research is to investigate the hydrodynamics of the ducted system of the Van Rompay Turbine. The ducted system is a component of the Van Rompay Turbine. The entire system, with paddlewheel installed, should be studied in future work.

2.1. Research Objectives

The concept around which the research revolves can be defined as follows:

An experimental and numerical investigation of the ducted system of a Van Rompay Turbine.

This master thesis will be carried out to determine whether the ducted system of the Van Rompay Turbine is a workable concept and it is investigated by comparing venturi configurations to find which configuration represents better in term of the lowest energy losses. The duct, which is based on a Venturi working principle, consists of a converging inlet, a throat and a diverging outlet. Above the throat, an air chamber is present to provide an air environment to reduce resistance for the paddlewheel. No experimental research has been done on this combination of a Venturi system and an air chamber yet.

The Venturi system will ensure that the water flow converges to a smaller area which creates a force on the lowest part of the paddlewheel. The air chamber aims to provide an air environment for a paddlewheel, which entails that its shaft can be located above the waterline. The performance of the paddlewheel and its impact on the hydrodynamic behaviour will not be studied in this master thesis and should be investigated in future research.

The combination of the Venturi ducted system and the air chamber should be assessed during experiments. The ducted system will be examined based on the hydrodynamics inside the system during field experiments

and CFD simulations. Based on the acquired hydrodynamic data of the field experiments and the CFD simulations, the available power to be captured by the turbine can be calculated.

The **main objective** of this research is as follows:

> *Testing a prototype of the **ducted system** of a patented **hydrokinetic** concept named the **Van Rompay Turbine**, which is based on a **Venturi working principle** and consists of an **air chamber**, by carrying out (i) **field experiments** to measure the hydrodynamics and (ii) to model the ducted system in **CFD simulations** to investigate the hydrodynamics for higher velocities and scaled up dimensions.*

The experiments are subdivided into three phases:

1. The first phase covers the field experiments. The flow velocity increase will be measured between the inlet velocity and the velocity inside the ducted system. The flow velocity can be compared when changes have been made to the ramp size and ramp design to identify the better performing Venturi from a set of given configurations in terms of the lowest energy losses in the system.

2. In the second phase, the ducted system will be modelled in CFD software to investigate the hydrodynamics for higher velocities. The flow velocities and the turbulence kinetic energy are calculated.

3. In the third phase, the ducted system will be scaled up in CFD software to investigate the hydrodynamics. Again, the flow velocities and the turbulence kinetic energy are calculated.

2.2. Research Questions

The following research questions ought to be answered to fulfil the research objectives:

2.2.1. Phase 1

1. **What is the impact of the different ramp geometries on the hydrodynamics in the ducted system?**

    (a) What is the impact in flow velocity increase when changing the in –and outflow inclination angle?

    (b) What is the impact in flow velocity increase when changing the inflow ramp design?

2.2.2. Phase 2

2. **How can CFD modelling help to improve the investigation on the hydrodynamics in the ducted system?**

    (a) How can the ducted system be modelled in a CFD simulation?

    (b) How does the CFD model represent the model in the field experiments?

    (c) What is the impact in terms of turbulence when changing the inflow ramp design?

    (d) What is the impact in flow velocity increase when changing the inflow ramp design?

2.2.3. Phase 3

3. **How are the hydrodynamics in the ducted system affected by scaling?**

    (a) What is the impact in terms of turbulence when scaling up the ducted system?

    (b) What is the impact in flow velocity increase when scaling up the ducted system?

    (c) What is the impact in the water flow power available to the turbine when scaling up the ducted system?

2.3. Report structure

Chapter 1 Gives an introduction as it states the energy market problems today and the global energy challenges.

Chapter 2 Introduces the scope of this research according to its research objectives and research questions.

Chapter 3 Discusses the state of the art in the hydrokinetic energy market. Furthermore, it presents the concept of the Van Rompay Turbine.

Chapter 4 Describes the methods used for the field experiments (experimental) and the CFD simulations (numerical).

Chapter 5 Presents the results of the field experiments and the CFD simulations.

Chapter 6 Discusses the considerations of the experiments and provides recommendations for future research.

Chapter 7 Provides the conclusions of the research by answering the research questions.

3

State of the Art

State of the art means the most recent stage in the development of a market, incorporating the newest technology, ideas, and features. In this chapter, the state of the art of the hydrokinetic energy market is discussed. Hydrokinetic is a combination of hydro- + kinetic which means the movement of water. Hydrokinetic energy power is the kinetic energy caused by currents that take place in oceans, rivers, estuaries or similar that is converted into electricity through a transformation of water momentum into a mechanical motion, typically rotational or oscillatory (ITTC, 2014; Hydro Quebec, 2015).

The hydrokinetic energy market has been analysed and an overview has been made of the existing concepts. Firstly, the tidal energy market is discussed in Section 3.1. Subsequently, the river current energy market is discussed in Section 3.2. In Section 3.3, the energy availability is elaborated on and in Section 3.4, the challenges of hydrokinetic energy are discussed. Afterwards, in Section 3.5, the concept of the "Van Rompay turbine" will be extensively explained and it focuses on the state of the art and the improvements of this concept.

3.1. Tidal Current Energy

Tidal currents are caused by the gravitational forces of the sun and the moon and accelerated near constrictions such as islands or inlets. In Appendix B, the phenomena of tidal currents are explained.

3.1.1. Market Analysis

Tidal energy can be divided into two categories: the potential and the kinetic energy category (Zainol et al., 2017). The potential energy can be captured by the so-called tidal barrage approach. The kinetic energy, or tidal currents, can be captured by tidal current turbines. In Appendix C, a figure is shown to give a visualization of the different techniques. In Figure 3.1, the overview of ocean energy deployment is shown. As can be seen, the tidal barrage market has an activated capacity of 521.5 MW and the tidal current market contributes only 10.6MW. The tidal barrage, therefore, has a share of 97.5% of the ocean energy market deployment and the tidal current only has a share of ±0.025% (IRENA, 2020). The tidal current market has therefore a minimal contribution to the ocean energy deployment and lets alone its contribution to the global energy supply.

Figure 3.1: The ocean energy deployment (IRENA, 2020)

Three tidal barrage systems are in use at this moment, but no such power plant has been constructed in the last 10 years. This is due to the low resource potential. Tidal current, on the other hand, has the second-largest

share in ocean technology. This technology is projected to continue growing much faster in the coming years. This can be seen in Figure 3.2.

Figure 3.2: Active and projected cumulative tidal energy capacity (IRENA, 2020)

In the offshore renewable energy strategy of the European Commission, which was released on 19 November 2020, it was stated that they have set objectives as regards ocean energy (Commission, 2020).

- 1-3 GW of wave and tidal energy by 2030 (Commission, 2020)

- 60 GW of wave and tidal energy by 2050 (Commission, 2020)

Among the renewable energy technologies, offshore technologies have the highest potential to scale up due to the tremendous amount of space that is available (Commission, 2020). A worldwide potential of kinetic tidal energy is estimated to be 150 GW (Bryden, 2016). The predicted available energy in some countries is shown in Figure 3.3.
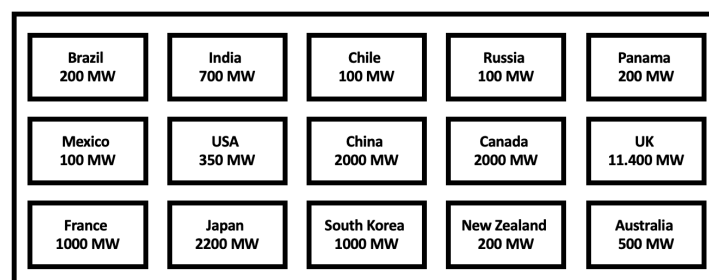
Figure 3.3: The tidal energy potential for different countries - Own Work based on (Bryden, 2016)

It can be concluded that the United Kingdom has the most potential to capture energy from tidal currents. Most of the tidal energy concepts are therefore tested in this area.

At this moment, the installed capacity of tidal current power systems are situated in different stages (IRENA, 2020).

- 7.8 MW: First phase of larger commercial tidal farms

- 1.7 MW: A small share belongs to smaller completed commercial projects

- 1.0 MW: Full-scale demonstration plants

- 0.1 MW: Sub-scale test plants

In Figure 3.4, the global distribution of active current and barrage tidal power plants are shown.
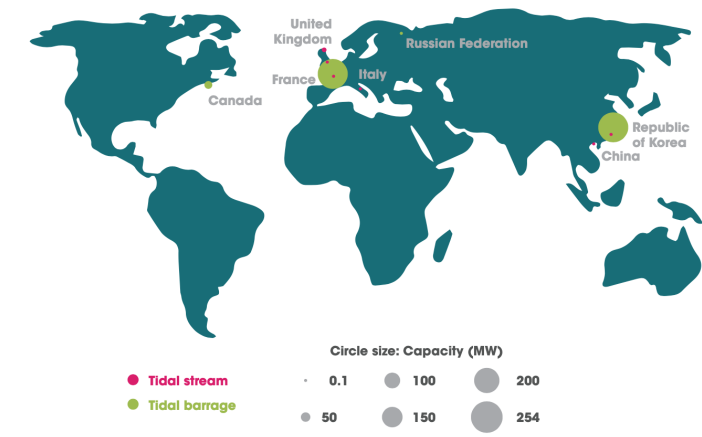
Figure 3.4: The global distribution of active stream and barrage tidal power plants (IRENA, 2020)

3.1.2. Existing Tidal Current Energy Systems
The existing tidal energy turbines are summarized in Table 3.1. Note that the emphasis of this table is to not include past and cumulative deployment. Only currently active projects make it to the table. In Appendix D, the sources are shown.

Table 3.1: Overview of the active tidal current energy turbine systems (IRENA, 2020)

Tidal Current System	Power Output	Type	Location	Year active
Holyhead Deep Tidal Energy	0.50 MW	Oscillatory Device	UK	2019
LHD Tidal Current Phase I b	0.40 MW	Horizontal Axis	China	2016
LHD Tidal Current Phase I a	0.60 MW	Horizontal Axis	China	2016
LHD Tidal Current Phase II a	0.30 MW	Horizontal Axis	China	2018
LHD Tidal Current Phase II b	0.40 MW	Horizontal Axis	China	2018
MeyGen Phase IA Unit I	1.5 MW	Horizontal Axis	UK	2018
MeyGen Phase IA Unit II	4.5 MW	Horizontal Axis	UK	2018
Paimpol- Brehat Tidal Farm	1.0 MW	Ducted Horizontal Axis	France	2019
Seapower GEMSTAR System	0.10 MW	Oscillatory Device	Italy	2019
Shetland Tidal Phase IA	0.10 MW	Horizontal Axis	UK	2016
Shetland Tidal Phase IB	0.10 MW	Horizontal Axis	UK	2016
Shetland Tidal Phase IC	0.10 MW	Horizontal Axis	UK	2017
Uldolmok Tidal Power Plant	1.0 MW	Horizontal Axis	Korea	2009

In Table 3.1, the systems are presented including the power performance output, type of turbine, location and the year of implementation (Rosli and Dimla, 2018). In total, a capacity of 10.6 MW is installed. Various projects have been carried out so far, but none of them is efficient enough to be crowned the winner. MeyGen is the biggest player at this moment with 6 MW active capacity and they are planning to the extent their capacity in the coming years (MeyGen, n.d.). The big question is whether the concept will be profitable and efficient enough to stand. It is clear that the tidal energy concepts with the highest power performance output are based on a horizontal axis turbine.

Looking at the different horizontal axis turbine concepts, many challenges must be overcome before it is efficient and cost-effective enough. The design has a lot of edges and complex connections which are vulnerable to biofouling. Another concern is that the turbine needs to rotate in its own water which causes more friction and therefore involves a lower power output. High installation and maintenance costs are also disadvantages of these turbines. Tidal farms are being installed but the question is whether they will stand and be profitable over the longer term. As the worldwide potential of kinetic tidal energy is estimated to be 150 GW (Bryden, 2016) and the objectives of the European Commission are to reach 1-3 GW of ocean energy technology in 2030 and 60 GW in 2050, the search for more effective concepts is very welcome.

3.2. River Current Energy

Rivers are a constant flowing part of the hydrologic cycle, which makes them ideal for a renewable energy resource (Broslawski et al., 2017). River current energy systems are electromechanical energy converters that convert the kinetic energy of the river flow into energy. Based on the definition of Radkey and Hibbs (1981), river current turbines are 'Low-pressure run-of-the-river ultra-low-head turbines that will operate on the equivalent of less than 0.2m of head'. In Appendix B, the background of river currents is explained.

3.2.1. Market Analysis

Till this moment, no concept is in use for commercial purposes and there is no clear outlook on a specific leading technology. This market is not attractive and efficient enough to conclude it as an effective source of energy yet. Besides, there is no information on the global potential of hydrokinetic energy from rivers. The underlying challenges of system design, operation and economics lack proper understanding (Khan et al., 2008). This market is seeking an efficient concept as the solution to give the answer to this market is nowhere to find at this very moment.

However, to reach universal energy access, small hydrokinetic energy stations could be the solution. Once an efficient and cost-effective concept is found, the market could open. Especially in Africa and Asia, where a lot of rural and underdeveloped areas are located. These stations also create an energy supply to remote industrial sites where rivers or ocean currents are available. Akinyemi and Liu (2015) states that these stations in turn will create sustainable development, manufactures and jobs in those areas.

3.2.2. Existing River Current Energy Systems

A summary of the active concepts is shown in Table 3.2. In Appendix D, the sources are shown. Note that the Technology Readiness Levels and the different turbine types are indicated in the table.

Table 3.2: Overview of river current energy turbine systems (Flambard et al., 2019)

River Current System	Power Output	Rated Velocity	Location	TRL	Turbine Type
DesignPro	60 kW	N/A	Ireland	6	Vertical axis turbine
HydroQuest	40-80 kW	3.1 m/s	France	6	Vertical axis turbine
Aqua Libre	70 kW	3.3 m/s	Austria	6	Horizontal axis turbine
GKinetic	100 kW	N/A	Ireland	8	Vertical axis turbine
Guinard	20 kW	2.5 m/s	France	7	Horizontal Axis Ducted turbine
ORPC	Variable	N/A	USA	7	Horizontal axis turbine

The river current systems do not produce a significant amount of energy to be valuable. As can be seen in the TRL levels in Table 3.2, they are not proven as a "flight-proven" through successful mission operations as the levels do not reach TRL 9.

3.3. Energy Availability

Implementing hydrokinetic power generation systems involve many challenges. The most important challenge is that hydrokinetic energy is not constant over time. It produces an unsteady, non-uniform power output because they are influenced by seasonality. This is the opposite of the conventional gas turbines or coal power plants as they produce a constant power output (Kenyon, H. D., 2017).

Figure 3.5 presents the available power from different renewable energy sources. The available power is shown over the course of a year in the vertical axis and over the course of a day in the horizontal axis, for two different locations. The top row images are closer to the equator whereas the bottom row is further from the equator (Kenyon, H. D., 2017). The colour difference indicates the available energy that could be captured (Widén et al., 2015).

Note that river current systems are not taken into account in Figure 3.5. River flow rates may vary due to weather conditions and seasonality and therefore causes non-constant rates (Kenyon, H. D., 2017).
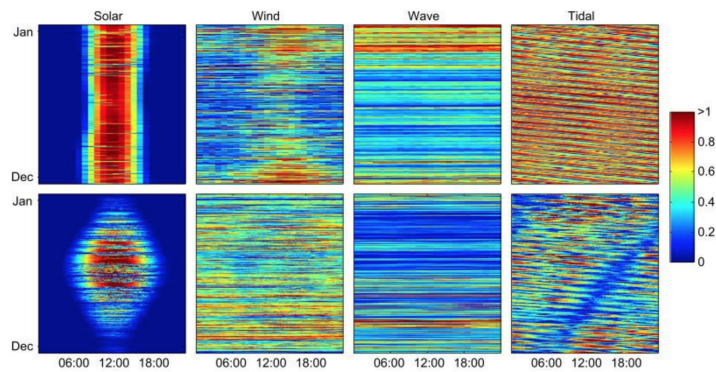
Figure 3.5: Resource Availability Variability Based upon Time of Year and Time of Day (Widén et al., 2015)

The availability of capturing energy from tidal and river currents is not consistent during the day and year, however, it has the advantage to be predictable compared to other renewable energy systems. This can be seen as a huge benefit which makes hydrokinetic energy a renewable energy with a lot of potential. Prospecting tidal energy is no trivial matter. Monitoring, measuring, and performing numerical simulations are used to compute the potential energy that can be harvested in a regional area. Various numerical methods are used to forecast the annual energy production at different sites to ensure successful tidal deployment (Li et al., 2015).

3.4. Challenges of Hydrokinetic Energy

Various systems are in operation to convert hydrokinetic energy into electricity. Most of the research and development of hydrokinetic power generation technology to date has been directed towards tidal current energy systems, and there has been relatively little development for river current energy systems. River current systems face more user conflicts due to the restriction in space and local regulation (Laws and Epps, 2016). What stands out is that almost all active tidal current energy systems are based on a horizontal axis turbine. Submerged horizontal axis turbines are tested extensively, however, the output is not significant enough to be valuable for the global energy market. This is because submerged horizontal axis turbines come with disadvantages that cause low efficiency and high costs over the longer run. The most important disadvantages are the high installation costs and corrosion and biofouling causing high maintenance cost and lower efficiency.

The search for new concepts for tidal and river energy which deal with these disadvantages is therefore very welcome. In the next section, the concept of the Van Rompay Turbine is explained.

3.5. The Van Rompay Turbine Concept

The goal of this master thesis is to carry out an experimental and numerical investigation of the hydrodynamics of the ducted system of a Van Rompay Turbine. In this section, the concept of the Van Rompay turbine will be described in detail. The aim of this concept is to convert hydrokinetic energy into electricity. The Van Rompay Turbine consists of a duct, an air chamber and a paddlewheel. The duct, which is based on a Venturi working principle, consists of a converging inlet, a throat and a diverging outlet. Above the throat, an air chamber is present to provide an air environment to reduce resistance for the paddlewheel.

3.5.1. The Built-Up

Three segments can be identified as can be seen in Figure 3.6.

1. The function of segment 1 is to capture the flow and to converge the water flow. This principle is explained Appendix E.

2. In segment 2, an air chamber is present. The operation of the air chamber is explained in Appendix F. This is the location where the paddlewheel will be installed. Underneath the air chamber, the water flow is present which creates a force on the paddlewheel. Note that the paddlewheel is not installed in this master thesis and should be tested in future research.

3. The function of segment 3 is to diverge the water flow out of the device. This phenomenon is again explained in Appendix E.
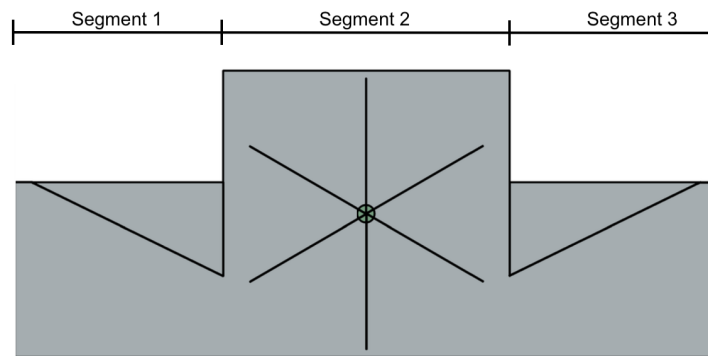
Figure 3.6: Side view of the Van Rompay Turbine - Own work

3.5.2. The underlying idea

The underlying idea of this concept is based on the continuous currents that are present in oceans, rivers, estuaries or similar. These are large amounts of energy that move per unit of time. The Van Rompay turbine consists of a large inflow area which allows a lot of energy to flow into the ducted system. The Venturi ducted system will ensure that the energy is converged to a smaller surface. As a result, a smaller rotor (paddlewheel) is needed inside the ducted system to convert the same amount of energy into electricity (note that losses are present due to turbulence and friction). The water flow entering the ducted system creates a force on the lowest part of the paddlewheel which is optimal for this type of turbine. This ducted system and the paddlewheel could be scaled up so higher volumes can enter the system.

3.5.3. The Design Advantages

The Van Rompay Turbine consist of the following specifications:

- Bi-directional system

- Scalable

- Ducted system

- Air chamber

- Extended rotation area

- Prevention of biofouling in the installations

Bi-directional system

Hydrokinetic energy systems convert the energy of the moving water into electrical energy through a transformation of water momentum into a mechanical motion, typically rotational or oscillatory (ITTC, 2014). The main difference between a tidal current energy system and a river current energy system is the variation in direction of the moving water used for the energy extraction (ITTC, 2014). River current applications involve a unidirectional flow of water while ocean tidal applications involve a bi-directional flow. In the case of a tidally influenced river, the device should be bi-directional as well to anticipate the change of flow direction.

Scalability

The Van Rompay Turbine is scalable. This means that it could be built according to the site requirements. Therefore, it could be used in rivers, oceans, estuaries or similar. In the oceans, the space restrictions are less and therefore large turbines could be installed. This implies that more energy could be captured. Several turbines could be connected to each other creating an array. It should be noted that the inflow area of the free water flow should be sufficient to overcome specific pressures in the ducted system. In Figure 3.7 and 3.8, an impression of the different scales are visible for respectively a river current turbine and an ocean current turbine of the Van Rompay Turbine.

Figure 3.7: River Application

Figure 3.8: Ocean Application

Ducted system

The Van Rompay Turbine consists of a ducted system based on the Venturi principle. In areas where there is a danger of divers and/or floating debris being drawn into the turbine, a grid could be placed on the upstream opening, thus reducing danger to life and danger of damaging or clogging the turbine. The duct shades the turbine itself from direct sunlight, and weed growth will thereby be reduced. Besides, the ducted system causes that a large amount of energy is concentrated into a smaller area so that a smaller, lower-cost turbine can be used for given power output. A disadvantage is that a ducted system causes an increase in drag compared to an open turbine device. The ducted system should also be deployed at a location where the inflow area of the free water flow is above the minimal required inflow area to overcome specific pressures inside the ducted system.

The side view of the Venturi ducted system can be seen in Figure 3.9.
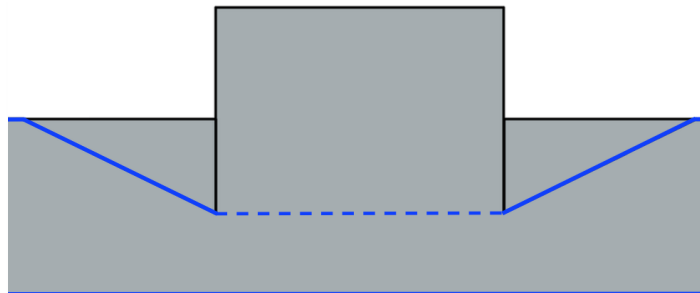
Figure 3.9: Side view of the ducted system of the Van Rompay Turbine - Own work

For the Venturi ducted system, the theoretical limit depends on:

- The pressure difference that is caused by narrowing the inflow segment.

- The volumetric flow through the Venturi ducted system.

- The design and the dimensions of the Venturi ducted system.

Venturi ducted systems are based on Bernoulli's equation. The theoretical background for converging and diverging flow can be found in Appendix E.

Based on prior literature, an improvement of the performance of the horizontal axial turbine in a ducted system is concluded (Kirke, 2003; Shives and Crawford, 2010a; Khunthongjan and Janyalertadun, 2012; Im et al., 2020). Normally, the Betz limit is present which means that for horizontal axial turbines without a ducted system, an upper limit of 59.3% efficiency is present. For a well designed ducted system, the so-called Betz limit is not applicable. In this way, the power output is higher as the efficiency of the turbine increases.

Paddlewheel Turbine

The paddlewheel turbine can be categorised as a drag turbine. They were the first kind of water wheel to be used due to their simple construction and low need for maintenance (Muller et al., 2007; Quaranta and Revelli, 2018). Paddlewheel turbines are characterised by an orientation chosen so that the flow direction is perpendicular to the axis of rotation of the device (ITTC, 2014).

In the Van Rompay Turbine, the paddlewheel is self-floating. An advantage of the paddlewheel being self-floating is that at least a part of its own weight is neutralised by the upward force of the water, such that the load on the bearings in which the paddlewheel shaft is mounted is reduced, or even completely neutralised. This contributes to a reduction of losses in the bearings, such that more hydraulic energy is available for driving the generator, which results in more electric power being generated by the generator. In Figure 3.10, two paddlewheels are drawn. One with twelve blades and the other with six blades. The most optimal number of blades need to be found by future experiments as this is not within the scope of this research.
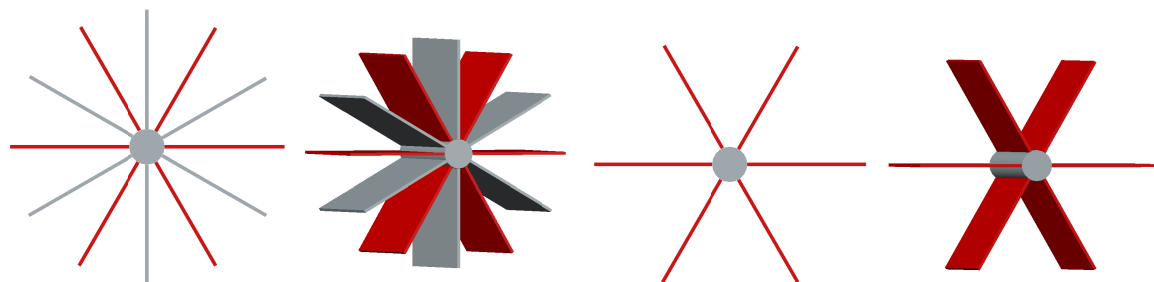
(a) 3D view paddlewheel 12 paddles (b) Side view paddlewheel 12 paddles (c) 3D view paddlewheel 6 paddles (d) Side view paddlewheel 6 paddles

Figure 3.10: paddlewheel designs - Own Work

Air chamber

An air chamber is present inside the turbine. This air chamber should be built airborne. In this chamber, a paddlewheel will be installed. An advantage when making use of this air chamber, compared to the already active hydrokinetic energy systems, is that the turbine will rotate in an air environment and will be powered by the water flow. This implies that the turbine experiences less friction during rotating compared to the fully submerged horizontal axis turbines. Note that electricity is needed to keep the air chamber on the right pressure.

In Figure 3.11, the concept of the ducted system is shown and the air chamber is indicated.
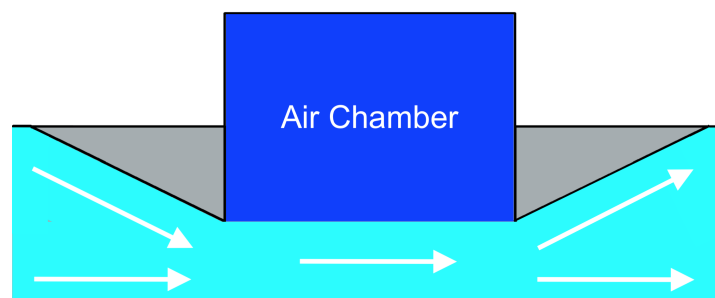
Figure 3.11: Concept Van Rompay Turbine - Own work

Because the turbine will rotate in an air environment, the materials are less exposed to (salt)water. This can be seen as an advantage as less maintenance is needed due to the lower amount of corrosion damage and marine organisms that have the chance to attach themselves to the turbine.

Extended Rotation Area

The paddlewheel will be installed in the air chamber. By enlarging the size of segment 2 (thus the air chamber), the diameter of the paddlewheel can be enlarged as well. The diameter of the paddlewheel determines the immersed radius ratio. The ratio can be found in Equation 3.1

$$\text{Immersed radius ratio} = \frac{i}{r} \tag{3.1}$$

These parameters are presented in Figure 3.12.
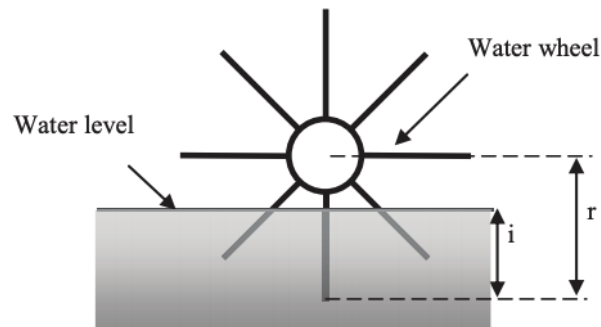
Figure 3.12: Immersed radius ratio (Tevata and Inprasit, 2011)

For a too high ratio, a large drag force at the paddle back is occurring. The water impulse force at the paddle face was resisted by the drag force on the paddle back (Tevata and Inprasit, 2011). For a too low ratio, this could cause that the water wheel model could not rotate for a given torque load. This is because its water impulse area was too small (Tevata and Inprasit, 2011). It can be concluded that for each design, the optimal immersed ratio should be found to optimize the paddlewheels performance.

In Figures 3.13 and 3.14, a prototype without an extended air chamber and with an extended air chamber can be seen respectively. For an extended air chamber, the shaft of the rotor can be located above the water-line. This has the advantage that the shaft does not come into contact with the water. This entails that less maintenance is required because there is less biofouling and corrosion.
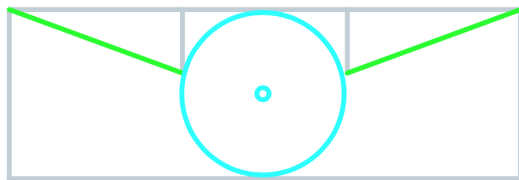
Figure 3.13: No extended air chamber - Own work
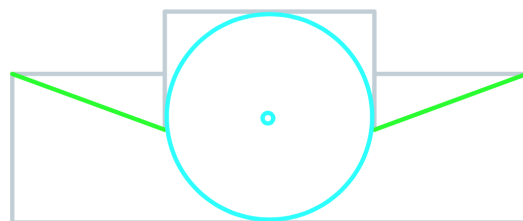
Figure 3.14: Extended air chamber - Own work

Location

The Van Rompay Turbine could be installed in oceans, rivers, estuaries or similar where currents are present. The higher the current velocity, the higher the power in the flow. Besides, the Van Rompay turbine could also be operational at locations where lower velocities are present. However, the power output will be lower as this is proportional to the velocity.

An advantage is that the Van Rompay Turbine can be stationed close against a bank or dry land. This involves that the transmission of the generated energy to the electricity grid is much cheaper and more efficient because it is closer to the electricity grid so that shorter cables are required underwater to make a connection to the closest power station on dry land. Moreover, fewer losses will occur in the cable, such that the efficiency is higher.

Size

Because the Van Rompay Turbine is relatively large due to the ducted system compared with the already active hydrokinetic energy turbines, this can be seen as a disadvantage. However, the device could be located close

to the bank where it does not impede boats sailing on the river. This is of course dependent on the available space and the restrictions. On the ocean, more space is available, therefore larger devices can be installed here.

Dealing with Biofouling

Submerged constructions are expensive. Whatever you build gets exposed to (salt)water, sand debris, barnacles and storms. However, less fouling will occur when high flow velocities are present.

As the inside of the Van Rompay Turbine is subject to these high velocities, less fouling will be present in the first place. The fouling that will be present, however, is not an issue for the Van Rompay Turbine, provided the correct coating is chosen. We should treat the components of the device with a non-toxic coat of paint based on a surface-treated composite coating. Such a coating is described in the white book of Van Rompay (2012). Due to the maintenance-friendly properties of this coating, growth can easily be removed with cleaning equipment. The methods that are used can be found in patent BE1013187 (Van Rompay, 2004) and patent BE2010/0423 (Van Rompay, 2010).

By using this coating, environmental pollution is ruled out by the non-toxic nature of this paint. No corrosion problems will occur and therefore no energy losses will be caused by rust. The blades can be made thinner and therefore, the device is lighter.

Maintenance

According to a preferred embodiment, the paddlewheel is equipped with a number of radially oriented paddles, and at least one of which is always partially in the water during use. In this way, the paddlewheel can be set into motion by the water, without it being necessary to place the shaft of the paddlewheel underwater. This provides the advantage that the device is very simple which makes its construction cheap and it is easily accessible without extra facilities. Aside from the paddles of the paddlewheel, there are no other moving parts that are underwater, such that no extra attention is required for sealing and other measures to prevent the harmful effects of water.

4

Methods

In this chapter, the methods and associated equipment for the various experiments to investigate the ducted system of the Van Rompay Turbine are explained in detail. Two types of experiments can be distinguished:

- Field experiments

- CFD simulations

    – Modelling and simulating the ducted system of the Van Rompay Turbine
    – Scaling up the ducted system of the Van Rompay Turbine

4.1. Field experiments

In this section, the method of executing the field experiments is discussed. The information about the test location, experiment set-up, prototype, equipment, model approach, data acquisition and the accuracy are covered in this section.

4.1.1. Test Location

The experiments were conducted in front of the Hydrex headquarters in the Port of Antwerp, Belgium. This made the experiments easier as the necessary tools were within reach. As can be seen in Figure 4.1, the water in front of the Hydrex headquarters is stagnant water. Running water is a requirement to test the prototype. The running water was simulated by propellers of a workboat. This will be explained in Section 4.1.2. This method was chosen over carrying out the experiments in a river because the inlet velocity was controllable by the workboat's propellers. This made the process easier because changes to the prototype could be tested more quickly at different inlet velocities.
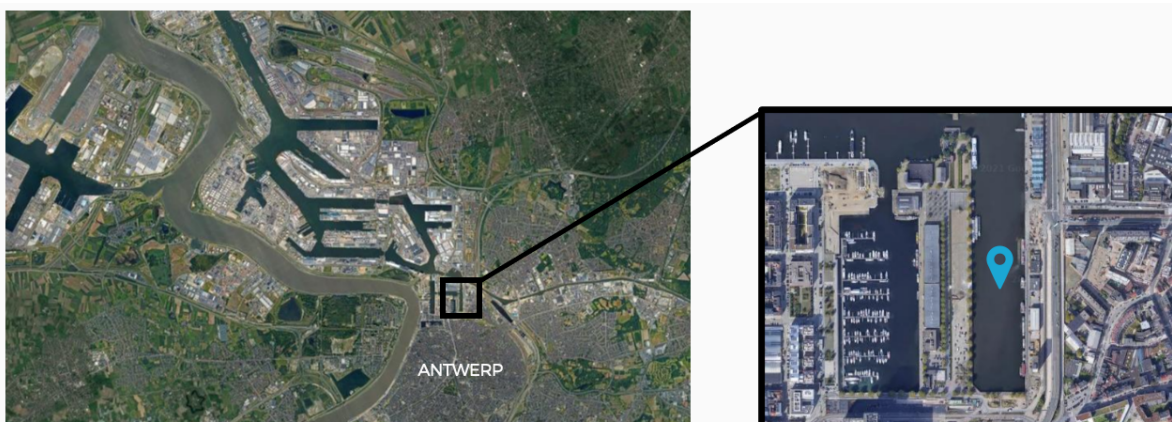
Figure 4.1: Location experiments - Google Maps

4.1.2. Experiment Set-up

Two workboats were used for the test setup. One to attach the prototype to and the other to simulate flowing water using the propellers. A truss construction has been attached to the prototype which can be slide into a rail using a crane. The rails themselves are attached to the workboat and thus provide a fixed construction. The top view of the set-up can be seen in Figure 4.2 and the prototype with the truss construction is showed in Figure 4.3.
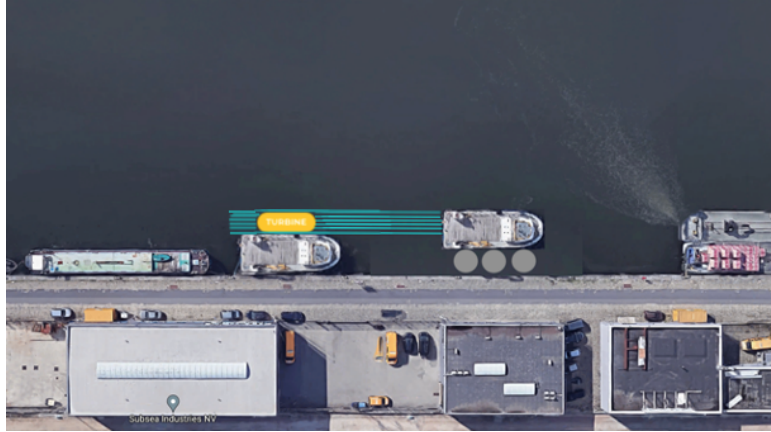
Figure 4.2: Top View Experiment Set-Up

Figure 4.3: Truss construction

To simulate running water with the propellers of the workboat, and to prevent excessive turbulence in the flow, sufficient distance has been left between the propellers and the prototype.

In Figures 4.4, the prototype is launched into the water by sliding the truss construction into the rails which is fixed to the workboat. In Figure 4.5, an image captured inside the air chamber is shown.

Figure 4.4: Prototype launched and fixed to the workboat

Figure 4.5: Image inside the air chamber

4.1.3. Prototype

To carry out the experiments, a prototype of the ducted system of the "Van Rompay Turbine" is built. The prototype is dimensioned and designed according to the information of the patent (Van Rompay, 2017) and the requirements from the company. The main dimensions of the prototype can be found in Table 4.1. Its corresponding 3D drawing can be found in Figure 4.6.

Table 4.1: Dimensions Prototype

Measurements	Value
Length	4.05 m
Width	1.17 m
Height	1.17 m
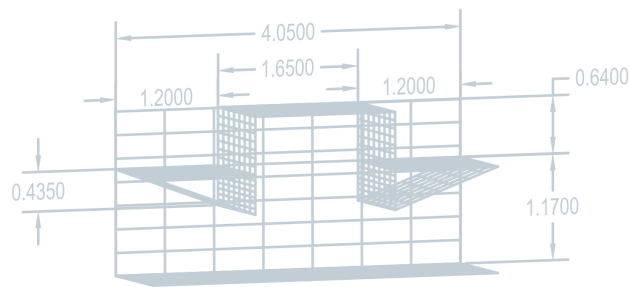
Figure 4.6: Prototype Drawing

4.1.4. Equipment

The instruments used during the experiments are explained in this section.

Flow Velocity Measuring Equipment

Flow velocity measurements are carried out using hydrometric propellers (Type: OTT, C31 Universal Current Meter). These propellers were used in combination with a cable suspended from the workboat connected to counter units to count the number of rotations (OTT, n.d.). The rotation rate of the calibrated propeller is proportional to the water velocity. The velocity is determined by registering the number of rotations over a pre-selected time period. Note that these are point measurements and are therefore not able to measure the complete velocity field. Four C31 Universal Current Meters are installed of which two can measure up to 5 m/s and the other two up to 6 m/s. The specifications are shown in Appendix H.

The data of two velocity meters (at the inlet and inside the ducted system) were used in this research. The two other velocity meters have been installed at the outflow of the prototype. This data will be used to compare with future research when scaling the dimensions.

Camera Equipment

To analyse and study the behaviour of the water flow in combination with the air chamber, two cameras are installed. The cameras are connected to a video unit at the workboat where live images were visible. The live images could be recorded for later review and study. In Figure 4.7 and Figure 4.8, the camera equipment used during the field experiments is shown.

Air Compressor and Power Unit

An air compressor is needed to keep the air pressure constant inside the air chamber of the prototype during the experiments. Metabo 700-90 D is used during the experiments. To provide the air compressor of electricity, a power unit is installed. In Figure 4.9, the air compressor and power unit are shown.

Figure 4.7: Camera

Figure 4.8: Video Unit

Figure 4.9: Air Compressor & Power Unit

4.1.5. Model Approach

During the experiment, step by step changes were made to the prototype to measure the differences in flow velocity increase.

Firstly, the field experiments consist of testing three inclination angles: 21°, 26° & 31°, for the converging inflow and diverging outflow segment, referred to as the small, medium and large ramp size, respectively, to determine which size represents the lowest energy losses in the system. The flow velocity increase caused by ramp sizes is calculated by measuring the inlet velocity and the velocity inside the ducted system. In Table 4.2, an overview of the three different in -and outflow angles are presented. In Figure 4.10, the ramp sizes are visualised.

Table 4.2: Angle of in -and outlet

Ramp Size	In -and Outlet Angle
Small	±21°
Medium	±26°
Large	±31°
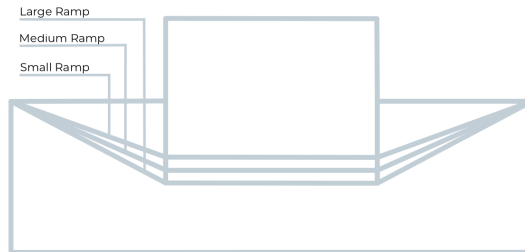
Figure 4.10: Ramp Designs Experiments

Secondly, the ramp with the greatest flow velocity increase is selected to change the inflow design to optimise the flow velocity increase. Subsequently, on the best performing ramp size in terms of lowest energy losses, five designs were tested, referred to as the straight, curved and the high, mid & low frequency waved designs; to determine which design represents the lowest energy losses in the system. The waved designs are tested during the experiments as they have the capability to cause drag reduction. This mechanism is explained in Appendix K. The flow velocity increase caused by the different ramp designs is calculated again by measuring the inlet velocity and the velocity inside the turbine. The design parameters of the ramp designs are presented in Table 4.3 and the ramps are visualised in Figure 4.11.

Table 4.3: Parameters ramp designs

Ramp Design	Wave Length	Wave Height
Straight	N/A	N/A
Curved	$\lambda = 1200$ mm	H = 120 mm
Low Frequency Waved	$\lambda = 420$ mm	H = 90 mm
Mid Frequency Waved	$\lambda = 180$ mm	H = 50 mm
High Frequency Waved	$\lambda = 70$ mm	H = 19 mm
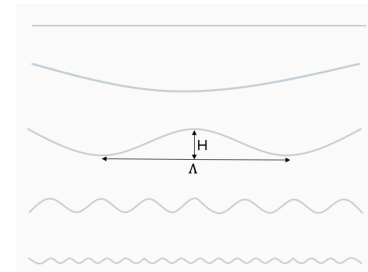
Figure 4.11: Drawings ramp designs

Images of the different ramp designs used during the experiments are presented in Figure 4.12.

Figure 4.12: Different ramp designs during experiments

4.1.6. Data Acquisition

The flow velocity measurement points are indicated in Figure 4.13 by P_1 and P_2 .

Figure 4.13: Velocity measurement locations

Point P_1 will represent the flow velocity in the ocean, river, estuary or similar. Point P_2 is equal to the flow velocity inside the turbine. This flow velocity increase is calculated using Equation 4.1.

$$\text{Flow Velocity Increase} = 100 \cdot \frac{\text{Velocity Inside the Turbine}}{\text{Inlet Velocity}} - 1 \qquad (4.1)$$

This flow velocity increase represents the velocity increase due to the converging segment. The greater this parameter, the lower the energy losses in the ducted system.

The data is acquired by carrying out the velocity measurements for an inlet velocity ranging between 0 m/s and 0.5 m/s. The inlet velocity can be controlled by changing the RPM of the propellers of the workboat. For different RPMs, multiple measurements are carried out. The rotations of the velocity meter propellers are counted over a pre-selected time period of 100 seconds. To translate the number of rotations into velocity, Table 4.4 was used. The parameter n indicated the propeller revolution per second. Additional information about the parameters can be found in in Appendix H.

Table 4.4: Velocity formula for each velocity meter

Measurement Point	Propeller Type	Velocity Range	Velocity Formula
P1	Propeller 1-75228	5 m/s	If n<0.63 $\Rightarrow$ 0,2458n + 0,017 If n≥ 0.63 $\Rightarrow$ 0,2600n + 0,008
P2	Propeller 2-74472	6 m/s	If n<0.33 $\Rightarrow$ 0,4755n + 0,017 If n≥ 0.33 $\Rightarrow$ 0,518n + 0,003
P3	Propeller 2-77011	6 m/s	If n<0.33 $\Rightarrow$ 0,4755n + 0,017 If n≥ 0.33 $\Rightarrow$ 0,518n + 0,003
P4	Propeller 1-49417	5 m/s	If n<0.64 $\Rightarrow$ 0,2465n + 0,015 If n≥ 0.64 $\Rightarrow$ 0,259n + 0,007

4.1.7. Accuracy

The accuracy of the C31 Universal Current meters is ±2%. This accuracy is acceptable to get reliable results. However, these meters involve several disadvantages. Firstly, the current meters are not measuring the entire flow velocity field as it is a point measurement. The average flow velocity of the profile could therefore not be measured. Another disadvantage is that for lower velocities, the propeller could be less accurate.

4.2. CFD Simulations

In this section, the method of executing the CFD simulations is explained. The CFD software package COM-SOL Multiphysics is used to model the Van Rompay Turbine.

4.2.1. Model Approach

Geometry

The 3D model is encompassed by a block, representing the free water flow that flows in the direction of the inlet of the ducted system. The ducted system of the Van Rompay Turbine is based on the Venturi effect and will therefore, when designed correctly, accelerate the incoming flow. The CFD simulations are applied to:

- Carry out CFD simulations of the different ramp designs to investigate the hydrodynamics.

- Scale up the dimensions of the prototype by making use of the CFD simulations to study the hydrodynamics inside the ducted system.

COMSOL Multiphysics provides the ability to apply material settings to each of the geometric components. The ducted system of the Van Rompay Turbine is defined as steel (similar as the prototype during the field experiments), whereas the block is defined as water. The mesh is adjustable to the desired element quality for the turbine and the block. The mesh of the ducted system is made up of a finer mesh because these solutions require higher quality. The mesh covers the surface of all components. For scaling up the geometry, the mesh size is adapted. In Figure 4.14, an example of a simulation in CFD is shown.
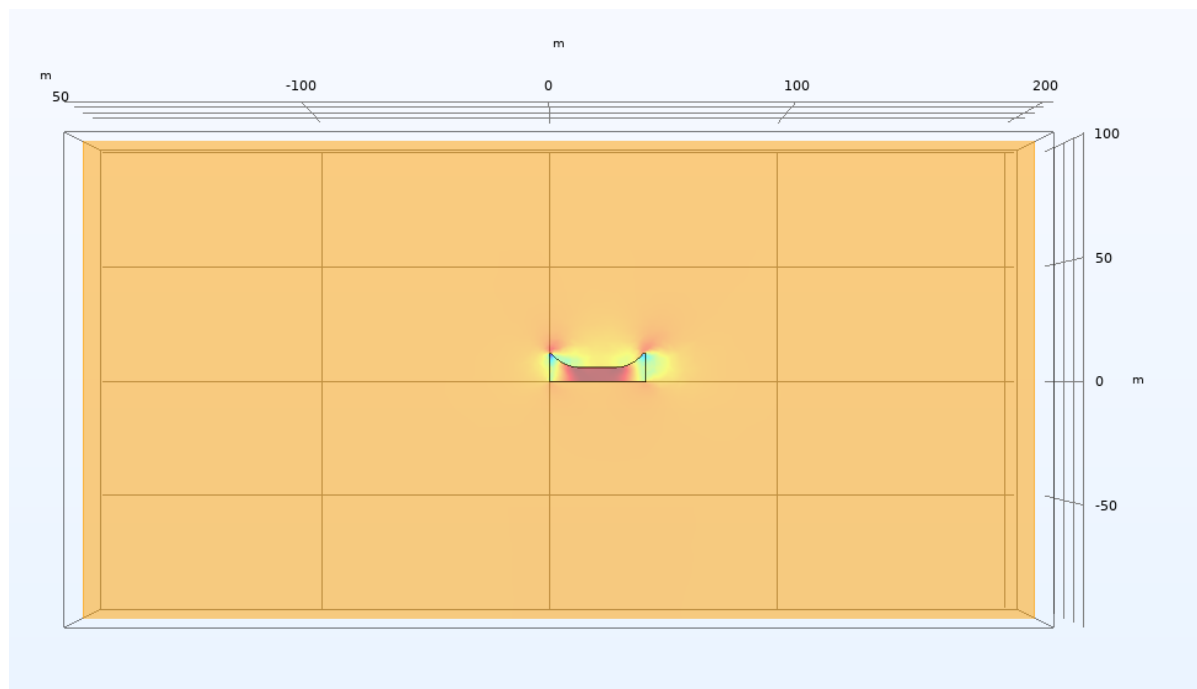
Figure 4.14: Example CFD Simulation

One-Phase Simulation

The simulation is based on a one-phase simulation. This entails that only the phase water is used and air is not simulated. The boundary between the air chamber and the water flow is therefore simulated as a plate. This could have an influence on the turbulence levels created by the air chamber.

Inlet Velocity

The time-dependent velocity should be described with an analytical function which increases over a time period of 50 seconds. This is plotted in COMSOL and is presented in Figure 4.15.
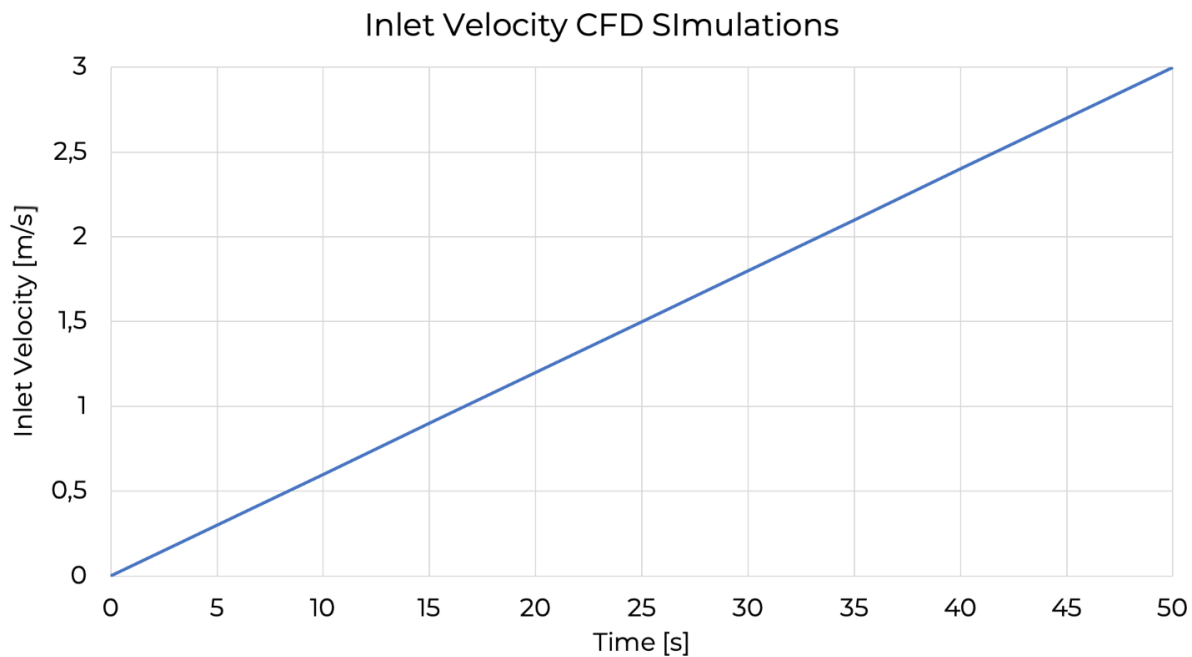
Figure 4.15: Inlet Velocity Plot CFD Simulations

Turbulence Closure Model

The Van Rompay Turbine will be installed in a turbulent environment like oceans, rivers, estuaries or similar. Therefore, the ducted system of the Van Rompay Turbine was simulated for a turbulent flow. The first step is to apply stationery, laminar flow to determine the velocities and pressure distribution throughout the ducted system. In the second step, the results of the stationary, laminar flow are used as initial values to study the time-dependent turbulent flow.

The K-ϵ Turbulence Closure Model is chosen and simulates mean flow characteristics for turbulent flow conditions. This is done by making use of two transport equations (PDEs), namely the Reynolds-averaged Navier-Stokes (RANS) equations for conservation of momentum and the continuity equation for conservation of mass. The turbulence closure model is explained in more detail in Chapter 5.

The flow near the walls is modelled using wall functions. The K and ϵ represent respectively the turbulent kinetic energy and the dissipation rate of the turbulent kinetic energy. The following dependent variables are defined for this physics interface:

- Velocity field u and its components

- Pressure p

- Turbulent kinetic energy k

- Turbulent dissipation rate ϵ

Advantages of this model are that it is a stable and easy method to solve the model as a coarser mesh can be used near the wall. It performs well for external flow problems and complex geometries. Disadvantages are that due to the wall function approximation, the solution at the wall is less accurate.

4.2.2. Data Acquisition

Turbulence

Data about the magnitude of turbulence is acquired by averaging the turbulent kinetic energy over the volume of the ducted system. The turbulence kinetic energy, k, is the kinetic energy per unit mass of the turbulent fluctuations and is expressed in [J/kg]. This parameter represents the magnitude of turbulence in the ducted

system. For every simulation, the turbulent kinetic energy is measured. The formula for turbulence kinetic energy is presented in Equation 4.2.

$$k \stackrel{\text{def}}{=} \frac{1}{2} \overline{u_i' u_i'} = \frac{1}{2} \left(\overline{u_x'^2} + \overline{u_y'^2} + \overline{u_z'^2} \right) = \frac{3}{2} \overline{u'^2} \tag{4.2}$$

Velocity

The data is acquired by measuring the velocity at two points. These two points are similar as the locations of the point measurements during the field experiments. The first point represents the inlet velocity whereas the second point represents the velocity inside the turbine. The data at these two points are collected over a period of 50 seconds. This data is then used to calculate the flow velocity increase between the inlet velocity and the velocity inside the turbine. In Figure 4.16, the two points are shown where the velocity will be measured.
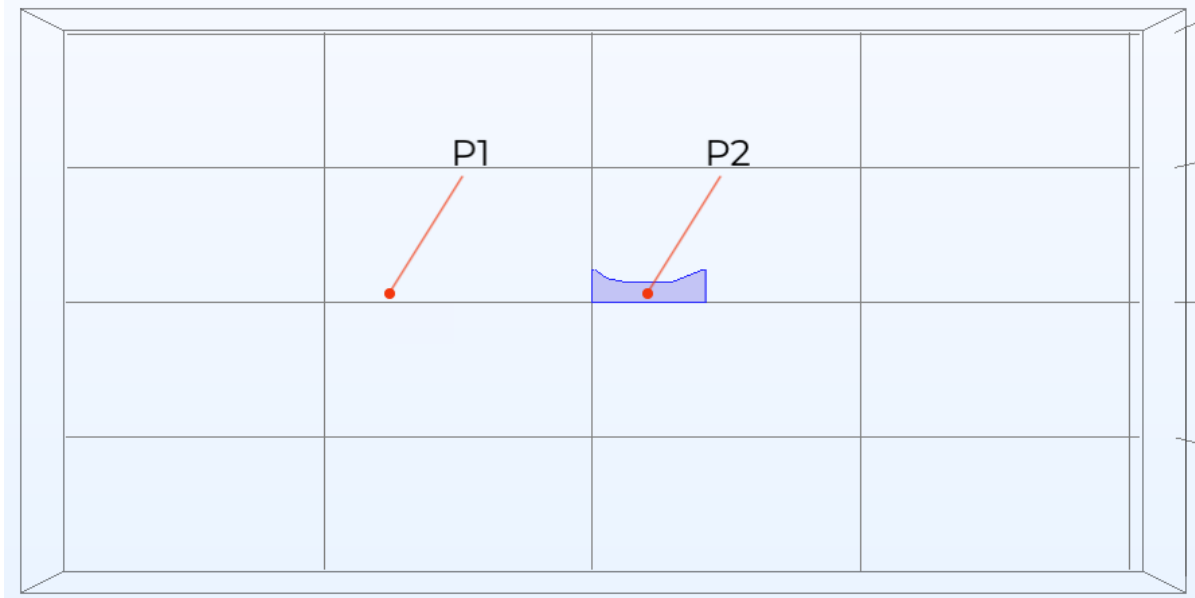
Figure 4.16: The velocity measurement points

This flow velocity increase is calculated using Equation 4.3.

$$\text{Flow Velocity Increase} = 100 \cdot \frac{\text{Velocity Inside the Turbine}}{\text{Inlet Velocity}} - 1 \tag{4.3}$$

4.2.3. Accuracy

There are three methods executed to validate the model.

- The first method is to check the mesh quality. The rule of thumb is that it should have a minimum element quality of at least 0.1.

- The second method to validate the model is to integrate the inflow and outflow surface. When integrating the surface over the velocity, the volume that enters the model and leaves the model can be compared. The difference between these two values indicates the error.

- Subsequently, after running the model, the reciprocal of the time step and the error can be found under the "convergence plot 1" and "convergence plot 2". This indicates whether the simulation converges well.

A conclusion can be made based on the outcomes of these accuracy-tests whether the accuracy is sufficient and the CFD simulations could be used for research.

<div align="right">

5

</div>

<div align="right">

Results

</div>

In this chapter, the results of the experiments are presented and substantiated. The results are divided into the following phases:

- Phase 1: Field experiments

- Phase 2: CFD simulations

- Phase 3: CFD scaling

5.1. Phase 1: Field experiments

A prototype of the ducted system of the Van Rompay turbine was tested during the field experiments to investigate the impact on the hydrodynamics of the different geometries of the ducted system. This is carried out by studying the impact in flow velocity increase when changing the ramp sizes and designs. The velocity is measured with point measurements at the inlet and inside the ducted system. The flow velocity increase is a critical parameter as this implies how much energy is lost caused by the Venturi ducted system. During the experiments, step by step adjustments was made to the prototype to measure the flow velocity increase.

Firstly, three inclination angles: 21°, 26° & 31°, for the converging inflow and diverging outflow segment were tested, referred to as the small, medium and large ramp size, respectively, to determine which size represents the lowest energy losses in the system. Subsequently, on the best performing ramp size, in terms of lowest energy losses, five designs were tested, referred to as the straight, curved and the high, mid & low frequency waved designs; to determine which design represents the lowest energy losses in the system. Roughed waved wall designs are streamwise wavy walls with each a different wavelength and amplitude.

5.1.1. Ramp Sizes

Firstly, the inlet velocity and the velocity inside the ducted system are plotted for the three tested ramp sizes. In this way, the velocity measurements of each ramp size can be studied.

This flow velocity increase is calculated using Equation 5.1. Secondly, the flow velocity increase is calculated and are plotted for each ramp size. The higher this value, the lower the losses due to turbulence and friction and thus the more optimal the design.

$$\text{Flow Velocity Increase} = 100 \cdot \frac{\text{Velocity Inside the ducted system}}{\text{Inlet Velocity}} - 1 \qquad (5.1)$$

The flow velocity increase is based on the continuity equation. The continuity Equation 5.2 states that the flow rate in point 1 equals the flow rate in point 2. If the cross-section gets smaller, the flow velocity increases, and vice versa.

$$A_1 v_1 = A_2 v_2 \qquad (5.2)$$

Inlet Velocity vs. Inside ducted system Velocity

In the Figures 5.1a, 5.1c and 5.1e, the three different ramp sizes are drawn. In the Figures 5.1b, 5.1d and 5.1f, the inlet velocity (P1) and the velocity inside the ducted system (P2) is plotted.

(a) Drawing Small Straight Ramp

(b) Velocities P1 and P2 for Small Straight Ramp

(c) Drawing Medium Straight Ramp

(d) Velocities P1 and P2 for Medium Straight Ramp

(e) Drawing Large Straight Ramp

(f) Velocities P1 and P2 for Large Straight Ramp
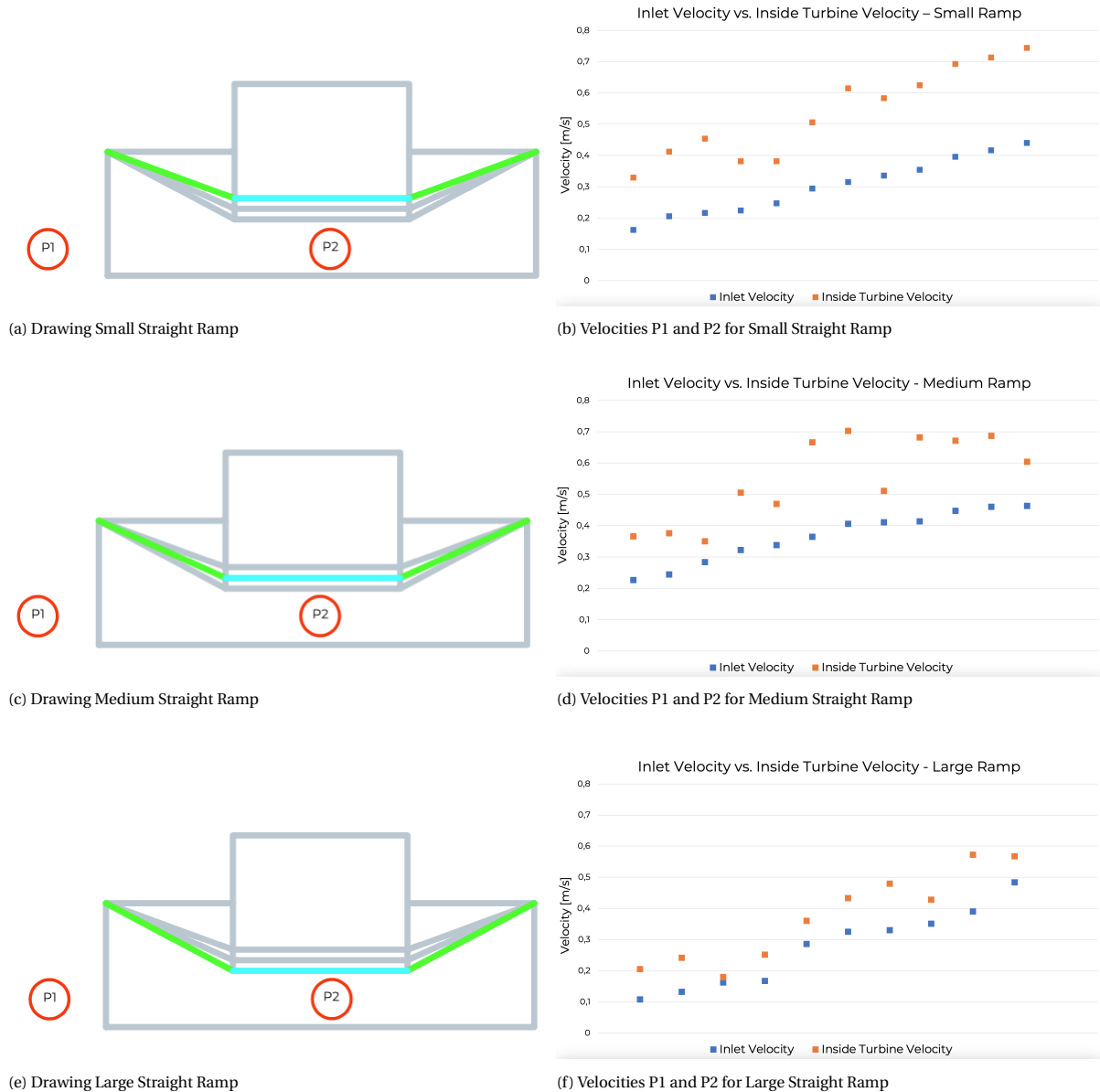
Figure 5.1: Drawings and velocity plots for ramp size experiments

The data points acquired by the field experiments are fluctuating. The fluctuation may likely be the cause of turbulence inside the ducted system. Other external factors may also play a role in the accuracy of the data. Examples of these factors are the movement of the prototype, the movement of the workboat during the experiments, and the irregular retention of pressure by the air compressor influences the fluctuating behaviour of the data.

Flow Velocity Increase

The flow velocity increase is calculated using Equation 5.1. This parameter represents the magnitude of acceleration caused by the converging inflow. In Figure 5.2, the flow velocity increase of the three different ramp sizes is presented over an inlet velocity between 0 and 0.5 m/s. Polynomial trend lines to the 2nd power are plotted as this behaviour is found in prior research carried out by Jung et al. (2011).

Flow Velocity Increase (P1-P2) - Ramp Sizes
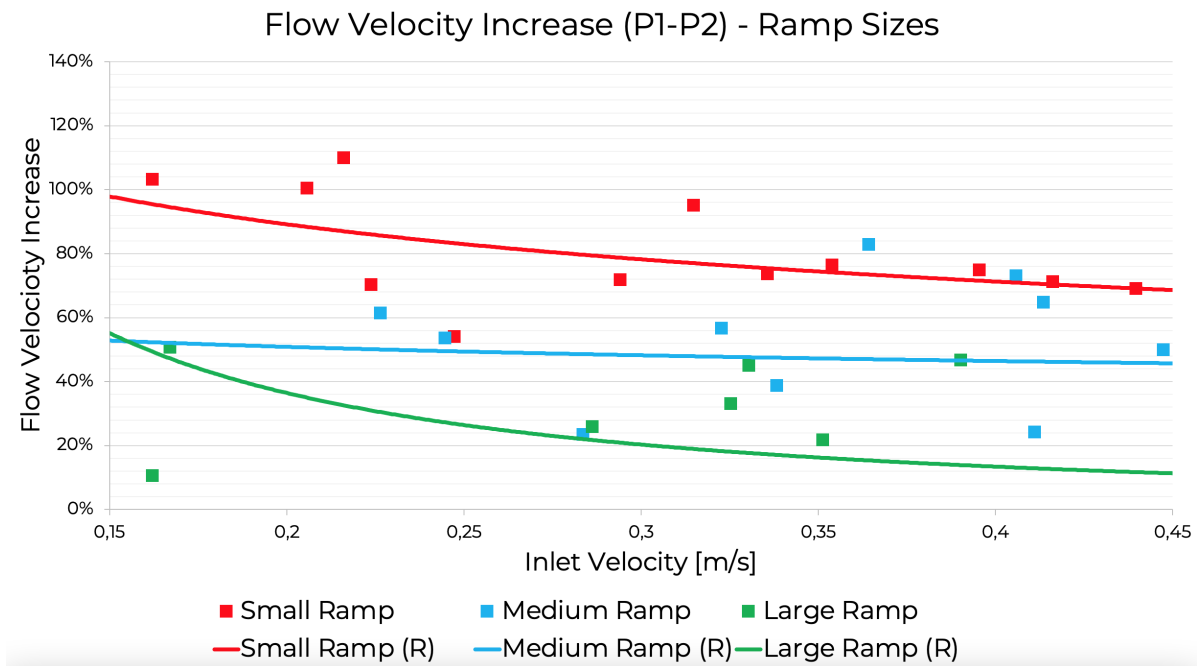
Figure 5.2: Flow Velocity Increase for the small, medium and large ramp over the velocity range of 0 - 0.5 m/s

In Figure 5.2, the small ramp represents the greatest increase and is, consequently, the most optimal of the three ramps tested between a range of 0 m/s and 0.5 m/s.

We can see in Figure 5.2 that the velocity increase occurs for all three ramps when the cross-sectional area decreases. However, the small ramp represents the highest flow velocity increase caused by the venturi system compared to the medium and large ramp. Based on the experiments, the continuity equation seems to be contradicted. It would be expected that the large ramp represents the highest flow velocity increase as this ramp has the smallest cross-sectional area. However, the water flow for the medium and large ramp indicates too much blockage due to turbulence caused by a too steep converging ramp.

It can be stated that the results, due to the scattering of the data points, show uncertainty. The plotted trend lines based on the data points are used to acquire information about the different ramp designs. Hence, the trend lines may be uncertain. In Section 5.2, these experiments are modelled in CFD simulations to investigate the ducted system further. In Table 5.1, a summary of the average flow velocity increase of the ramp sizes is shown, including their corresponding angle.

Table 5.1: Average Flow Velocity Increase Ramp Size - field experiments

Ramp Design	Ramp Angle	Average Flow Velocity Increase
Small Ramp	21°	80.9%
Medium Ramp	26°	55.7%
Large Ramp	31°	42.3%

Based on the experiments, the small ramp represents the highest flow velocity increase with a value of 80.9% compared to the medium and large ramp. The impact on the flow velocity increase of the medium and the large ramp is lower. Respectively, an average flow velocity increase of 55.7% and 42.3% is found. This indicates that the small ramp represents the lowest energy losses in the system. Therefore, the small ramp was used for further investigation. The further investigation consisted of changing the inflow design to reduce energy losses inside the ducted system. In total, five different designs were tested.

5.1.2. Ramp Designs

For the tested ramp designs (straight, curved and the high, mid & low frequency waved designs), the inlet velocity (P1) and the velocity inside the ducted system (P2) are plotted. This is done to determine which design represents the lowest energy losses in the system. Based on this data, the flow velocity increase of each ramp design is calculated and presented. This flow velocity increase is calculated using Equation 5.1.

Inlet Velocity vs Inside the ducted system Velocity

In the Figures 5.3a, 5.3c, 5.3e, 5.3g and 5.3i, the different ramp designs are portrayed. In the Figures 5.3b, 5.3d, 5.3f, 5.3h and 5.3j, the inlet velocity and the velocity inside the ducted system is plotted for each design.
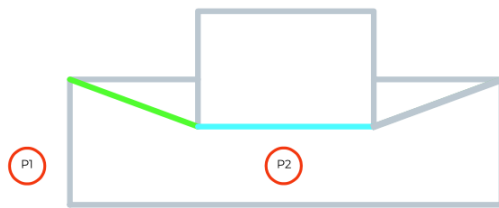
(a) Drawing Small Straight Ramp
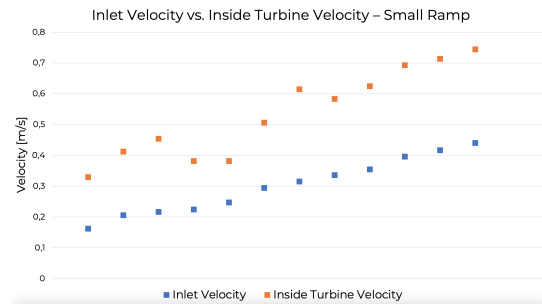
(b) Velocities P1 and P2 for Small Straight Ramp
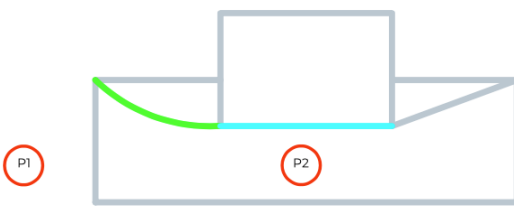
(c) Drawing Small Curved Ramp
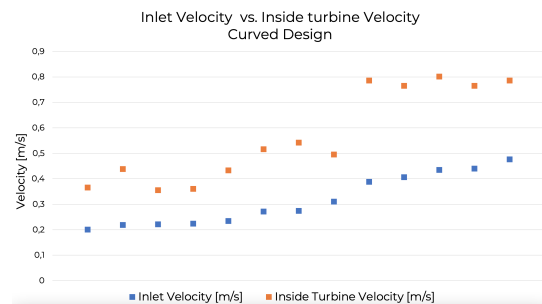
(d) Velocities P1 and P2 for Small Curved Ramp
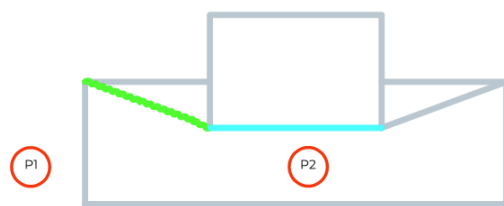
(e) Drawing High Frequency Waved Small Ramp
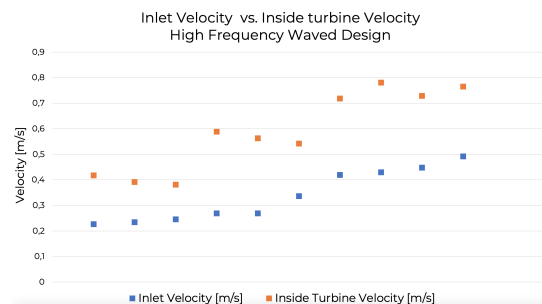
(f) Velocities P1 and P2 for Small High Frequency Waved Ramp

(g) Drawing Mid Frequency Waved Small Ramp
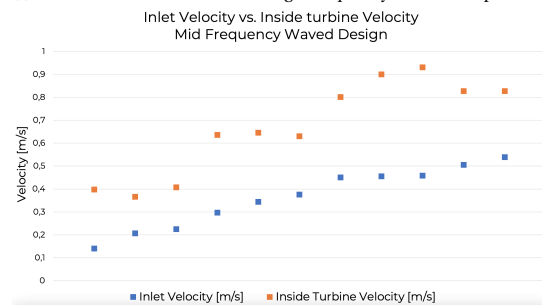
(h) Velocities P1 and P2 for Small Mid Frequency Waved Ramp

(i) Drawing Low Frequency Waved Ramp

(j) Velocities P1 and P2 for Small Low Frequency Waved Ramp
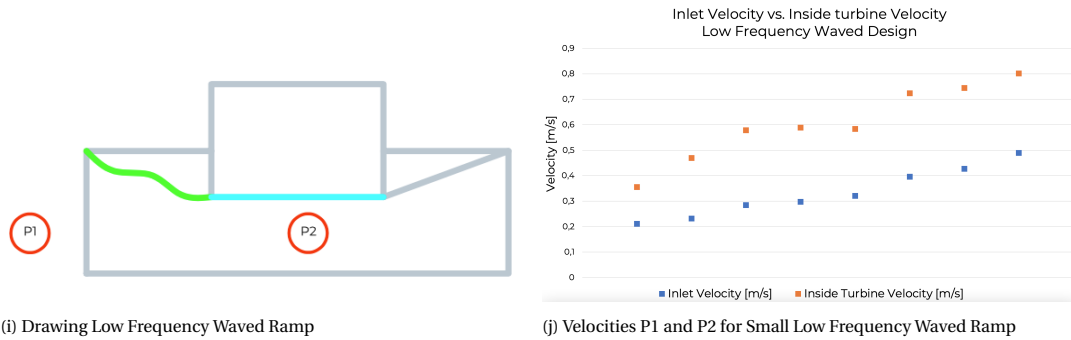
Figure 5.3: Drawings and velocity plots for ramp design experiments

Similar to the prior experiments, the data shows fluctuation. Once again, the reason for this is likely the turbulent behaviour inside the ducted system. External factors, such as the movement of the prototype and the workboat during the experiments and the irregular retention of pressure by the air compressor, influence the fluctuating behaviour of the data.

Flow Velocity Increase
The flow velocity increase is calculated with Equation 5.1. In Figure 5.4, the data points representing the flow velocity increase of the different ramp designs are presented over an inlet velocity between 0 and 0.5 m/s. Polynomial trend lines to the 2nd power are plotted as this behaviour is found in prior research carried out by Jung et al. (2011).
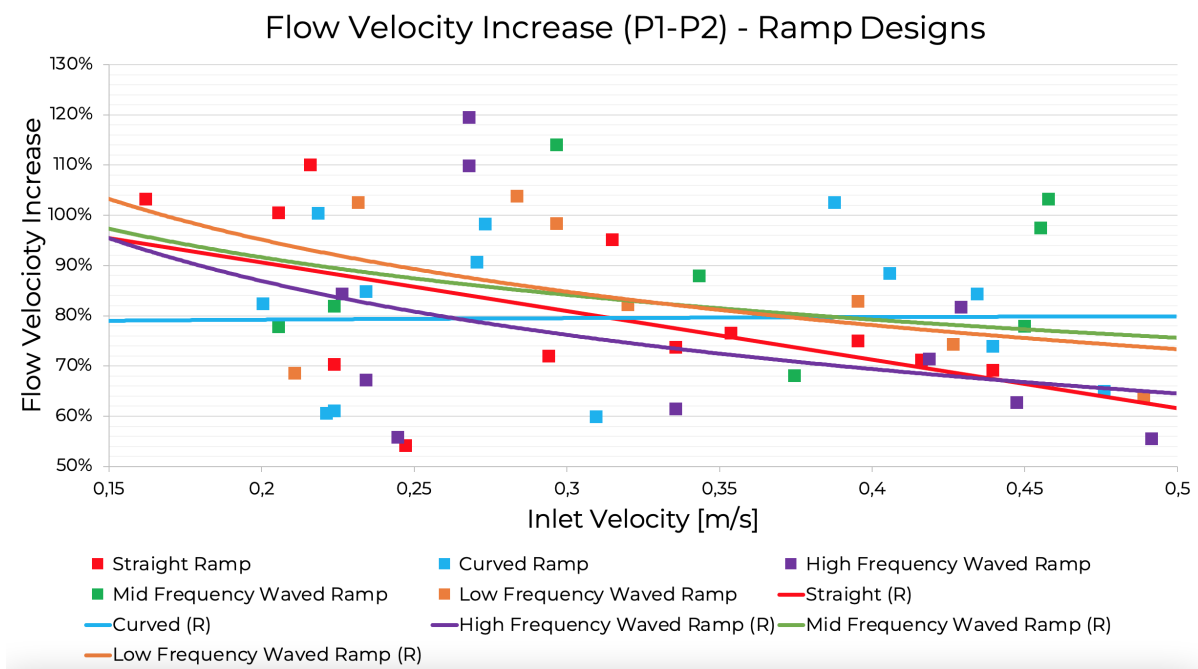
Figure 5.4: Flow Velocity Increase for different design ramps

As can be seen in Figure 5.4, the low frequency waved ramp represents the highest velocity increase between a range of 0 and 0.4 m/s and the curved design shows the greatest velocity increase between 0.4 and 0.5 m/s. This indicates that these designs represents the lowest energy losses in the system for both velocity ranges. Overall, the waved designs show a greater velocity increase for inlet velocities between 0 and 0.4 m/s compared to the straight design. This can be explained by prior studies concerning streamwise wavy walls (Quadrio et al., 2009). These studies indicate that waved walls have the capability to reduce turbulence. In Appendix K, this is phenomenon is discussed and explained in more detail.

The curved ramp shows a higher flow velocity increase in comparison to the straight ramp for inlet velocities between 0.4 m/s and 0.5 m/s. Zerpa et al. 2019 state that this is because the pressure gradient drops exponentially due to the curved shape. The pressure drop between the converging part and inside the ducted system has a smooth transition and, therefore, it results in a lower local pressure head loss.

It can be stated that the results, due to the scattering of the data points, show uncertainty. The plotted trend lines based on the data points are used to acquire information about the different ramp designs. Hence, the trend lines may be uncertain.

In Table 5.2, a summary of the different ramp designs are shown including their corresponding flow velocity increase.

Table 5.2: Average Flow Velocity Increase Ramp Design - field experiments

Ramp Design	Wave Length	Wave Height	Flow Velocity Increase
Straight	N.A	N.A	80.9%
Curved	$\lambda = 1200$ mm	H = 120 mm	80.8%
High Frequency Waved	$\lambda = 70$ mm	H = 19 mm	77.0%
Mid Frequency Waved	$\lambda = 180$ mm	H = 50 mm	91.8%
Low Frequency Waved	$\lambda = 420$ mm	H = 90 mm	84.6%

The mid frequency waved ramp represents the highest overall flow velocity increase with a value of 91.8% over the entire inlet velocity range (0-0.5 m/s). However, for the velocity range between 0 and 0.4 m/s, the low frequency waved ramp represents the higher flow velocity increase. For higher velocities (0.4-0.5 m/s), the curved ramp shows to represent a higher flow velocity increase.

The data points acquired during the experiments were scattered due to external factors increasing the uncertainty of the measurements. Besides this, the experimental investigations were tested over an inlet velocity between 0 and 0.5 m/s, limiting the data analysis. For this reason, several CFD simulations were carried out in Section 5.2 to acquire data with no influence of external factors and to investigate the system for higher velocities.

5.2. Phase 2: CFD simulations

This chapter aims to investigate how CFD modelling can help to improve the design of the Van Rompay Turbine. This is done by modelling the ducted system in the CFD software COMSOL Multiphysics (5.6) to represent the field experiments. Subsequently, this model is used to study the impact in terms of turbulence and the impact in flow velocity increase when changing between different ramp designs. The advantage compared to the field experiments is that the external factors that cause scattering in the data are not applicable, and the ducted system can be investigated for higher inlet velocities.

The geometry is modelled in 3D. The 3D model is encompassed by a block, representing the water that flows in the direction of the inlet of the ducted system. COMSOL Multiphysics provides the ability to apply material settings to each of the geometric components. The Van Rompay Turbine ducted system is defined as steel, whereas the block is defined as water. The mesh is adjustable to the desired element quality for the ducted system and the block. The mesh of the ducted system is made up of a finer mesh because these solutions require higher quality. The mesh covers the surface of all components.

5.2.1. Turbulence Closure Model

The CFD simulation is performed with COMSOL Multiphysics using a three-dimensional one-phase model. The CFD model solves the Reynolds-averaged Navier–Stokes (RANS) equations with a k-ϵ turbulence closure model. The RANS equation is presented in Equation 5.3, and the general equations of the k - ϵ turbulence closure model are provided in Equation 5.4 till 5.8.

$$\rho\frac{\partial \mathbf{u2}}{\partial t} + \rho(\mathbf{u2}\cdot\nabla)\mathbf{u2} = \nabla\cdot[-p\mathbf{l}+\mathbf{K}] + \mathbf{F} + \rho\mathbf{g} \tag{5.3}$$

where ρ represents the density of water (kg/m^3), $u2$ the velocity field (m/s), l the shear rate viscosity (Pa $\cdot$ s), p the pressure (N/m^2), k the turbulence kinetic energy (m^2/s^2) and F the volume force field (N/m^3).

$$\rho\nabla\cdot\mathbf{u2} = 0 \tag{5.4}$$

$$\mathbf{K} = \left(\mu + \mu_\tau\right)\left(\nabla\mathbf{u2} + (\nabla\mathbf{u2})^\top\right) \tag{5.5}$$

where μ_T the turbulent viscosity [(N/m2) $\cdot$ s]

$$\rho\frac{\partial k2}{\partial t} + \rho(\mathbf{u2}\cdot\nabla)k2 = \nabla\cdot\left[\left(\mu + \frac{\mu_T}{\sigma_k}\right)\nabla k2\right] + P_k - \rho\epsilon \tag{5.6}$$

where ϵ represents the rate of dissipation of turbulence energy (m^2/s^3)

$$\rho\frac{\partial \varepsilon}{\partial t} + \rho(\mathbf{u2}\cdot\nabla)\varepsilon = \nabla\cdot\left[\left(\mu + \frac{\mu_T}{\sigma_\epsilon}\right)\nabla\epsilon\right] + C_{\epsilon 1}\frac{\epsilon}{k2}P_k - C_{\epsilon 2}\rho\frac{\epsilon^2}{k2}, \quad \epsilon = \text{ep2} \tag{5.7}$$

$$\mu_T = \rho C_\mu\frac{k2^2}{\epsilon} \tag{5.8}$$

The values of dimensionless constants $C_1 = 1.44$, $C_2 = 1.92$, $C_\mu = 0.09$, $\sigma_\epsilon = 1.3$ and $\sigma_k = 1$ are taken from Morse et al. (1972).

5.2.2. Mesh

A mesh covers a given shape or form, and subdivides it into non-overlapping elements. Functions are assigned to the specific elements. These functions can be calculated for the entire model by assembling the collection of all elements. In Figure 5.5a and 5.5b, the mesh of the block and the ducted system are presented. The mesh of the block is defined as 'fine', and the mesh of the ducted system is defined as 'extra fine'.

(a) Mesh Block defined as 'fine'

(b) Mesh ducted system defined as 'extra fine'
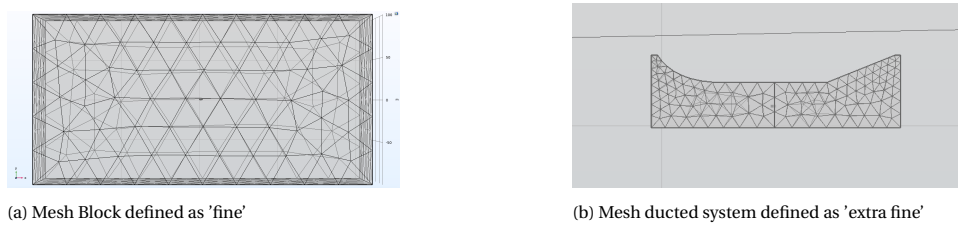
Figure 5.5: Mesh geometries

In Figures 5.6a, 5.6b, 5.6c, 5.6d and 5.6e, the information about the mesh elements is displayed. The minimum element quality is ±0.2225, ±0.2207, ±0.1001, ±0.1006 and ±0.1362 for the mesh of the straight, curved and high, mid & low frequency waved ramp simulations, respectively. This is sufficient as the rule of thumb indicates that a minimum element quality of at least 0.1 is necessary. The minimum element quality is lower for the waved designs since more detailed curvatures are present in these geometries.

(a) Straight ramp

(b) Curved ramp

(c) High Frequency Waved ramp

(d) Mid Frequency Waved ramp

(e) Low Frequency Waved ramp
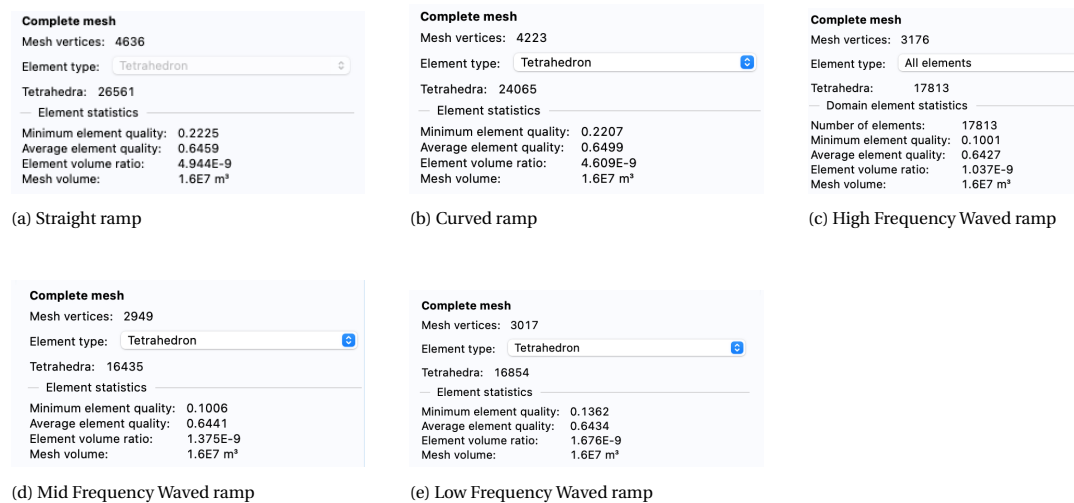
Figure 5.6: Mesh elements CFD simulations ramp designs

5.2.3. Validation CFD Model

In this section, the hydrodynamic model is validated. This is done by verifying the accuracy of the simulations. In case the accuracy is acceptable, the CFD model can be used to compare with the field experiments. Subsequently, the errors between the two approaches are calculated and discussed.

Accuracy

In Table 5.3, the volume entering the inflow plane and the volume leaving the outflow plane of the ducted system are shown per unit of time. As can be seen, there is a minimal loss of volume present in the model. The error is 1.56%, 1.83%, 0.93%, 1.82% and 2.1% for the straight, curved and high, mid & low frequency waved ramps, respectively. Other methods to investigate the accuracy of the CFD simulations are discussed and executed in Appendix I. Based on the accuracy check methods, it is concluded that these errors are acceptable, and therefore, the accuracy of the CFD models is approved.

Table 5.3: Time Integration Volume Check - CFD simulations

Ramp Design	Volume In [m^3/s]	Volume Out [m^3/s]	Error
Straight	3.91	3.85	1.56%
Curved	3.89	3.82	1.83%
High frequency Waved	3.95	3.92	0.93%
Mid frequency Waved	3.92	3.85	1.82%
Low frequency Waved	3.90	3.82	2.10%

Comparison

The data of the CFD simulations are compared with the field experiments to validate whether the CFD model can be used for further investigation. The comparison for each design was carried out by plotting the velocity inside the ducted system over the corresponding inlet velocity for the field experiments and the CFD simulations. This is presented in Figures 5.7a, 5.7b, 5.7c, 5.7d, 5.7e. These plots visualise the deviation between the two approaches.

(a) Straight Ramp

(b) Curved Ramp

(c) High Frequency Waved Ramp

(d) Mid Frequency Waved Ramp

(e) Low Frequency Waved Ramp
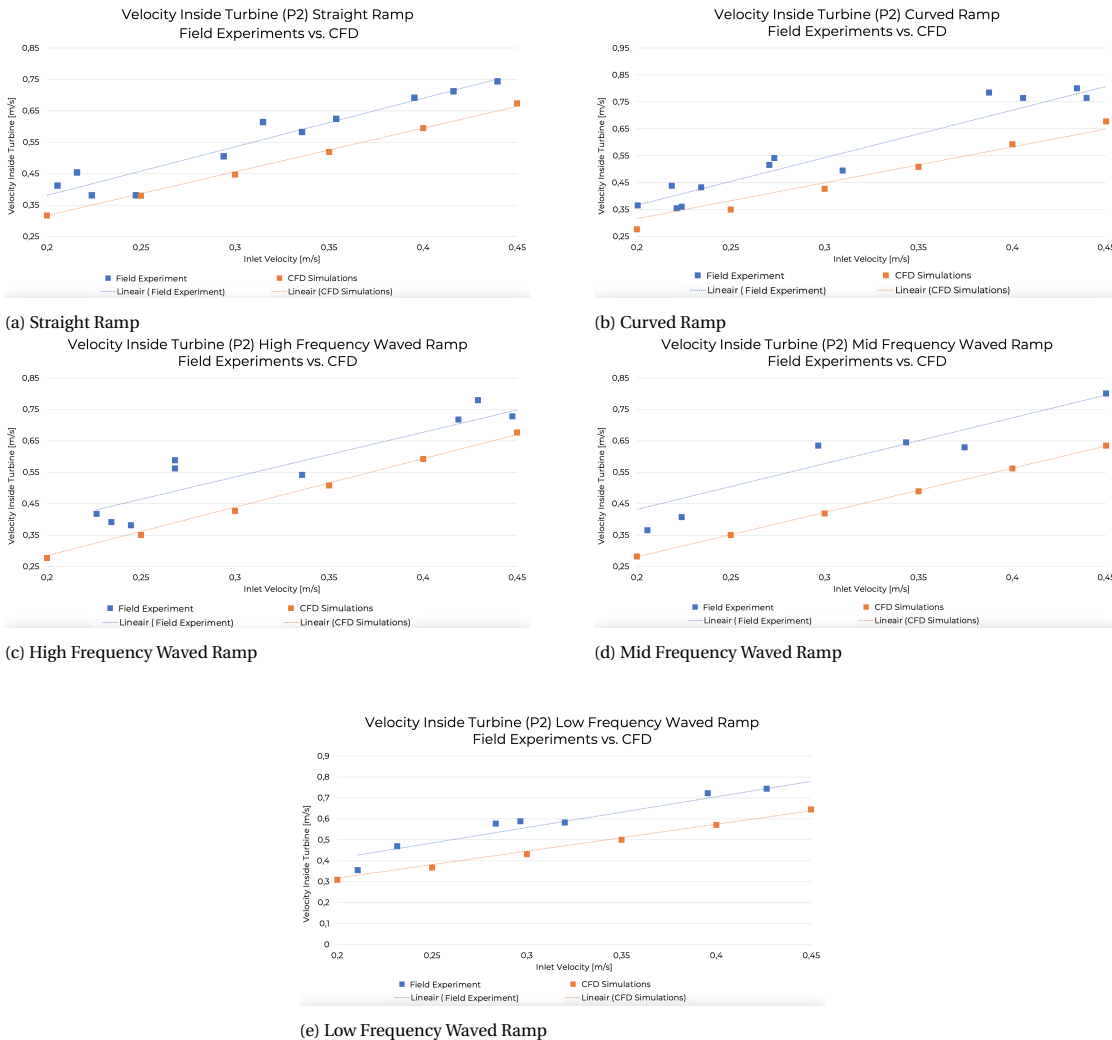
Figure 5.7: Velocity inside ducted system over inlet velocity for ramp designs for CFD simulations and field experiments

It is visible that the data of the field experiments are scattered. This is due to external factors that played a role during the field experiments. The factors are the movement of the prototype, the movement of the workboat during the experiments and the irregular retention of pressure by the air compressor. The data of the CFD simulations does not have a scattering behaviour. This is because the external factors are not present in CFD simulations.

For an increase in inlet velocity, an increase in velocity inside the ducted system can be found. The data of both approaches represent a similar trend. Based on the presented data, the errors between the field experiments and the CFD simulations are calculated and discussed next.

Error

In Table 5.4, the errors between the field experiments and the CFD simulations are presented. These errors are calculated by making use of Equation 5.9.

$$\% \text{ error } = \frac{| \text{ accepted value - experimental value } |}{\text{accepted value}} \tag{5.9}$$

Table 5.4: Overview error field experiments vs. CFD simulations - velocity inside ducted system at inlet velocity 0.45 m/s

Ramp Design	Velocity Field experiments [m/s]	Velocity CFD Simulations [m/s]	Error
Straight	0.75	0.65	15.4%
Curved	0.82	0.65	26.15%
High Frequency Waved	0.75	0.67	11.9%
Mid Frequency Waved	0.79	0.64	23.4%
Low Frequency Waved	0.78	0.65	20.0%

The error is found to be between 11.9% and 26.15%. This error could be minimised by calibrating the parameters. However, it was chosen not to adjust the parameters because it is unknown how to change the parameters for the model. Therefore, it was chosen to keep the input parameters that were found by Morse et al. (1972). The values of dimensionless constants are: $C_1 = 1.44$, $C_2 = 1.92$, $C_\mu = 0.09$, $\sigma_\epsilon = 1.3$ and $\sigma_k = 1$. It can be concluded that the error between the two approaches can be accepted. This is because the trends found in the CFD simulations are validated with the experimental data.

Now that the CFD model is validated, it can be used to study the hydrodynamics of the Van Rompay Turbine ducted system for higher velocities. The impact of turbulence kinetic energy and the flow velocity increase caused by the converging and diverging part is investigated. It should be noted that during the CFD simulations, a one-phase approach was used. The impact of the air chamber is therefore not included in the simulations. The behaviour of the air chamber should be studied in future research as this could have an impact on the data found.

5.2.4. Turbulence

The impact in terms of turbulence is investigated by measuring the turbulence kinetic energy. The turbulence kinetic energy (TKE) is the mean kinetic energy per unit mass. The kinetic energy in a turbulent flow is associated with eddies. Physically, the turbulence kinetic energy is characterised by measured root-mean-square (RMS) velocity fluctuations. In the Reynolds-averaged Navier Stokes equations, the turbulence kinetic energy can be calculated based on the closure method, i.e. a turbulence closure model.

The turbulence kinetic energy, k, is the kinetic energy per unit mass of the turbulent fluctuations u_i' in a turbulent flow. The SI unit of k is J/kg = m^2/s^2. The formula for turbulence kinetic energy is presented in Equation 5.10.

$$k \stackrel{\text{def}}{=} \frac{1}{2}\overline{u_i' u_i'} = \frac{1}{2}\left(\overline{u_x'^2} + \overline{u_y'^2} + \overline{u_z'^2}\right) = \frac{3}{2}\overline{u'^2} \tag{5.10}$$

where the turbulent velocity component is the difference between the instantaneous and the average velocity $u' = u - \overline{u}$, whose mean and variance are presented in Equation 5.11 and 5.12 respectively.

$$\overline{u'} = \frac{1}{T}\int_0^T (u(t) - \overline{u})\, dt = 0 \tag{5.11}$$

$$\overline{(u')^2} = \frac{1}{T}\int_0^T (u(t) - \overline{u})^2\, dt \geq 0 \tag{5.12}$$

TKE can be produced by fluid shear, friction, or through external forcing at low frequency eddy scales.

The turbulence kinetic energy is extracted from the simulations of the different designs. This is done by averaging the turbulence kinetic energy over the entire volume of the ducted system. This is presented in Figure 5.8.
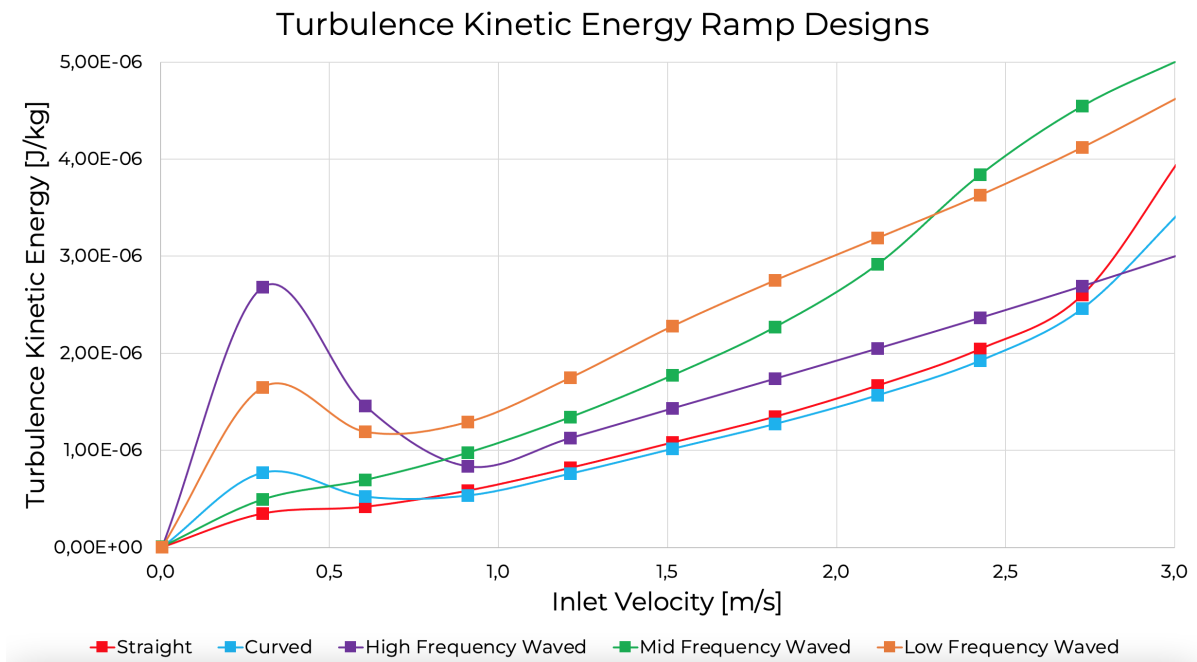
Figure 5.8: Turbulence Kinetic Energy (TKE) of the designs CFD simulation

The straight ramp represents the lowest magnitude of turbulence kinetic energy for lower velocities (0 m/s - 0.75 m/s) compared to the curved and high, mid & low frequency waved ramps. The curved ramp represents the lowest magnitude of turbulence kinetic energy for higher velocities (0.75 m/s - 3 m/s) compared to the straight and the high, mid & low frequency waved ramps.

It is found that the turbulence kinetic energy around 0.5 m/s shows a hump. The increase in turbulence kinetic energy at this point might be caused due to an increase of viscous stresses in the fluid as the blockage is occurring. The decrease of the hump displays the moment when the blockage is dissolved, and this results in a reduction of turbulence.

In Figures 5.9, 5.10, 5.11, 5.12 and 5.13 snapshots of the hydrodynamic CFD simulations at a velocity of 1, 2 and 3 m/s is presented for the different ramp designs. For each ramp design, a legend is attached from where the turbulence kinetic energy values can be read.

(a) Inlet velocity of 1 m/s   (b) Inlet velocity of 2 m/s   (c) Inlet velocity of 3 m/s   (d) Legend
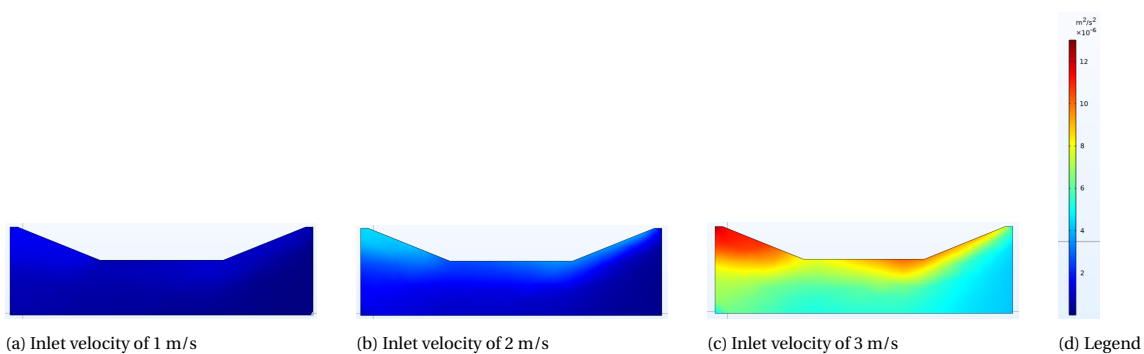
Figure 5.9: Snapshots of the Turbulence Kinetic Energy at 1 m/s, 2 m/s and 3 m/s for the straight ramp

(a) Inlet velocity of 1 m/s   (b) Inlet velocity of 2 m/s   (c) Inlet velocity of 3 m/s   (d) Legend
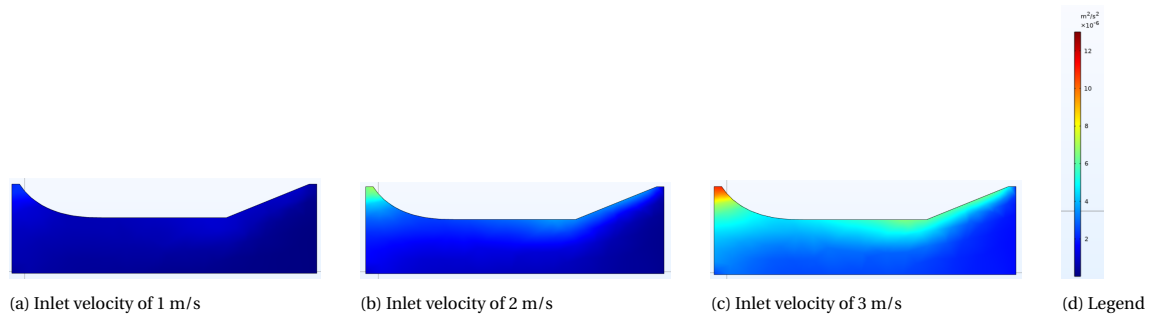
Figure 5.10: Snapshots of the Turbulence Kinetic Energy at 1 m/s, 2 m/s and 3 m/s for the curved ramp

(a) Inlet velocity of 1 m/s   (b) Inlet velocity of 2 m/s   (c) Inlet velocity of 3 m/s   (d) Legend
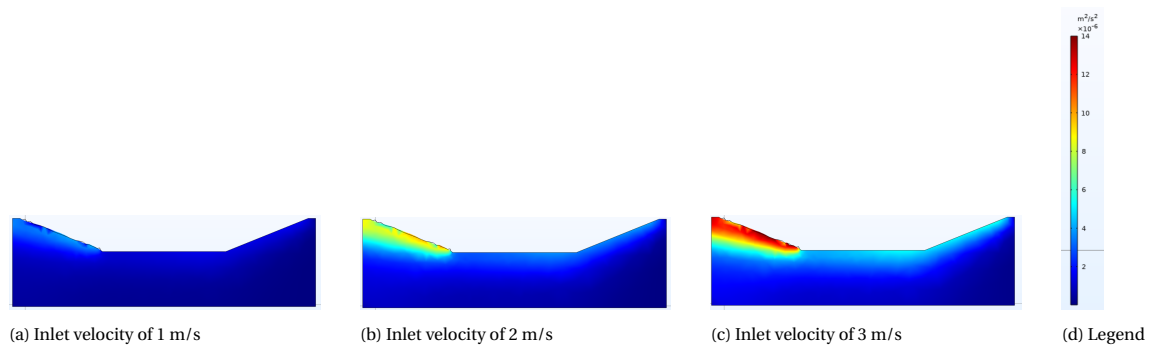
Figure 5.11: Snapshots of the Turbulence Kinetic Energy at 1 m/s, 2 m/s and 3 m/s for the high frequency waved ramp

(a) Inlet velocity of 1 m/s   (b) Inlet velocity of 2 m/s   (c) Inlet velocity of 3 m/s   (d) Legend
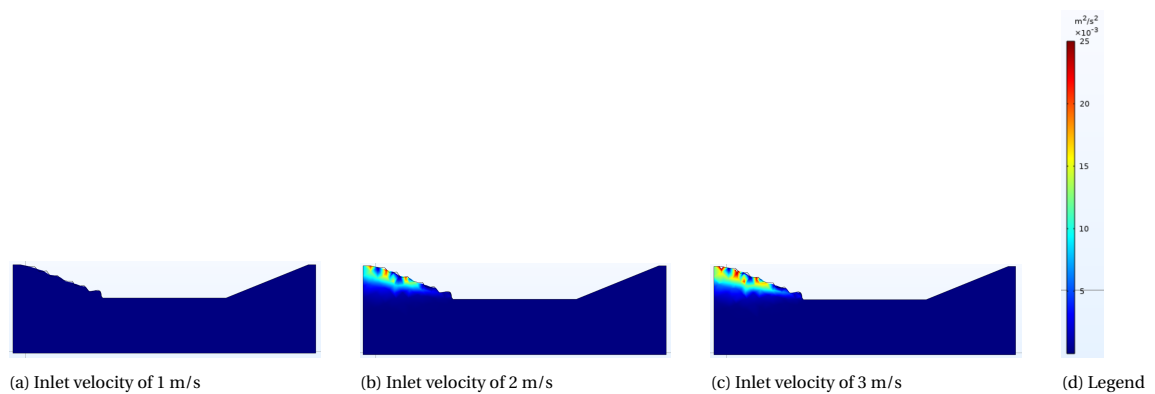
Figure 5.12: Snapshots of the Turbulence Kinetic Energy at 1 m/s, 2 m/s and 3 m/s for the mid frequency waved ramp

(a) Inlet velocity of 1 m/s   (b) Inlet velocity of 2 m/s   (c) Inlet velocity of 3 m/s   (d) Legend
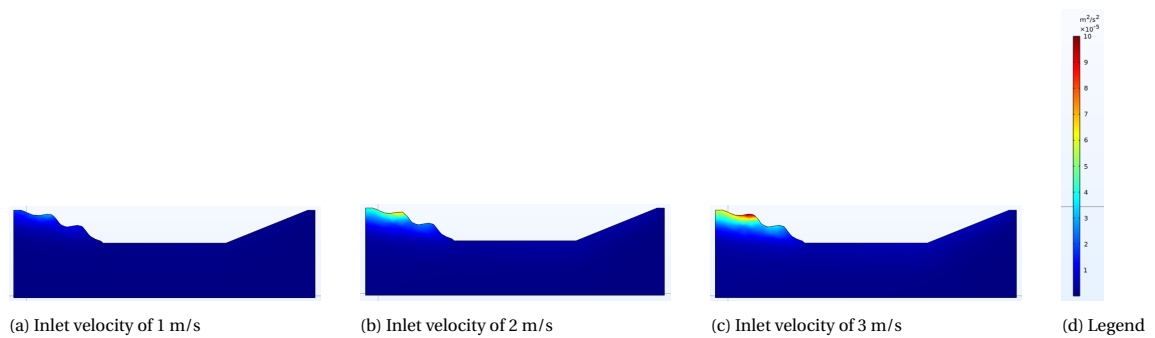
Figure 5.13: Snapshots of the Turbulence Kinetic Energy at 1 m/s, 2 m/s and 3 m/s for the low frequency waved ramp

Based on the snapshots, it is visible that turbulence is mainly generated in the inlet because at this location, the water is confronting the ramp in the converging section. Inside the ducted system, the magnitude of turbulence is reduced. This is because when the cross-sectional area decreases, the velocity fluctuations become smaller compared to the average velocity. This causes a considerable flattening of the velocity profile and results in a lower magnitude of turbulence (Deutz, 2003). The water flowing through the diverging segment experienced a considerable increase in turbulence levels. The flow is subject to an adverse pressure gradient which is strong enough to cause separation of the mean flow and thus increasing turbulence (Deutz, 2003).

Another visible phenomenon is the increase in turbulence kinetic energy when increasing the inlet velocity. The drag between adjacent layers of water flow and between the water flow and the ducted system form more vortices for higher velocities.

The waved designs result in a drag reduction for lower velocities (Tomiyama and Fukagata, 2013). This is caused due the quasi-streamwise vortices are moved away from the wall and weakened. The weakened quasi-streamwise vortices produce fewer shear stresses and the reduced shear stresses result in drag reduction (Tomiyama and Fukagata, 2013). This mechanism is elaborated on in Appendix K. For higher velocities, the drag reduction is less significant. This is because the quasi-streamwise vortices get closer to the wall in case of higher velocities and are therefore less weakened.

The design of the curved ramp is a smooth and gradual transition to the smaller region. This smooth transition entails lower magnitudes of turbulence. How these waved and curved designs affect the flow velocity increase is presented in Section 5.2.5.

In Table 5.5, an overview is presented of the turbulence kinetic energy for each ramp design. As can be seen, the curved ramp represents the lowest overall turbulence kinetic energy.

Table 5.5: Average Turbulence Kinetic Energy Ramp Designs - CFD simulations

Ramp Design	Wave Length	Wave Height	Turbulence Kinetic Energy [J/kg]
Straight	N.A	N.A	1.36E-06
Curved	$\lambda = 1200$ mm	H = 120 mm	1.30E-06
High Frequency Waved	$\lambda = 70$ mm	H = 19 mm	1.76E-06
Mid Frequency Waved	$\lambda = 180$ mm	H = 50 mm	5.94E-05
Low Frequency Waved	$\lambda = 420$ mm	H = 90 mm	2.41E-06

5.2.5. Flow Velocity Increase

The flow velocity increase is calculated with Equation 5.13. This parameter represents the degree of acceleration caused by the converging inflow.

$$\text{Flow Velocity Increase} = 100 \cdot \frac{\text{Velocity Inside the ducted system}}{\text{Inlet Velocity}} - 1 \tag{5.13}$$

In Figure 5.14, the flow velocity increase of the different inflow ramp designs are presented over an inlet velocity between 0 and 3 m/s. This flow velocity increase can be explained by the Continuity Equation. The continuity Equation 5.14 states that the flow rate in point 1 equals the flow rate in point 2. If the cross-section gets smaller, the flow velocity increases, and vice versa.

$$A_1 v_1 = A_2 v_2 \tag{5.14}$$

We can see in Figure 5.14 that the velocity increase occurs for all the ramp designs as the cross-sectional area decreases.
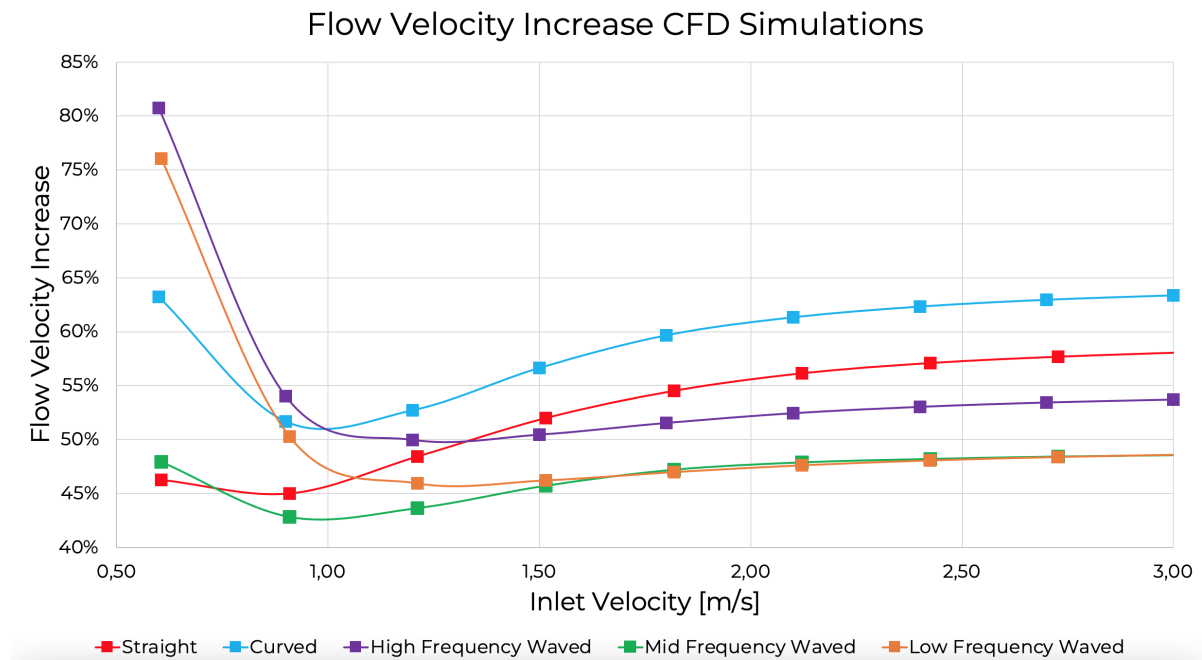
Figure 5.14: Flow velocity increase ramp designs CFD simulations

It is remarkable that the flow velocity increase between 0.5 and 1 m/s is relatively high. This is caused due to for lower inlet velocities; the turbulence profile is more spatially distributed. For higher velocities, more turbulence is generated, and this implicates a more uniformly profile distribution. It can therefore be stated that the first points found in the plot represent an inaccurate result.

As was found during the field experiments in Section 5.1.2, a higher flow velocity increase was found for the waved designs for lower velocities. This is confirmed by the CFD simulations presented in Figure 5.14. This increase in flow velocity can be explained based on prior studies about streamwise wavy walls. Quadrio et al. (2009) researched the response of a turbulent channel flow to sinusoidal waves of spanwise velocity applied at the wall and travelling along the streamwise direction. It was concluded in this research that drag reduction was present when streamwise wavy walls were applied. This has a direct impact on the velocities found in the ducted system. As turbulent levels are reduced, higher velocities can be achieved. Turbulence causes energy losses due to quasi-streamwise vortices, which reduces the energy levels.

The mechanism behind the turbulent reduction is due to the spanwise wall motion. The pumping effect induces the spanwise flow in the vicinity of the wall: above the trough, a strong flow is induced in the same direction as the travelling wave; above the crest, a weaker flow is induced in the opposite direction. This induced flow above the trough shields quasi-streamwise vortices from the groove; namely, the quasi-streamwise vortices are moved away from the wall and weakened. The weakened quasi-streamwise vortices produce fewer anomalies Reynolds shear stresses, and the reduced random Reynolds shear stresses result in drag reduction (Tomiyama and Fukagata, 2013). This mechanism is elaborated on in Appendix K.

The research of Quadrio et al. 2009 has shown that this mechanism has more impact at lower velocities. This is because the quasi-streamwise vortices get closer to the wall in case of higher velocities and are therefore less weakened. This phenomenon is visible in the results. At lower velocities (0.5-1 m/s) the flow velocity of the waved ramps are higher. For higher velocities, it was found that the curved ramp represents a higher flow velocity increase. Therefore, it can be confirmed that for higher velocities, the mechanism of drag reduction is less effective for waved designs.

The study of Quadrio et al. (2009) also concluded that drag reduction appears to increase with the wave amplitude. This is the case between the low frequency waved ramp and the mid frequency waved ramp. The amplitude of the low frequency waved ramp is 90 mm. It has an average flow velocity increase of 51%, whereas the amplitude of the mid frequency waved ramp is 50 mm and has an average flow velocity increase

of 47%. Remarkable is that for the high frequency waved ramp, which has an amplitude of 19mm, an average flow velocity increase of 55% is found. This can be explained because more wave periods are present for the high frequency waved ramp. For high periods, more interaction is present, and the turbulent flow is moved away from the wall region. Therefore, the high frequency waved design has more impact on the turbulent reduction, and higher flow velocities are present compared to the other two waved ramps.

As was found in the field experiments, the curved ramp shows a higher flow velocity increase for higher velocities. This is because the pressure gradient drops exponentially due to the curved shape. The pressure drop between the converging part and inside the ducted system has a smooth transition due to the gradual transition to the smaller region which causes fewer losses (Zerpa et al., 2019). Therefore, the curved ramp represents the highest flow velocity increase, with an average flow velocity increase of 59%. This is an increase of 6% compared to the straight ramp.

In Table 5.6, a summary of the different ramp designs are shown including their corresponding average flow velocity increase.

Table 5.6: Average Flow Velocity Increase Ramp Designs - CFD simulations

Ramp Design	Wave Length	Wave Height	Average Flow Velocity Increase
Straight	N.A	N.A	53%
Curved	$\lambda = 1200$ mm	H = 120 mm	59%
High Frequency Waved	$\lambda = 70$ mm	H = 19 mm	55%
Mid Frequency Waved	$\lambda = 180$ mm	H = 50 mm	47%
Low Frequency Waved	$\lambda = 420$ mm	H = 90 mm	51%

5.3. Phase 3: Scaling Up

In this phase, the CFD model of the curved design is used to study how the hydrodynamics of the ducted system of the Van Rompay are affected when scaling up the dimensions. The small curved design is used throughout this phase because this design represents the lowest energy losses in the system compared to the other tested designs. This model is therefore used to scale up the dimensions with a factor 2 and a factor 10. The main dimensions of factors 1, 2 and 10 can be found in Tables 5.7, 5.8 and 5.9.

Table 5.7: Dimensions factor 1

Measurements	Value
Length	4.05 m
Width	1.17 m
Height	1.17 m
Inflow Area	1.37 m^2

Table 5.8: Dimensions factor 2

Measurements	Value
Length	8.1 m
Width	2.34 m
Height	2.34 m
Inflow Area	5.5 m^2

Table 5.9: Dimensions factor 10

Measurements	Value
Length	40.5 m
Width	11.7 m
Height	11.7 m
Inflow Area	136.9 m^2

5.3.1. Turbulence Closure Model

Similar to the previous phase, the hydrodynamic CFD model is solved by the Reynolds-averaged Navier–Stokes (RANS) equations with a k - ϵ turbulence closure model. This is explained in section 5.2.1.

5.3.2. Mesh

In Figure 5.15a, 5.15b and 5.15c, the mesh of the block and the ducted system of the scaling factor 1, 2 and 10 are shown. The mesh of the block is coarser than the mesh of the geometry of the ducted system. The difference in mesh size is chosen because the hydrodynamics close to the Van Rompay Turbine ducted system is more of interest. Therefore, it should be calculated with more accuracy. Note that the air chamber is not modelled. This could influence the magnitude of turbulence present inside the system.

(a) Mesh Factor 1   (b) Mesh Factor 2   (c) Mesh Factor 10
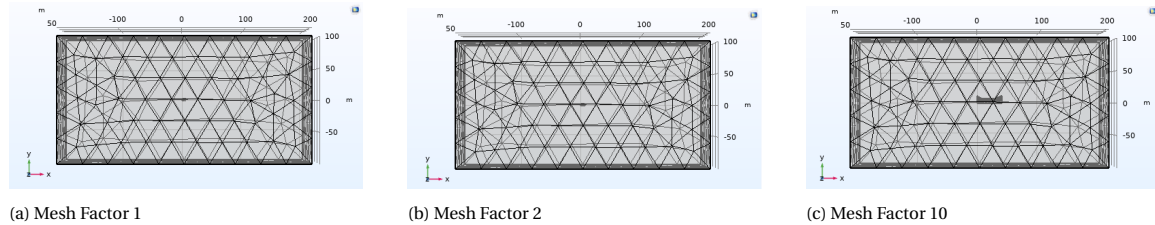
Figure 5.15: Mesh size scaled up turbines CFD simulations

In Table 5.10, an overview of the mesh sizes are shown for each scaling factor.

Table 5.10: Mesh Size ducted system and block - CFD simulations

Factor	Ducted System Mesh Size	Block Mesh Size
Factor 1	Fine	Normal
Factor 2	Finer	Normal
Factor 10	Extra Fine	Normal

In Figures 5.16a, 5.16b and 5.16c, information about the elements is presented. The minimum element quality is ±0.2225, ±0.1952 and ±0.1851 for the factor 1, factor 2 and factor 10 simulations, respectively. This is sufficient as the rule of thumb says that a minimum element quality of at least 0.1 is necessary. Further investigation of the accuracy of these simulations is explained and discussed in Appendix J.

(a) Mesh Elements Factor 1   (b) Mesh Elements Factor 2   (c) Mesh Elements Factor 10
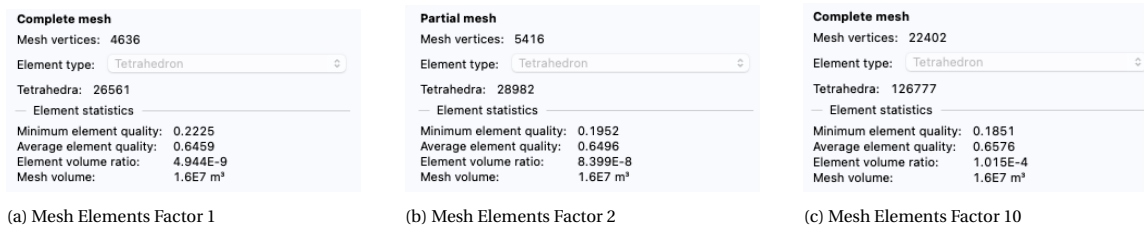
Figure 5.16: Mesh Elements scaled up turbines CFD simulations

5.3.3. Turbulence CFD Scaling

The magnitude of turbulence kinetic energy is extracted from the simulations after scaling up the ducted system with factors 1, 2 and 10. This is done by averaging the turbulence kinetic energy over the entire volume of the ducted system. The magnitude of the turbulence kinetic energy is presented in Figure 5.17.
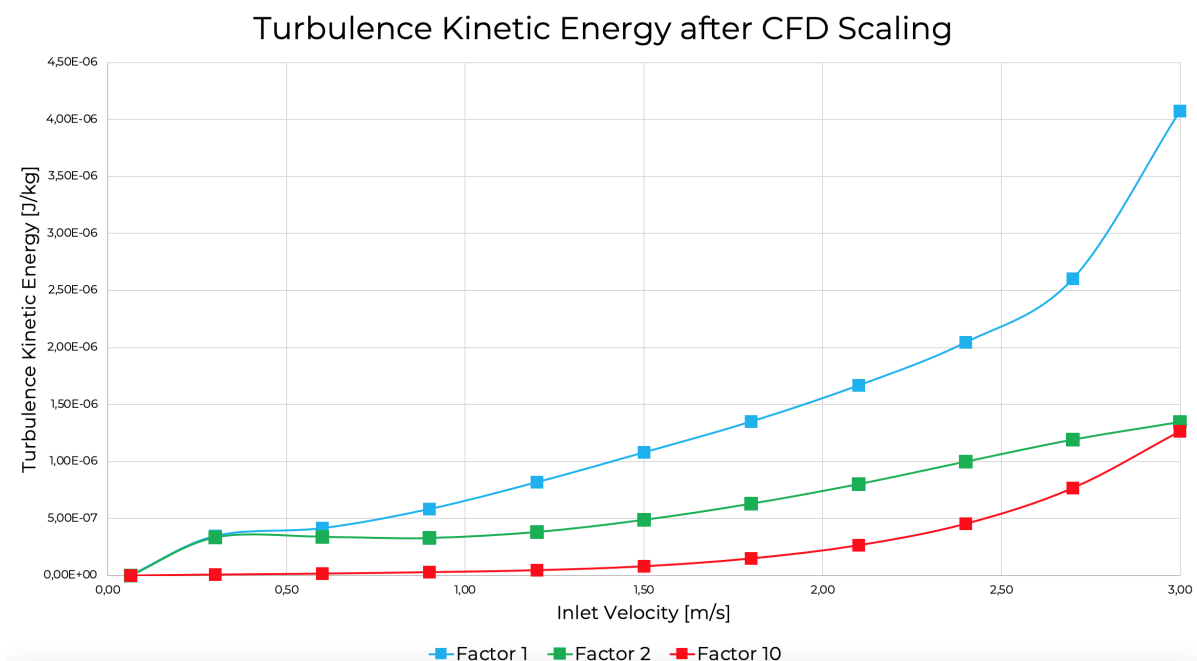
Figure 5.17: Turbulence Kinetic Energy (TKE) for scaled up ducted system factor 1, 2 and 10

It can be concluded that when scaling up the ducted system, a lower magnitude of turbulence kinetic energy is present per cubic meter. This can be explained since larger systems have a marginal lower specific surface of contact between the water and the duct. This is visible in Figure 5.17 as the average turbulence kinetic energy is measured over the entire volume of the ducted system. However, the total magnitude of turbulence kinetic energy present in the entire ducted system increases for larger systems.

The magnitude of turbulence kinetic energy of factor 2 and factor 10 are close to each other compared to factor 1 ducted system. This implies that the system could be optimised regarding the amount of turbulence and the size of the system based on a cost-benefit analysis. This is because a non-linear increase in turbulence is found when scaling up the dimensions. This optimum could be found in future research.

In Figures 5.18, 5.19 and 5.20 the snapshots of the hydrodynamic CFD simulations at a velocity of 1, 2 and 3 m/s is presented for the different scaling factors. For each factor, a legend is attached from where the turbulence kinetic energy values can be read.

(a) Inlet velocity of 1 m/s   (b) Inlet velocity of 2 m/s   (c) Inlet velocity of 3 m/s   (d) Legend
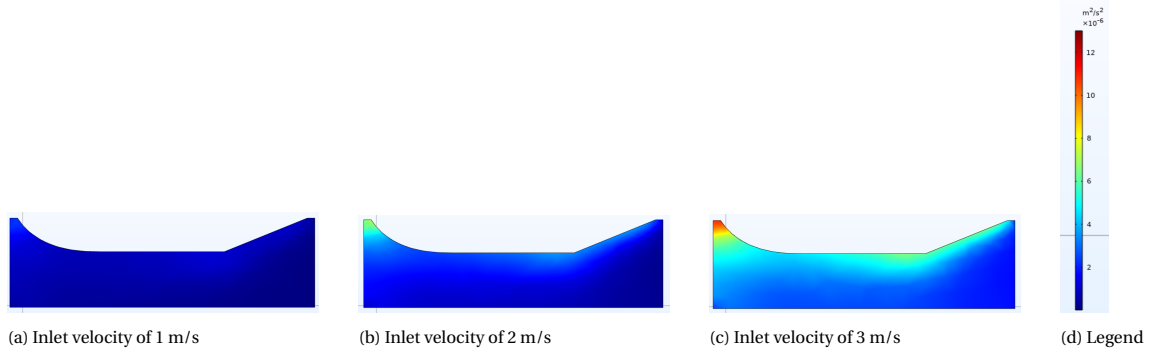
Figure 5.18: Snapshots of the Turbulence Kinetic Energy at 1 m/s, 2 m/s and 3 m/s for scaling factor 1

(a) Inlet velocity of 1 m/s   (b) Inlet velocity of 2 m/s   (c) Inlet velocity of 3 m/s   (d) Legend
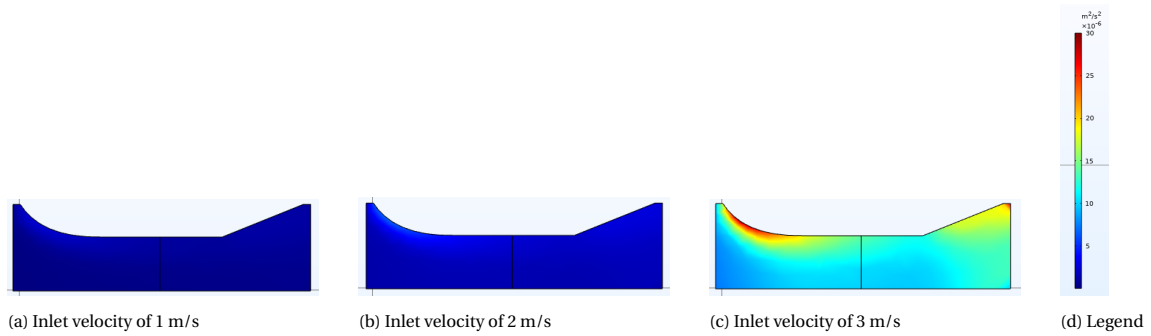
Figure 5.19: Snapshots of the hydrodynamic CFD simulation at several velocities for scaling factor 2

(a) Inlet velocity of 1 m/s   (b) Inlet velocity of 2 m/s   (c) Inlet velocity of 3 m/s   (d) Legend
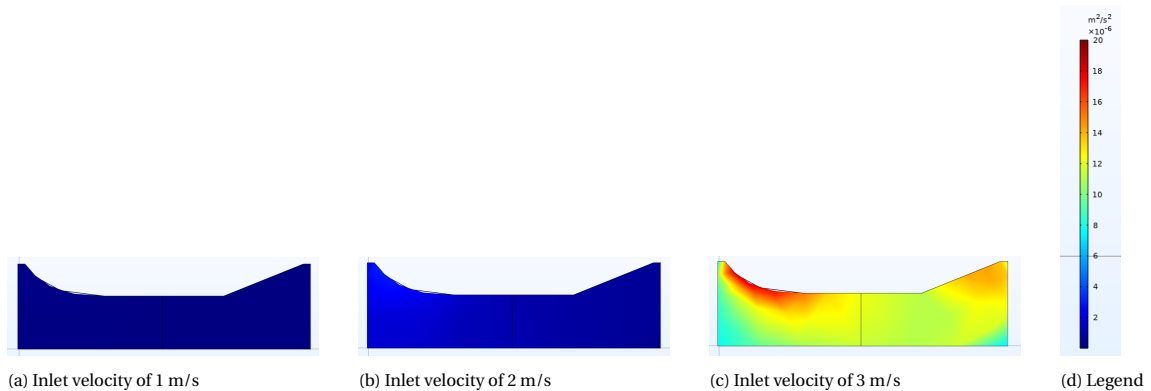
Figure 5.20: Snapshots of the hydrodynamic CFD simulation at several velocities for scaling factor 10

Similar to Section 5.2.4, the turbulence is mainly generated in the inlet because at this location, the water is confronting the ramp. Inside the ducted system, the magnitude of turbulence is reduced. This is because when the cross-sectional area decreases, the velocity fluctuations become smaller compared to the average velocity. This causes a considerable flattening of the velocity profile and results in a lower magnitude of turbulence (Deutz, 2003). Water flowing through the diverging segment experienced a considerable increase in turbulence levels. The flow is subject to an adverse pressure gradient which is strong enough to cause separation of the mean flow and thus increasing turbulence (Deutz, 2003).

Similar to Section 5.2.4, an increase in turbulence kinetic energy is found when increasing the inlet velocity. The drag between adjacent layers of water flow and between the water flow and the ducted system form more vortices for higher velocities.

It is visible that the boundary layers in the converging part increase in thickness and in length when scaling

up the dimensions. This is because, for longer walls, more interaction between the water flow and the wall is caused. The particles in the layer closest to the wall encounter skin friction and reduce in velocity. They apply a shear force to the layer immediately above them due to viscosity, which slows them down, which in turn slows down the layer above it and so on. This causes more and larger eddies, resulting in a longer and thicker boundary layer. This entails that more energy to be lost in the water, which negatively impacts the flow velocity increase. How the turbulence kinetic energy impacts the flow velocities for the different scaled up ducts is presented in Section 5.3.4.

In Table 5.11, an overview is presented of the magnitude of the turbulence kinetic energy for each scaling factor. As can be seen, the factor 10 represents the lowest turbulence kinetic energy compared to the factor 1 and factor 2 ducted system. Note that the turbulence kinetic energy indicates the mean kinetic energy per unit mass associated with eddies in turbulent flow.

Table 5.11: Overview Results Average Flow Velocity Increase Scaling Up Experiments

Factor	Average Turbulence Kinetic Energy [J/kg]
Factor 1	1.3E-06
Factor 2	6.2E-07
Factor 10	2.8E-07

5.3.4. Flow Velocity Increase CFD scaling

The flow velocity increase is again calculated with Equation 5.1. This increase is calculated over a range between 0 and 3 m/s for a scaling factor 1, 2 and 10. This is plotted in Figure 5.21.
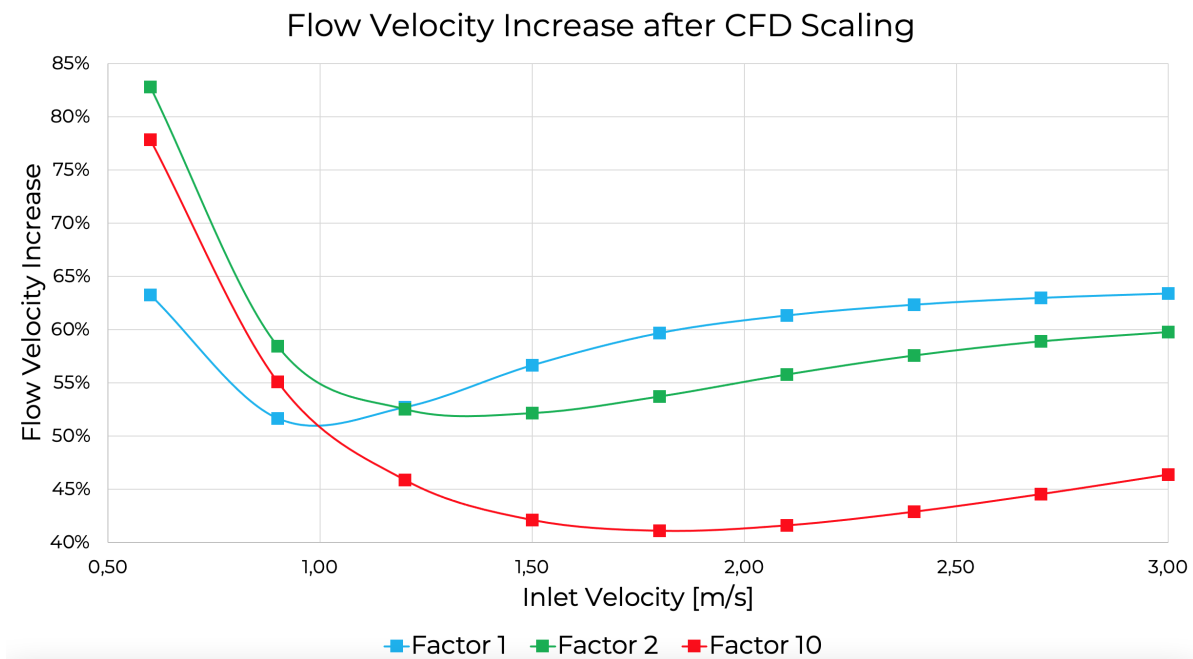
Figure 5.21: Average Turbulence Kinetic Energy scaling up - CFD simulations

For lower velocities (0 m/s - 1.25 m/s), the factor 1 ducted system represents a lower flow velocity increase compared to the scaling factors 2 and 10. This is due to more restrictions are present which causes more turbulence for lower velocities. This results in more losses and thus a lower flow velocity increase.

It was found in Section 5.3.3 that for longer walls, more interaction is experienced between the water flow and the wall, which causes more energy to be lost. Therefore, larger ducted systems results in a lower flow velocity increase. In Table 5.12, an overview is presented of the flow velocity increase for each scaling factor.

As can be seen, the factor 10 represents the lowest average flow velocity increase compared to the factor 1 and factor 2 ducted system.

Table 5.12: Average Flow Velocity Increase Scaling up - CFD simulations

Factor	Average Flow Velocity Increase
Factor 1	59%
Factor 2	59%
Factor 10	49%

When increasing the dimensions of the turbine, lower flow velocity increases can be found. In the next chapter, this data is used to estimate the available water flow power inside the turbine.

5.3.5. Available Power

The conservation of energy is a fundamental concept of fluid dynamics. Within some problem domains, the amount of energy remains constant. Energy can be converted from one form to another (potential energy can be converted to kinetic energy), but the total energy within the domain remains fixed.

The energy balance in steady-state for the control volume is presented in Equation 5.15.

$$\Delta E_k + \Delta E_P + \Delta U = \sum_{\text{input streams}} m_j \left(\hat{H}_j + \frac{u_j^2}{2} + g z_j \right) - \sum_{\text{output streams}} m_j \left(\hat{H}_j + \frac{u_j^2}{2} + g z_j \right) + Q - W_s \qquad (5.15)$$

Where E_k is the kinetic energy [J/kg], ΔE_P is the potential energy [J/kg] and ΔU is other work gained or lost to the system [J/kg], m_j is the mass [kg], $\hat{H}_j$ is the enthalpy [J/kg] (summation of internal energy U and pressure work $p \cdot V$) and Q is the heat rate into the system [J] and W_s is the rate of work done by the system [J].

There is no change in potential energy between the input and output stream in the ducted system as the depth of the two points stays constant; this causes the $g z_j$ terms to be neglected. The thermodynamic effects are minimal; therefore, the change in internal energy is negligible. There is no heat added to the system (Q), and there is no external work performed in the system (Ws). This entails that only the velocity terms and the pressure terms are needed.

The formula to calculate the power production can be found in Equation 5.16. Kinetic energy, in the form of velocity, is provided as input energy in the CFD simulations at the inflow plane of the block. This energy, when entering the duct, will partly be converted into pressure energy. As velocity increases in the ducted system due to the converging segment, the kinetic energy increases. However, this increase is balanced out by a pressure decrease. The pressure and kinetic energy represent the available power inside the ducted system. It can be seen that the pressure and the kinetic energy are multiplied with the flow rate Q [m^3/s].

$$P[W] = Q \cdot \left(\frac{1}{2} \cdot \rho \cdot v^2 + P \right) \qquad (5.16)$$

The ducted system is submerged sufficiently to avoid influence of the boundary conditions in the CFD simulations. In the field, the ducted system should be installed at the water level. Therefore, in the power equation 5.16, the total pressure (P) should not contain the hydrostatic pressure as the power that is caused due to the depth of the ducted system in the simulations should be filtered out.

The available power is calculated at three planes in the ducted system: the inflow plane, the plane inside the ducted system and the plane at the outflow. These planes are presented in Figure 5.22.
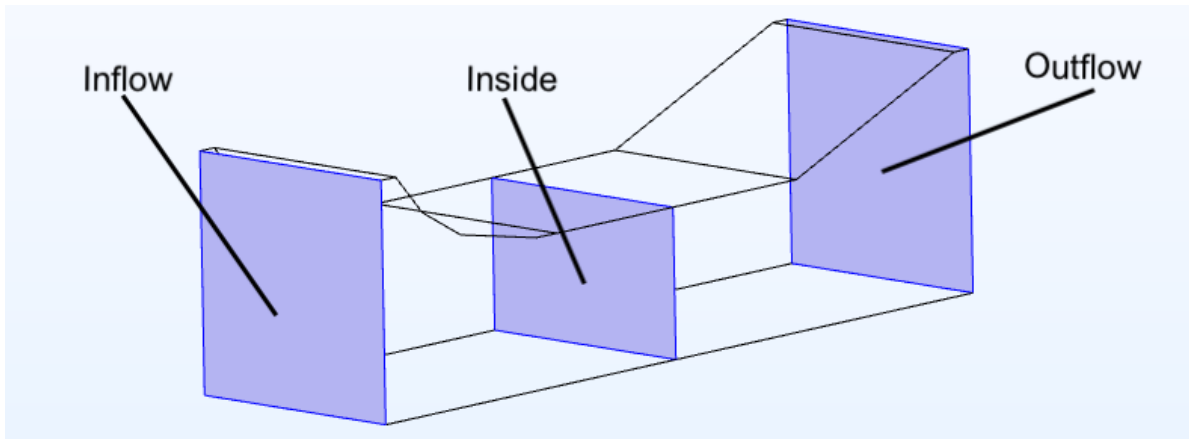
Figure 5.22: Planes in ducted system

In Figure 5.23, the available power [kW] of a scaled-up ducted system with factor 1 is presented. It is found that for 1 m/s, 2 m/s and 3 m/s, the available power is equal to 8.7 kW, 19.2 kW and 36.4 kW, respectively. It is visible that the inflow plane's power is higher than the power inside the ducted system. In turn, the power inside the ducted system is higher than the power at the outflow plane. This is because energy losses (turbulence and friction) occur when converging and diverging the flow. This is discussed and presented in Section 5.3.3.
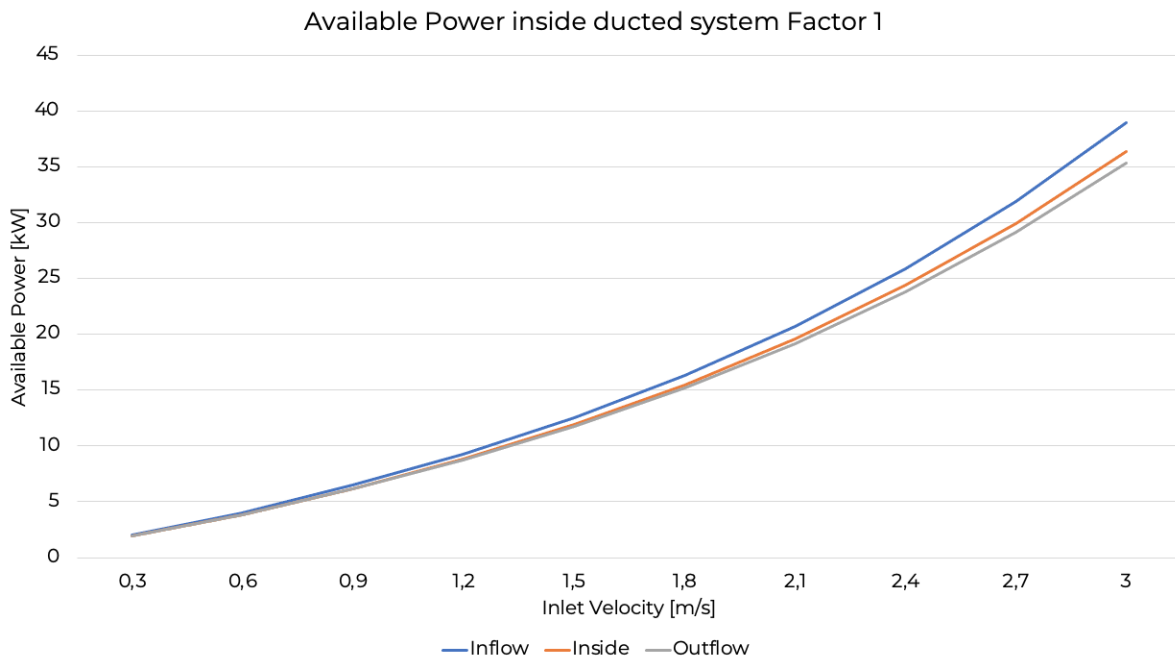
Figure 5.23: Available Power Factor 1

In Figure 5.24, the available power [kW] of a scaled-up ducted system with factor 2 is presented. Similar to factor 1, it is visible that the power at the inflow plane is higher compared to the power inside the turbine. And that in turn, the power inside the ducted system is higher than the power at the outflow plane. It is found that for 1 m/s, 2 m/s and 3 m/s, the available power is equal to 33.5 kW, 77.0 kW and 144.1 kW, respectively.

Available Power ducted system Factor 2
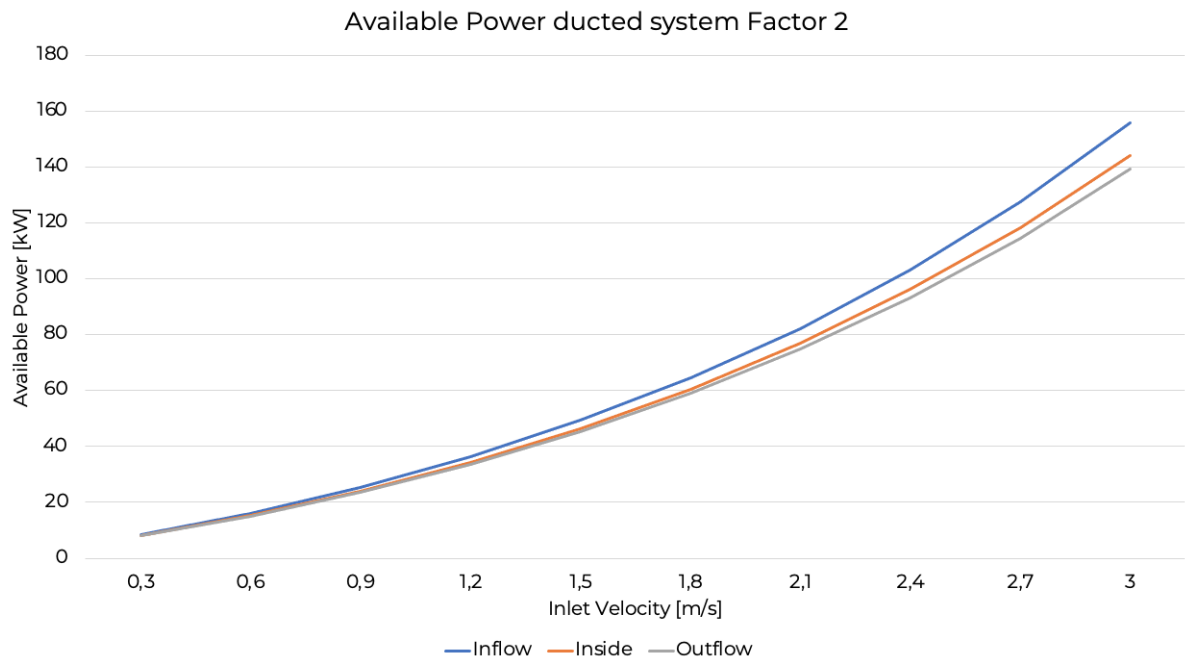
Figure 5.24: Available Power Factor 2

In Figure 5.25, the available power [kW] of a scaled-up ducted system with factor 10 is presented. Similar to factor 1 and factor 2, it is visible that the power at the inflow plane is higher compared to the power inside the turbine. Moreover, in turn, the power inside the turbine is higher than the power at the outflow. It is found that for 1 m/s, 2 m/s and 3 m/s, the available power is equal to 743.1 kW, 1675.1 kW and 3282.8 kW, respectively.

Available Power ducted system Factor 10
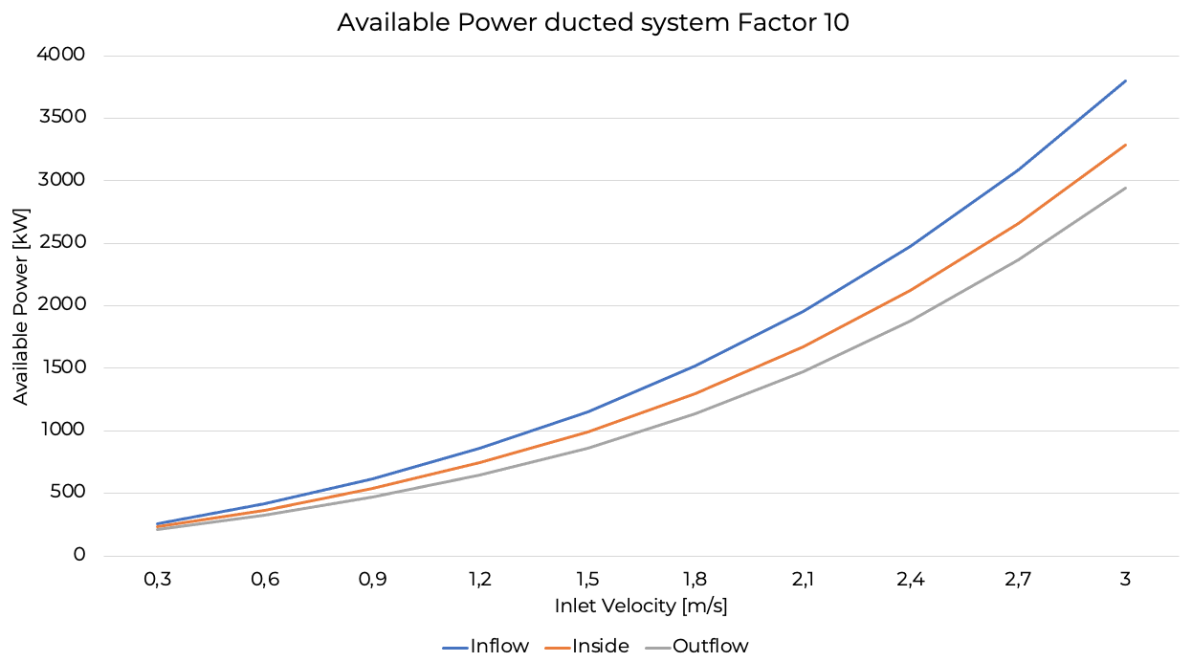
Figure 5.25: Available Power Factor 10

It is visible that the deviation between the inflow plane, inside the ducted system and the outflow plane increases for higher scaling factors. This is because, as explained in Section 5.3.3, the total magnitude of turbulence of the entire ducted system is larger for larger systems and therefore more energy is lost.

In Figure 5.26, the available power inside the ducted system for a factor 1, 2 and 10 are presented over a velocity range between 0 m/s and 3 m/s.
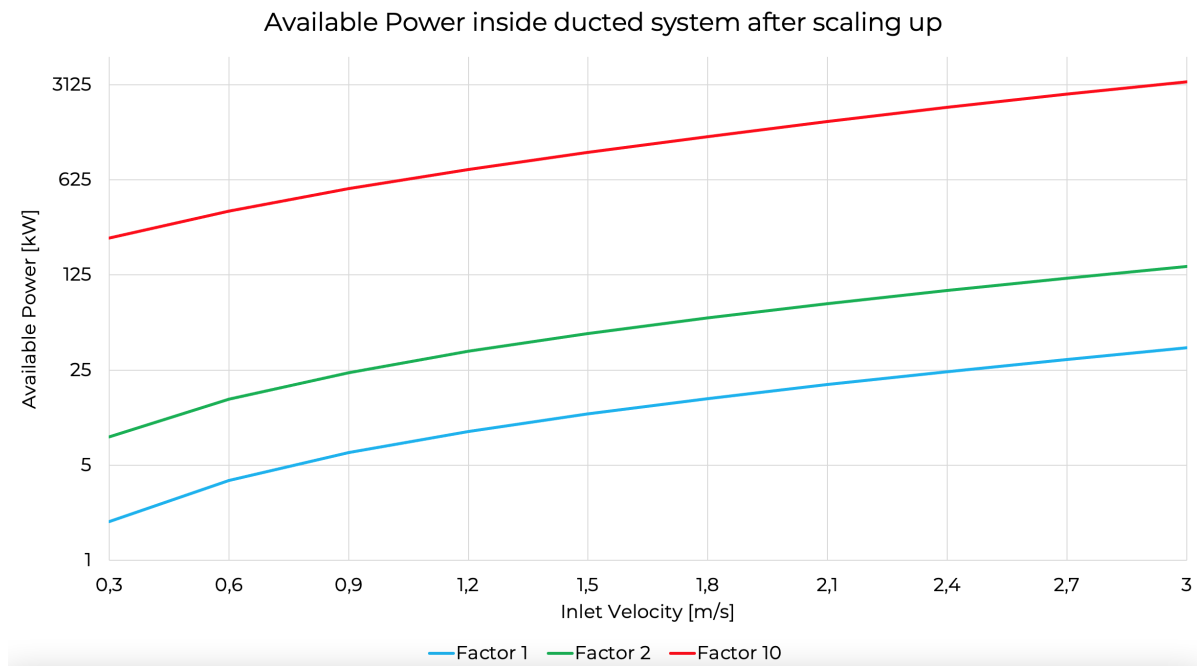
Figure 5.26: Available Power inside ducted system factor 1, 2 and 10 - logarithmic scale

In Table 5.13, an overview of the power available inside a ducted system with scale factors 1, 2 and 10 are presented for an inlet velocity of 1 m/s, 2 m/s and 3 m/s. For higher velocities, more energy is available as the kinetic energy increases. Another factor that increases the available power is the scaling up of the ducted system. Scaling up allows that more volumes can enter the ducted system and therefore, more power is present. This makes the duct of the Van Rompay turbine interesting as this can be scaled up depending on the site where the Van Rompay Turbine will be deployed.

Table 5.13: Water flow power inside ducted system for factor 1, 2 and 10

Factor	Water Flow Power [kW] at 1 m/s	Water Flow Power [kW] at 2 m/s	Water Flow Power [kW] at 3 m/s
Factor 1	8.7	19.2	36.4
Factor 2	33.5	77.0	144.1
Factor 10	743.1	1675.1	3282.8

The ducted system allows to collect energy in a small place, however, enough power should be available in the free water stream to provide enough force to overcome specific pressures the ducted system. In case the force provided by the free water flow cannot overcome the pressure of the ducted system, a hydrokinetic turbine that captures energy directly from the free water stream is more favourable.

There is a limit to the amount of energy that can be extracted from tidal flows (Shives and Crawford, 2010b). In case the inflow area of the free water flow does not meet the minimum area required to overcome the specific pressure in the ducted system, less water flow will enter the system as there is not enough energy to be concentrated in the duct. This results in a lower magnitude of available power in the system. Therefore, the potential available energy for generation also depends the location where the Van Rompay will be deployed. Different locations provide a different flow area and flow velocity. To calculate the available power in more detail, the boundary conditions of the CFD simulation should be adjusted based the location of deployment.

The required inflow area to obtain the available power for the factor 10 ducted system, shown in Table 5.13, is

equal to 40,000 m^2. Based on the power formula, shown in Equation 5.17, the minimal area for the different velocities can be calculated.

$$P_{\text{water flow}} = \frac{1}{2} \cdot \rho \cdot A_{\min} \cdot v^3 \tag{5.17}$$

The minimal area is calculated for an inlet velocity of 1 m/s, 2 m/s and 3 m/s, respectively.

$$A_{\min} = \frac{743.1\text{kW}}{\frac{1}{2} \cdot 1000 \cdot 1^3} = 1486.2\text{m}^2$$

$$A_{\min} = \frac{1675.1\text{kW}}{\frac{1}{2} \cdot 1000 \cdot 2^3} = 418.8\text{m}^2$$

$$A_{\min} = \frac{3282.8\text{kW}}{\frac{1}{2} \cdot 1000 \cdot 3^3} = 243.2\text{m}^2$$

It is found that for an inlet velocity of 1 m/s, the minimum inflow area of free water flow should be 1486.2 m^2. For an inlet velocity of 2 m/s, the minimum area of free water flow should be 418.8 m^2. And for an inlet velocity of 3 m/s, the minimum area of free water flow should be 243.2m^2

To confirm this, a CFD simulation of scaling factor 10 was carried out with an inflow area of the free water flow (block) of 250 m^2. The results are presented in Figure 5.27.
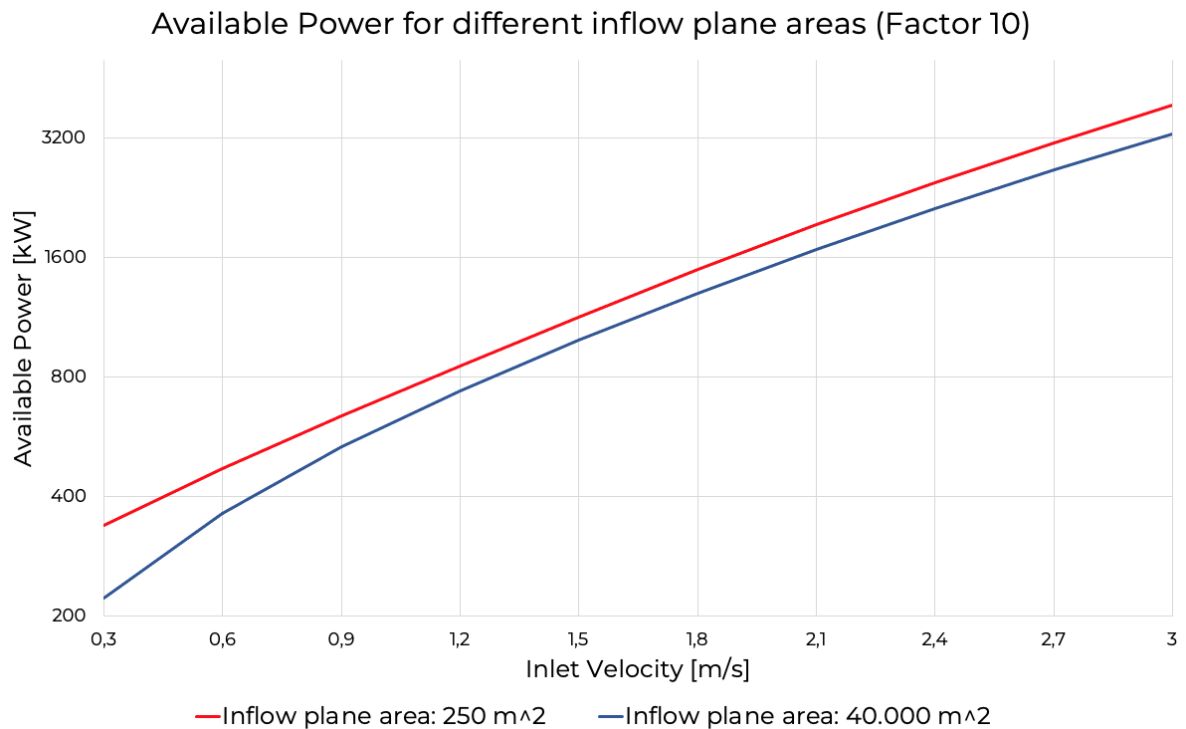
Figure 5.27: Available Power inside ducted system factor 10 for inflow area block of 250m^2 and 40.000 m^2 - logarithmic scale

The data of the simulations for the inlet area of 250 m^2 and 40,000 m^2 is summarised in Table 5.14 for an inlet velocity of 1 m/s, 2 m/s and 3 m/s

Table 5.14: Water flow power inside factor 10 ducted system with an inflow area of 250^2 and 40,000^2

Inflow Area	Water Flow Power [kW] at 1 m/s	Water Flow Power [kW] at 2 m/s	Water Flow Power [kW] at 3 m/s
250^2	814.2	1916.3	3935.5
40000^2	743.1	1675.1	3282.8

It is found that the simulation with a 250 m^2 inflow area of the block (free water flow) represents a higher available power inside the system. This would be correct if the hydrostatic pressure at the inflow plane would be equal to the total pressure as this indicates that the kinetic energy in the free flow is sufficient. However, it is found that the hydrostatic pressure does not equalise the total pressure at the inflow plane. In CFD simulations, this entails that extra energy was added in terms of pressure to overcome the minimal required amount of kinetic energy in the free water flow. Under real circumstances (ocean, river,...), the velocity would adapt instead of the magnitude of pressure. When the minimal required inflow area of the free water flow is not met, the flow velocity would decrease resulting in a lower amount of available power. For an inlet area of 40.000 m^2, the hydrostatic pressure and the total pressure are similar in the CFD simulations. This entails that the minimal required amount of kinetic energy in the free water flow was met.

Installing a hydrokinetic energy turbine with a ducted system in the free water flow will cause drag forces (Shives and Crawford, 2010b). This reduces the flow velocity of the free water flow. The paddlewheel in combination with the duct could influence or even block the entering flow. This affects the amount of kinetic energy to be captured by the paddlewheel.

To calculate the power performance output of the system, the available power needs to be multiplied by the power coefficient of the paddlewheel. The power coefficient C_P is dependent on the hydrodynamic efficiency. This power coefficient is uncertain as no field experiments are executed so far with the combination of the ducted system and the paddlewheel. Hence, future experiments need to be carried out to investigate the efficiency of the paddlewheel.

6

Discussion

In this chapter, the discussion regarding the field experiments, the CFD simulations and the CFD scaling are presented. The discussion consists of the considerations and the recommendations that should be taken into account for future research.

6.1. Field Experiments

The considerations and recommendations for future research concerning the field experiments are discussed in this section.

Firstly, the field experiments were carried out at a location with stagnant water. The running water was simulated by rotating the propellers of a workboat. This could have influenced the flow characteristics, such as flow direction, turbulence levels, turbulence structure (small scale vs. large scale), spatial uniformity (mean flow spatial gradients) and flow unsteadiness. The local bathymetry and nearby objects could also have affected the flow characteristics during the experiments. Therefore, it is recommended for future research to test the prototype in a laboratory facility, as they offer the advantages of controlled testing with a greater array of capabilities (instrumentation, sub-component testing, and improved methodology) (ITTC, 2014).

Secondly, the field experiments covered a velocity range between 0 m/s and 0.5 m/s. These are low flow velocities and higher flow velocities are more of interest. Therefore, a laboratory facility should be selected where higher velocities can be tested.

Thirdly, the flow velocity measurements during the field experiments are performed by point measurements. This can cause a distorted picture as the entire flow field has not been measured. The flow velocity near the wall is lower due to friction. Therefore, the measurements should be carried out with field velocity measurement equipment to map the entire velocity field. This will provide more accurate data.

Fourthly, the prototype was fixed to a workboat. This could involve minor movements of the prototype resulting in escaping air from the air chamber. This could affect the data as the air compressor works on an irregular basis. To minimise external factors, the prototype should be completely fixed in future experiments.

Fifthly, the waved and curved design ramps are only used at the inflow side. The outflow ramp was retained as a straight ramp. As improvements were found when changing the design of the inflow ramp, the performance should as well be measured when changing the design of the outflow ramp.

Lastly, the prototype was tested without a paddlewheel turbine installed. The paddlewheel turbine could affect the hydrodynamic behaviour inside the ducted system as the paddlewheel will extract the energy out of the water flow. To study the impact of a paddlewheel on the hydrodynamics, the paddlewheel should be installed in the prototype. The hydrodynamic efficiency of the paddlewheel should be investigated as well to determine the power coefficient. When this power coefficient is experimentally determined, the power performance output can be calculated.

6.2. CFD Simulations

The considerations and recommendations for future research concerning the CFD simulations are discussed in this section.

Firstly, when validating the CFD simulations with the field experiments, the data of both approaches represent a similar trend. For an increase in inlet velocity, an increase in velocity inside the ducted system is found. However, the error found is between 11.9% and 26.15%. This error could be minimised by calibrating the dimensionless constants. However, it was chosen not to adjust these parameters because it is unknown how to change these without extensive study during the experiments. Therefore, it was chosen to keep the input parameters that were found by Morse et al. (1972). When calibrating the parameters, the CFD simulations could be further optimised.

Secondly, for the CFD simulations, a one-phase approach was used. This entails that no air chamber was modelled in the ducted system and a steel plate was simulated instead of the air-water boundary between the air chamber and the water flow. The impact of the air chamber is therefore not included in the CFD simulations. The behaviour of the air chamber could have an impact on the magnitude of turbulence inside the system and thus on the data found. A two-phase approach should be used in future research to take into account the impact in hydrodynamics of the air chamber.

Thirdly, the time period for the simulations was set at 50 seconds. In 50 seconds, the inlet velocity increases linearly from 0 m/s to 3 m/s. The time period could have an influence on the data as the flow needs time to develop in the simulations. More simulations need to be carried out for larger time periods to study the relation between the time period and the acquired data about the hydrodynamics.

Lastly, similar as during the field experiments, the waved and curved design ramps are only used at the inflow side. The outflow ramp has been retained as a straight ramp. As improvements were found when changing the design of the inflow ramp, the performance should be measured when changing the outflow ramp design as well. This could have an influence on the flow velocity increase inside the ducted system.

6.3. CFD Scaling

The considerations and recommendations for future research concerning the CFD scaling are discussed in this section.

The considerations and the recommendations of the CFD scaling are similar to the CFD simulations, discussed in Section 6.2. However, during CFD scaling, the non-dimensional numbers are important. They all should be kept constant, however, it is not possible to keep them all the same. This implies that scaling introduces a source of error as some non-dimensional numbers must be changed. To avoid the error when scaling up the dimensions, larger prototypes need to be developed to test in the field.

7

Conclusions

The goal of this master thesis was to test a prototype of the ducted system of a hydrokinetic concept named the Van Rompay Turbine, by carrying out (i) field experiments to measure the hydrodynamics and subsequently (ii) to model the ducted system in CFD simulations to investigate the hydrodynamics for higher velocities and for scaled-up dimensions. The duct, which is based on a Venturi working principle, consists of a converging inlet, a throat and a diverging outlet. Above the throat, an air chamber is present to provide an air environment to reduce resistance for the paddlewheel.

7.1. Conclusions Field Experiments

The goal of the field experiments was to study the impact of the different geometries on the hydrodynamics in the ducted system. This is executed by studying the impact in flow velocity increase when changing the ramp sizes and ramp designs of the ducted system during field experiments (velocity range 0 m/s - 0.5 m/s). Three different inclination angles, 21°, 26° & 31°, for the converging inflow and diverging outflow segment are tested, referred to as the small, medium and large ramp size, respectively. Subsequently, on the best performing ramp in terms of the lowest energy losses, five different designs are tested, referred to as the straight, curved and high, mid & low frequency waved designs. This is done to find which configuration performs better in terms of the lowest energy losses in the system.

Despite the considerations stated in Chapter 6, the following conclusions of the field experiments are made:

- **The small ramp (inclination angle 21°) represents the highest flow velocity increase compared to the medium (inclination angle 26°) and large (inclination angle 31°) ramp.** Based on the continuity equation, it would be expected that the large ramp would represents the highest flow velocity increase as this ramp implies the smallest cross-sectional area inside the throat. However, the water flow for the medium (average flow velocity increase 55.7%) and large ramp (average flow velocity increase 42.3%) indicates too much blockage due to turbulence caused by a too steep converging ramp compared to the small ramp which has an average flow velocity increase of 80.9%.

- **The 21° inclination angle for the converging inflow segment represents the highest flow velocity increase for a rectangular shaped tube with a converging length of 1.2m compared to the medium (26°) and the large (31°) ramp.** Remarkably, this resembles the findings that for a conical-type Venturi tube, the optimal inclination angle is 21° and the length of the converging segment should be equal to $2.7(D-d)$ (Bird and Chivers, 1993). Despite the fact that it contains a different shape of a tube, these results indicate that the optimal inclination angle and converging length for a rectangular shaped tube may lay within the same range (±21°, 1.2m) as for a conical Venturi tube.

- **For inlet velocities between 0 m/s and 0.4 m/s, the high, mid & low frequency waved inflow ramp designs show a higher flow velocity increase compared to the straight and curved inflow ramp design.** Based on prior literature, the waved designs have the capability to cause drag reduction for lower flow velocities. This is caused due to the quasi-streamwise vortices which are moved away from the wall and weakened (Quadrio et al., 2009).

- **For inlet velocities between 0.4 m/s and 0.5 m/s, the curved inflow ramp design shows a higher flow velocity increase compared to the high, mid & low waved and the straight inflow ramp designs.** The pressure drop between the converging part and the throat inside the ducted system has a smooth and gradual transition in the curved ramp (Deutz, 2003).

The data acquired by the field experiments show uncertainty due to the scattering of the data points. External factors (e.g. movement of the prototype) may play a role in the accuracy of the data. The trend lines are plotted based on these data points. These are used to make conclusions about the different ramp sizes and designs. Hence, the trend lines may not be an accurate representation of the data, but rather an approximate representation. Besides this, the field experiments were tested over a low inlet velocity range (0-0.5 m/s), which limits the data analysis. Therefore, CFD simulations were carried out to acquire data with no influence of external factors and to investigate the system for higher velocities to improve the field experiments.

7.2. Conclusions CFD Simulations

The goal of this phase was to model the ducted system of the Van Rompay Turbine in the CFD simulations and to validate the acquired data with the field experiments. Subsequently, the impact in terms of turbulence kinetic energy and the impact in flow velocity increase when changing the inflow ramp designs of the ducted system was investigated for higher velocities (velocity range 0 m/s - 3 m/s). The five different inflow designs (straight, curved and high, mid & low frequency waved) are compared of the venturi configurations to find which configuration performs better in terms of the lowest energy losses in the system.

Despite the considerations stated in Chapter 6, the following conclusions of the CFD simulations are made:

- **For inlet velocities between 0 m/s and 0.75 m/s, the straight inflow ramp represents the lowest magnitude of turbulence kinetic energy compared to the curved and high, mid & low frequency waved inflow ramps.**

- **For inlet velocities between 0.75 m/s and 3 m/s, the curved inflow ramp represents the lowest magnitude of turbulence kinetic energy compared to the straight and high, mid & low frequency waved inflow ramps.**

- **For inlet velocities between 0 m/s and 0.75 m/s, the high, mid & low frequency waved inflow ramps show a higher flow velocity increase compared to the straight and curved inflow ramp design.** This is caused by quasi-streamwise vortices that are moved away from the wall and weakened. The weakened quasi-streamwise vortices produce fewer shear stresses which result in drag reduction (Tomiyama and Fukagata, 2013). Therefore, the high, mid & low frequency waved inflow designs have a positive impact on the flow velocity increase for lower velocities. For higher velocities, the drag reduction is less significant. This is due to the fact that for higher velocities the quasi-streamwise vortices get closer to the wall and consequently are less weakened (Tomiyama and Fukagata, 2013).

- **For inlet velocities between 0 m/s and 0.75 m/s, the high frequency waved inflow ramp (amplitude = 19mm) represents the highest flow velocity increase with an average of 55% compared to the mid and low frequency waved inflow ramp.** The low (amplitude = 90mm) and mid (amplitude = 50mm) frequency waved inflow ramp have an average flow velocity of 51% and 47%, respectively. Drag reduction appears to increase with the wave amplitude (Quadrio et al., 2009). However, the high frequency waved inflow ramp, which has the lowest amplitude, shows to have the highest average flow velocity increase (55%) compared to the mid and low frequency waved inflow ramps. This can be explained because the high frequency waved designs contains more wave periods. For more wave periods, more interaction is present and the turbulent flow is moved away from the wall region (Quadrio et al., 2009). Therefore, the high frequency waved inflow design has more impact on the turbulent reduction and higher flow velocities are found.

- **For inlet velocities between 0.75 m/s and 3 m/s, the curved inflow ramp represents the highest flow velocity increase compared to the straight and high, mid & low frequency waved inflow ramp.** The design of the curved ramp is a smooth and gradual transition to the throat. This smooth transition entails lower magnitudes of turbulence and causes therefore fewer losses.

7.3. Conclusions CFD Scaling

The goal of this phase was to investigate how the hydrodynamics of the ducted system of the Van Rompay Turbine are affected by scaling. The impact in terms of turbulence and the impact in flow velocity increase when scaling up the ducted system is studied by using the CFD model. Subsequently, the data of the CFD model is used to investigate the impact on the water flow power that is available to the paddlewheel when scaling up the dimensions. The ducted system (factor 1 - prototype) is scaled up with a factor 2 and a factor 10.

Despite the considerations stated in Chapter 6, the following conclusions of the CFD scaling are made:

- **When scaling up the ducted system with a factor 2 and 10, a lower magnitude of turbulence kinetic energy is present when averaging over the total volume.** For similar inlet velocities, the water flow entering the ducted system experiences less friction, as larger systems have a marginal lower specific surface of contact between the water and the duct. However, the total magnitude of turbulence kinetic energy present in the entire ducted system increases for larger systems.

- **Over an inlet velocity between 0 m/s and 3 m/s, factor 1 has the highest flow velocity increase with an average of 59.3% compared to the scaling factor 2 and factor 10.** The average flow velocity increase of the factor 2 and factor 10 ducted system is equal to 59.0% and 48.6%, respectively. The boundary layer in the converging part increases in thickness and in length when scaling up the dimensions. As the walls become longer, there is more interaction between the water flow and the wall. The particles in the layer closest to the wall encounter skin friction which causes more and larger vortices resulting in a longer and thicker boundary layer. This entails that more energy is lost in the water, which negatively impacts the flow velocity increase.

- **Scaling up the ducted system causes for an increase in total available power, however, the power per unit area decreases as more energy losses are present when scaling up.** Scaling up allows that more volumes can enter the ducted system and therefore, more power is present. This makes the duct of the Van Rompay turbine interesting as this can be scaled up depending on the site where the Van Rompay Turbine will be deployed. Nevertheless, when scaling up the ducted system, more energy losses (turbulence and friction) are found in the system.

- **The ducted system allows to collect energy in a small place, however, enough power should be available in the free water flow to provide enough force to overcome specific pressures in the ducted system.** When decreasing the inflow area of the block from 40,000 m^2 to 250 m^2, which represents the free water flow, the available power inside the ducted system (factor 10) is reduced. When the minimal required inflow area of the free water flow is not met, the flow velocity would decrease resulting in a lower amount of available power. Therefore, the power available inside the ducted system could change for various locations where the Van Rompay would be deployed.

7.4. Overall Conclusions

Despite the considerations stated in Chapter 6, the following overall conclusion are made:

The ducted system converges the flow to a smaller cross-sectional area in the throat. This results in the use of a smaller rotor to capture the same amount of energy, except for the energy losses (turbulence and friction) caused due to converging and diverging the water flow. The lowest energy losses for low-velocity currents between 0 m/s and 0.75 m/s is an in-and outflow inclination angle of 21° with a high frequency waved inflow ramp design. Regarding higher velocity currents between 0.75 m/s and 3 m/s, an in-and outflow inclination angle of 21° with a curved inflow ramp represents the lowest energy losses. For scaled up systems, more losses are found as more turbulence and friction is present, however scaling up allows for more volume entering the system, increasing the available water flow power. The extent to which the ducted system can be scaled up depends on the space restrictions at the specific location. Besides, the minimal required inflow area of the free water flow should be met. It can therefore be concluded that the potential available energy for generation also depends the location where the Van Rompay will be deployed. Bearing the recommendations in mind, more experiments need to be conducted in the future to investigate the potential of this concept in more detail by determining its power performance output.

Bibliography

Akinyemi, O., & Liu, Y. (2015). Cfd modeling and simulation of a hydropower system in generating clean electricity from water flow. *International Journal of Energy and Environmental Engineering, 6.* https://doi.org/10.1007/s40095-015-0180-2

Aqua libre performance. (n.d.). https://www.aqualibre-finanz.at/leistungsvermogen/?lang=en

ASEAN. (n.d.). The rising wave of tidal energy in southeast asia. https://theaseanpost.com/article/rising-wave-tidal-energy-southeast-asia

Askari, M., Mirzaei Mahmoud Abadi, V., Mirhabibi, M., & Dehghani, P. (2015). Hydroelectric energy advantages and disadvantages. *American Journal of Energy Science, 2,* 17–20.

Bird, J. O., & Chivers, P. J. (Eds.). (1993). Newnes pocket books. In *Newnes engineering and physical science pocket book* (pp. 554–555). Newnes. https://doi.org/https://doi.org/10.1016/B978-0-7506-1683-6.50072-2

Blodgett, C., Dauenhauer, P., Louie, H., & Kickham, L. (2017). Accuracy of energy-use surveys in predicting rural mini-grid user consumption. *Energy for Sustainable Development, 41,* 88–105. https://doi.org/10.1016/j.esd.2017.08.002

BP, C. (2020). Statistical review of world energy 2020. https://www.bp.com/content/dam/bp/business-sites/en/global/corporate/pdfs/energy-economics/statistical-review/bp-stats-review-2020-full-report.pdf?utm_source=BP_Global_GroupCommunications_UK_external&utm_medium=email&utm_campaign=11599394_Statistical%5C%20Review%5C%202020%5C%20-%5C%20on%5C%20the%5C%20day%5C%20reminder&dm_i=1PGC%5C%%5C2C6WM5E%5C%2COV0LQ4%5C%2CRQW75%5C%2C1

Broslawski, C., DeGiacomo, F., Goddard, K., & C., P. (2017). Towards the optimization of a fin-based hydropower generator. https://web.wpi.edu/Pubs/E-project/Available/E-project-032217-144047/unrestricted/Towards_the_Optimization_of_a_Fin-Based_Hydropower_Generator.pdf

Bryden, I. (2016). Tidal energy. *Reference module in earth systems and environmental sciences.* Elsevier. https://doi.org/https://doi.org/10.1016/B978-0-12-409548-9.10261-1

Commission, E. (2020). An eu strategy to harness the potential of offshore renewable energy for a climate neutral future.

Decentralized electrification. (n.d.). https://www.smart-hydro.de/

Designpro technology. (n.d.). https://designprorenewables.com/technology/#how_it_works

Deutz, L. (2003). *Study of the properties of turbulent flow through a venturi using lda techniques.*

Develops and supplies turn-key tidal power arrays. (n.d.). http://www.andritzhydrohammerfest.co.uk/

Emec. (2020). www.emec.org.uk/marine-energy/tidal-devices

Flambard, J., Amirat, Y., Feld, G., Benbouzid, M., & Ruiz, N. (2019). River and estuary current power overview. *Journal of Marine Science and Engineering, 7.* https://doi.org/10.3390/jmse7100365

Francis, W., & Peters, M. C. (1980). Data sheet no. 134 - solar power. In W. Francis & M. C. Peters (Eds.), *Fuels and fuel technology (second edition)* (Second Edition, pp. 459–461). Pergamon. https://doi.org/https://doi.org/10.1016/B978-0-08-025249-0.50084-7

Gkinetic technology. (2017). https://gkinetic.com/technology/

A global sustainable energy company. (2020). https://simecatlantis.com/

Guimarães, L. N. d. M. R. (2021). Alternative energy: Sources and future trends. In W. Leal Filho, A. Marisa Azul, L. Brandli, A. Lange Salvia, & T. Wall (Eds.), *Affordable and clean energy* (pp. 40–50). Springer International Publishing. https://doi.org/10.1007/978-3-319-95864-4_1

Hamed, A. M., Kamdar, A., Castillo, L., & Chamorro, L. P. (2015). Turbulent boundary layer over 2d and 3d large-scale wavy walls. *Physics of Fluids, 27*(10), 106601. https://doi.org/10.1063/1.4933098

Hydro Quebec. (2015). A renewable energy option: hydrokinetic power.

Hydrokinetic river and tidal turbine guinard energies. (2020). https://www.guinard-energies.bzh/en/guinard-energies-2/

Hydroquest technologies. (n.d.). https://www.hydroquest.net/technologies/

Hydrotube energie gets free power from tidal turbine. (2017). https://www.offshore-energy.biz/hydrotube-energie-gets-free-power-from-tidal-turbine

Idenergy performance. (n.d.). http://idenergie.ca/en/features/

IEA. (2020a). Access to electricity in the sustainable development scenario [Retrieved from https://www.iea.org/data-and-statistics/charts/access-to-electricity-in-the-sustainable-development-scenario-2010-2030 on 09/11/2020].

IEA. (2020b). International energy outlook. https://www.eia.gov/outlooks/ieo/pdf/ieo2020.pdf

IEA. (2020c). Sdg7: Data and projections. https://www.iea.org/reports/sdg7-data-and-projections

IEA. (2019). Global Energy & CO2 Status Report.

Im, H., Hwang, T., & Bumsuk, K. (2020). Duct and blade design for small-scale floating tidal current turbine development and cfd-based analysis of power performance. *Journal of Mechanical Science and Technology, 34*, 1591–1602. https://doi.org/10.1007/s12206-020-0321-2

IRENA. (2020). Innovation outlook ocean energy technologies.

ITTC. (2014). Model tests for current turbines.

J. Robbins. (2019). On the Water-Starved Colorado River, Drought Is the New Normal.

Jung, S.-H., Seo, I.-H., & Kim, C.-H. (2011). Effect of venturi system on acceleration of low-speed water flow at the venturi throat installed at the inlet of hydro turbine. *Journal of the Korean Society of Marine Engineering, 35.* https://doi.org/10.5916/jkosme.2011.35.7.914

Kallis, G., & Butler, D. (2001). The eu water framework directive: Measures and implications. *Water Policy, 3*(2), 125–142. https://doi.org/https://doi.org/10.1016/S1366-7017(01)00007-1

Kenyon, H. D. (2017). Harvesting Hydrokinetic River Current Power.

Khan, M., Iqbal, M., & Quaicoe, J. (2008). River current energy conversion systems: Progress, prospects and challenges. *Renewable and Sustainable Energy Reviews, 12*(8), 2177–2193. https://doi.org/https://doi.org/10.1016/j.rser.2007.04.016

Khunthongjan, P., & Janyalertadun, A. (2012). A study of diffuser angle effect on ducted water current turbine performance using cfd. *Songklanakarin Journal of Science and Technology, 34.*

Kirke, B. (2003). Developments in ducted water current turbines (this paper was originally written in 2003 and published on www.cyberiad.net. this version includes some updates on tests conducted in 2005).

Laghari, J., Mokhlis, H., Bakar, A., & Mohammad, H. (2013). A comprehensive overview of new designs in the hydraulic, electrical equipments and controllers of mini hydro power plants making it cost effective technology. *Renewable and Sustainable Energy Reviews, 20*, 279–293. https://doi.org/https://doi.org/10.1016/j.rser.2012.12.002

Laws, N. D., & Epps, B. P. (2016). Hydrokinetic energy conversion: Technology, research, and outlook. *Renewable and Sustainable Energy Reviews, 57*, 1245–1259. https://doi.org/https://doi.org/10.1016/j.rser.2015.12.189

Li, D., Yao, Y., Chen, Q., & Ye, Z. (2015). Numerical simulation of tidal current energy in yangtze estuary-hangzhou bay, china, 1–6. https://doi.org/10.1109/OCEANS-Genova.2015.7271385

Mankins, J. (1995). Technology readiness level – a white paper.

MeyGen. (n.d.).

Morse, A., Launder, B., Spalding, D., & Rodi, W. (1972). Prediction of free shear flows: A comparison of the performance of six turbulence models.

Muller, G., Denchfield, S., & Shelmerdine, R. (2007). Stream wheels for applications in shallow and deep water.

Murray, R. E., Ordonez-Sanchez, S., Porter, K. E., Doman, D. A., Pegg, M. J., & Johnstone, C. M. (2018). Towing tank testing of passively adaptive composite tidal turbine blades and comparison to design tool [Retrieved from http://www.sciencedirect.com/science/article/pii/S0960148117309254 on 10/11/2020]. *Renewable Energy, 116*, 202–214. https://doi.org/https://doi.org/10.1016/j.renene.2017.09.062

Ocean renewable power company. (n.d.). https://www.orpc.co/

OTT. (n.d.). http://meteo-tech.co.it/ImagesDownloadFiles/c31.pdf

P. Castro, M. H. (2007). *Marine biology.* McGraw-Hill Higher Education.

Paish, O. (2002). Small hydro power: Technology and current status. *Renewable and Sustainable Energy Reviews, 6*(6), 537–556. https://doi.org/https://doi.org/10.1016/S1364-0321(02)00006-0

Patil, B., devojee, B., Hj, P., & Pasha, M. (2020). Advances in renewable energy technologies.

Quadrio, M., RICCO, P., & VIOTTI, C. (2009). Streamwise-travelling waves of spanwise wall velocity for turbulent drag reduction. *Journal of Fluid Mechanics, 627*, 161–178. https://doi.org/10.1017/S0022112009006077

Quaranta, E., & Revelli, R. (2018). Gravity water wheels as a micro hydropower energy source: A review based on historic data, design methods, efficiencies and modern optimizations. *Renewable and Sustainable Energy Reviews, 97*, 414–427. https://doi.org/https://doi.org/10.1016/j.rser.2018.08.033

Radkey, R. L., & Hibbs, B. D. (1981). Definition of cost-effective river-turbine designs. final report, september 30, 1980-december 31, 1981.

Researching environmental monitoring technologies for marine energy. (n.d.). https://triton.pnnl.gov/

Ritchie, H. (2014). Energy [https://ourworldindata.org/energy]. *Our World in Data.*

Rosen, M. (2012). *A synthesis of aquatic science for management of lakes mead and mohave.*

Rosli, R., & Dimla, E. (2018). A review of tidal current energy resource assessment: Current status and trend, 34–40. https://doi.org/10.1109/ICREGA.2018.8337585

Saidur, R., Rahim, N., Islam, M., & Solangi, K. (2011). Environmental impact of wind energy. *Renewable and Sustainable Energy Reviews*, *15*(5), 2423–2430. https://doi.org/https://doi.org/10.1016/j.rser.2011.02.024

Shives, M., & Crawford, C. (2010a). Overall efficiency of ducted tidal current turbines. *MTS/IEEE Seattle, OCEANS 2010*, 1–6. https://doi.org/10.1109/OCEANS.2010.5664426

Shives, M., & Crawford, C. (2010b). Overall efficiency of ducted tidal current turbines. *MTS/IEEE Seattle, OCEANS 2010*, 1–6. https://doi.org/10.1109/OCEANS.2010.5664426

Tevata, A., & Inprasit, C. (2011). The effect of paddle number and immersed radius ratio on water wheel performance. *Energy Procedia*, *9*, 359–365. https://doi.org/10.1016/j.egypro.2011.09.039

Tidal energy: The energy of the future. (n.d.). http://www.eel-energy.fr/

Tidal power complete deployment of advanced modular anchoring system. (n.d.). https://orbitalmarine.com/news/89-scotrenewables-tidal-power-ltd-srtp-complete-deployment-of-advanced-modular-anchoring-system

Tidal power complete deployment of advanced modular anchoring system. (n.d.). https://orbitalmarine.com/news/89-scotrenewables-tidal-power-ltd-srtp-complete-deployment-of-advanced-modular-anchoring-system

Tomiyama, N., & Fukagata, K. (2013). Direct numerical simulation of drag reduction in a turbulent channel flow using spanwise traveling wave-like wall deformation. *Physics of Fluids*, *25*(10), 105115. https://doi.org/10.1063/1.4826887

Tsp: A clean and predictable solution, driving force of the energy transition. (n.d.). https://www.sabella.bzh/

Turbines and engineering services. (2018). https://simecatlantis.com/services/

UCS. (2008). Environmental impacts of renewable energy technologies. https://www.ucsusa.org/resources/environmental-impacts-renewable-energy-technologies#:~:text=All%5C%20energy%5C%20sources%5C%20have%5C%20some,use%5C%2C%5C%20and%5C%20global%5C%20warming%5C%20emissions.

US Bureau of Reclamation. (2020). Lake Mead Water Database.

Van Rompay, B. G. (2012). *Surface treated composites white book*. Tahoka Press.

Van Rompay, B. G. (2004). US6692336B2 Method for protecting underwater surfaces against pollution due to fouling, and brush and coating agent used therewith.

Van Rompay, B. G. (2010). Recuperation system for underwater cleaning operations. https://uspto.report/patent/app/20120006244

Van Rompay, B. G. (2017). Device for generating hydro-electric energy. https://www.freepatentsonline.com/y2017/0167469.html

Westwood, A. (2004). Ocean power: Wave and tidal energy review. *Refocus*, *5*(5), 50–55. https://doi.org/https://doi.org/10.1016/S1471-0846(04)00226-4

What causes ocean tides? (n.d.). https://www.timeanddate.com/astronomy/moon/tides.html

Widén, J., Carpman, N., Castellucci, V., Lingfors, D., Olauson, J., Remouit, F., Bergkvist, M., Grabbe, M., & Waters, R. (2015). Variability assessment and forecasting of renewables: A review for solar, wind, wave and tidal resources. *Renewable and Sustainable Energy Reviews*, *44*, 356–375. https://doi.org/https://doi.org/10.1016/j.rser.2014.12.019

Williams, G. E. (2005). Comment on "tidal rhythmites and their implications" by r. mazumder and m. arima [earth-science reviews, 69 (2005) 79–95]. *Earth-Science Reviews*, *72*(1), 113–117. https://doi.org/https://doi.org/10.1016/j.earscirev.2005.05.001

Zainol, M., Ismail, N., & Zainol, I. (2017). A review on the status of tidal energy technology worldwide. *Science International*, *29*, 675–680.

Zerpa, L., Partington, B., & Gamboa, J. (2019). Effect of nozzle geometry on critical-subcritical flow transitions. *Heliyon*, *5*, e01273. https://doi.org/10.1016/j.heliyon.2019.e01273

Zheng, J., Dai, P., & Zhang, J. (2015). Tidal stream energy in china [8th International Conference on Asian and Pacific Coasts (APAC 2015)]. *Procedia Engineering, 116,* 880–887. https://doi.org/https://doi.org/10.1016/j.proeng.2015.08.377

Zohuri, B. (2020). 2 - nuclear fuel cycle and decommissioning. In S. U.-D. Khan & A. Nakhabov (Eds.), *Nuclear reactor technology development and utilization* (pp. 61–120). Woodhead Publishing. https://doi.org/https://doi.org/10.1016/B978-0-12-818483-7.00002-0

A
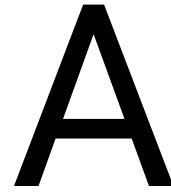
Device Development Stages

Technology Readiness Levels (TRL) are used to give an overview of the stages that need to be done to develop a new technology towards the full economic operation. A summary is given below and is found in the paper of Mankins (1995):

- TRL 1 Basic principles observed and reported

- TRL 2 Technology concept and/or application formulated

- TRL 3 Analytical and experimental critical function and/or characteristic proof-of-concept

- TRL 4 Component and/or breadboard validation in a laboratory environment

- TRL 5 Component and/or breadboard validation in a relevant environment

- TRL 6 System/subsystem model or prototype demonstration in a relevant environment

- TRL 7 System prototype demonstration in a space environment

- TRL 8 Actual system completed and "flight qualified" through test and demonstration (ground or space)

- TRL 9 Actual system "flight-proven" through successful mission operations

B

Tidal and River Current Energy Explained

B.0.1. Principle of Tidal Stream Energy

Tidal flows are formed by the gravitational and centrifugal forces originating from the interaction between the sun, moon and earth (Zheng et al., 2015). The gravitational force creates two bugles on opposite sides and can be accurately predicted. This can be seen in Figure B.1. The centrifugal force is generated by the rotation of the moon and the earth (Williams, 2005). This combination of forces creates tidal phenomena around the world. Depending on the location, a maximum of two tides can be present (Westwood, 2004).
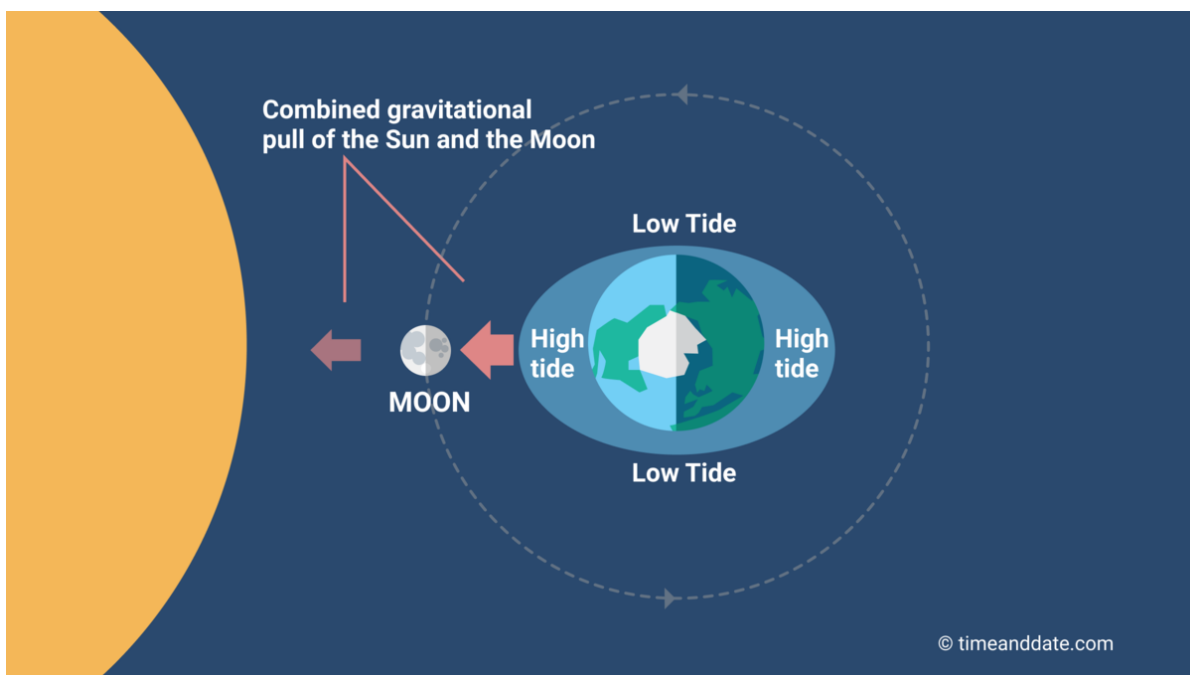
Figure B.1: The ocean bugle (not in scale) (*What Causes Ocean Tides?* n.d.)

The position of the moon and the sun can affect the tidal displacement as shown in Figure B.2. Over a period of time, one can predict the changes in the tides.
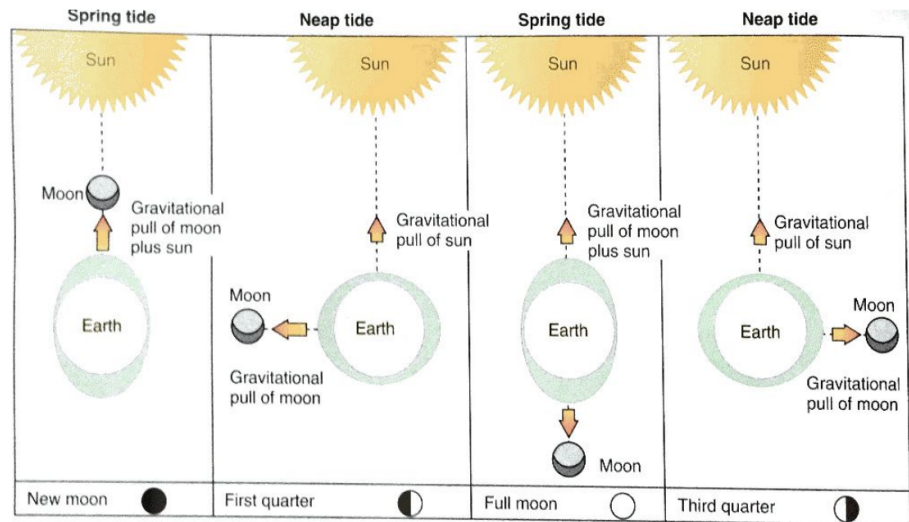
Figure B.2: Sun and moon effects on tide (P. Castro, 2007)

Tidal energy can be divided into two categories: the potential and the kinetic energy. The potential energy could be captured by the so-called tidal barrage approach. The kinetic energy, or tidal stream, could be captured by the tidal current turbines approach. In Figure B.3, the two methods for generating electricity from the tides are shown (ASEAN, n.d.).
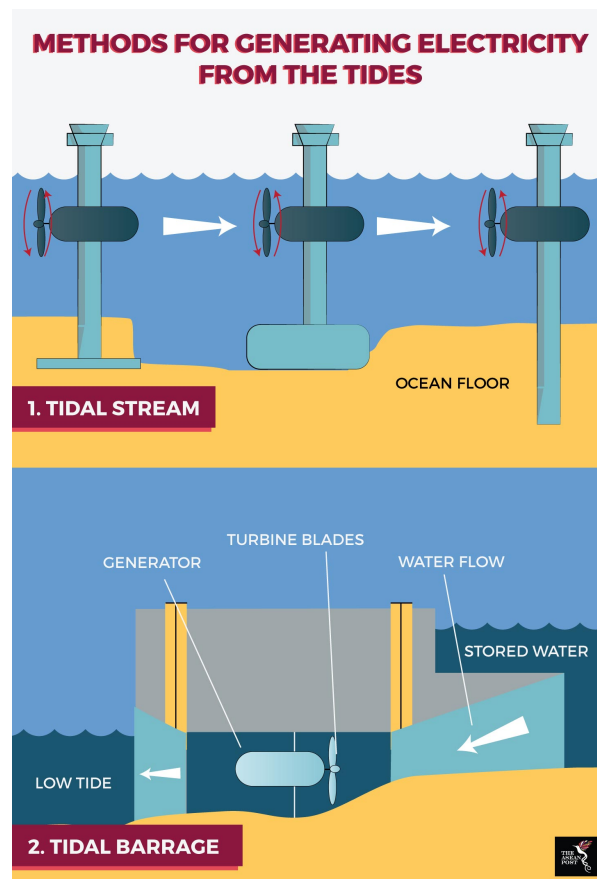
Figure B.3: Methods for generating electricity from the tides (ASEAN, n.d.)

B.0.2. Principle of River Current Energy

Rivers are a constant flowing part of the hydrologic cycle, which makes them ideal for a renewable energy resource (Broslawski et al., 2017). River current energy systems are electromechanical energy converters that convert the kinetic energy of the river flow into energy. Based on the definition of Radkey and Hibbs (1981), river current turbines are 'Low-pressure run-of-the-river ultra-low-head turbines that will operate on the equivalent of less than 0.2m of head'.

The conventional way of generating energy is by building hydropower plants. This principle can be seen in figure B.4 These plants make use of reservoirs and penstocks to create an artificial water head. The created potential energy will be converted into electric power by turbines. This is in contrast with the definition of Radkey and Hibbs (1981) about river current turbines. These could be built as a free-rotor or part of a channel augmented system and require less or no civil work (Khan et al., 2008). Besides, the environmental impact will be drastically less compared to the conventional hydropower plants.
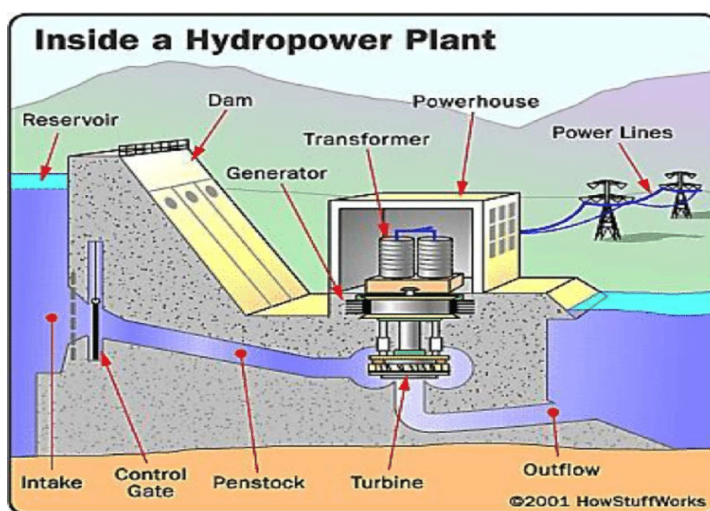
Figure B.4: The inside of a conventional hydropower plant (Patil et al., 2020)

C

Different tidal energy technologies

In Figure C.1, the different tidal energy technologies are shown (*EMEC* 2020). The tidal barrage is based on head difference and the other technologies are based on tidal currents.

TRL 9

Barrage
Water that entered an enclosed tidal basin with high tide is released in low tide and generates electricity by passing through turbines.

TRL 8

Horizontal-axis turbine
The tidal currents flow past blades that are radially attached to a horizontal shaft and cause rotation, thus generating power, much like a wind turbine underwater. Either the hub or blades need to turn 180 degrees to accommodate a reverse flow direction.

TRL 5

Vertical-axis turbine
The tidal currents flow through a set of blades parallel to a rotating shaft, generating power irrespective of the direction of the flow.

TRL 7

Enclosed tips (venturi)/open-centre
The tidal stream's velocity is increased by concentrating it in a funnel or duct, in which a turbine is placed to generate energy.

TRL 5

Reciprocating device/oscillating hydrofoil
the tidal flow lifts an oscillating hydrofoil attached to an arm. This up-and-down movement drives a shaft or pistons to generate energy.

TRL 6

Archimedes screw/spiral
a tidal stream passes through the spiral of a helical-shaped impeller. The device starts to turn, and the rotation is converted into energy.

TRL 6

Tidal kite
A kite connected to the sea bed or to a floating platform moves through the tidal stream in an eight-shaped or linear trajectory. The relative velocity is increased and with it the electricity output.

Other
Other technologies have been investigated that either fit in none of the categories or incorporate various aforementioned characteristics.

Figure C.1: Different tidal energy turbine technologies (*EMEC* 2020)

D

Sources Active Hydrokinetic Concepts

In Table D.1, an overview of the sources used to make a summary of the active hydrokinetic turbines based on river and tidal currents are shown.

Table D.1: Overview of sources used to make a summary of the active hydrokinetic energy turbines.

Source	System
Tidal Power complete deployment of advanced modular anchoring system (n.d.)	Tidal
Develops and supplies turn-key tidal power arrays (n.d.)	Tidal
Turbines and Engineering Services (2018)	Tidal
A global sustainable energy company (2020)	Tidal
Tidal Power complete deployment of advanced modular anchoring system (n.d.)	Tidal
TSP: a clean and predictable solution, driving force of the energy transition (n.d.)	Tidal
Researching Environmental Monitoring Technologies For Marine Energy (n.d.)	Tidal
Decentralized Electrification (n.d.)	River
DesignPro Technology (n.d.)	River
Aqua Libre Performance (n.d.)	River
Gkinetic Technology (2017)	River
Hydrokinetic river and tidal turbine Guinard Energies (2020)	River
Ocean Renewable Power Company (n.d.)	River
Tidal energy: The energy of the future (n.d.)	River
Idenergy performance (n.d.)	River
Hydrotube Energie gets free power from tidal turbine (2017)	River
HydroQuest Technologies (n.d.)	River

E

Venturi Principle Explained

A well designed Venturi ducted system can channel and accelerate a flow. This accelerated flow creates more force on the turbine blades and therefore, the power output can be enlarged. This principle is also used in conventional hydropower turbines (ITTC, 2014). However, Venturi ducted systems cause an increase in drag compared to an open turbine device.

For the Venturi ducted system, the theoretical limit depends on:

- The pressure difference that is caused by narrowing the inflow segment

- The volumetric flow through the Venturi ducted system

- The design and the dimensions of the Venturi ducted system

E.0.1. Converging and Diverging flow

In converging flow, the area will decrease and therefore the velocity will increase along with the flow and thus an acceleration can be found. This velocity increase means that the pressure will drop. This can be seen in Figure E.1.
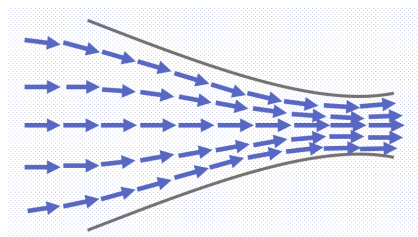
Figure E.1: Converging flow - Own work

For diverging flow, the case will be exactly the opposite. The pressure will increase along with the flow. This pressure increase is called an adverse pressure gradient condition. As the pressure increases along with the flow, the fluid particles decelerate along the length. After a particular length, flow reversal could occur. This reversal will lead to flow vortices and energy losses. In short, diverging flow is a difficult flow to maintain. It offers far more resistance than the converging flow. This can be seen inFigure E.2.
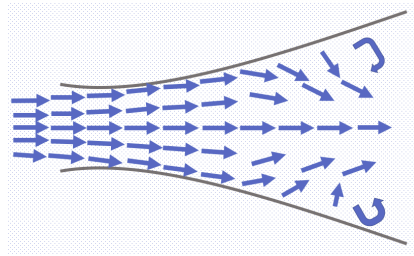
Figure E.2: Diverging flow - Own work

E.0.2. Theoretical background

Venturi ducted systems are based on Bernoulli's equation, see Equation E.1. This equation describes the conservation of energy for flowing fluids. In the places where the flow velocity is increased, a decrease in fluid pressure can be found. The equation that is used to calculate the flow velocity in a perfectly designed Venturi ducted system can be found in Equation E.1. Note that friction losses are not taken into account and should be considered to get reliable results.

$$P_1 + \frac{1}{2}\rho v_1^2 + \rho g h_1 = P_2 + \frac{1}{2}\rho v_2^2 + \rho g h_2 \tag{E.1}$$

The first term is the pressure energy, the second term is the kinetic energy per unit volume and the third term is the potential energy per unit volume. This can be found in the figure E.3
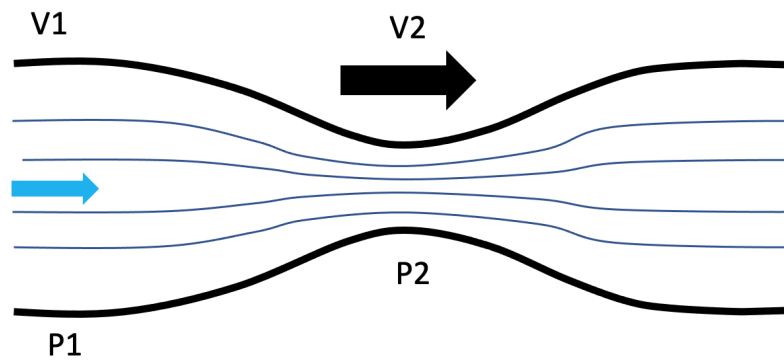
Figure E.3: Bernoulli Equation - Own work

The fluid speed is increased for V_2 and the internal pressure is decreased for P_2 due to the decrease in area ($A_2 < A_1$).

Air Chamber Explained

In the concept, the air chamber is located in the middle of the device. To give a good impression, the device is shown in Figure F.1.
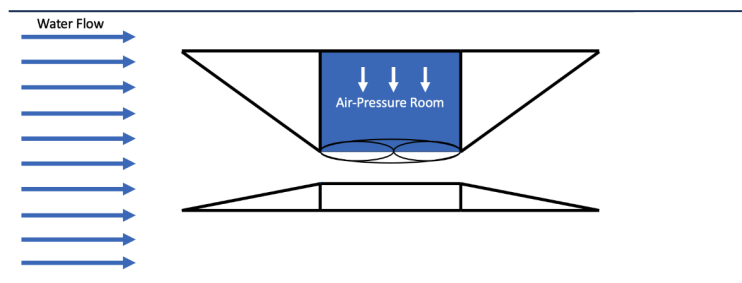
Figure F.1: Side view air chamber - Own work

The pressure inside is initially p_{Atm} = 1 atm. The pressure outside (water pressure) can be computed from the hydrostatic equations shown below. Note that the unit is in Pascal [Pa].

$$P_{atm} = 101325 \;\; Pa = 1 \;\; atm \tag{F.1}$$

$$P_{Height} = \rho \times g \times \Delta h \tag{F.2}$$

$$P_{Speed} = \frac{1}{2} \times \rho \times v^2 \tag{F.3}$$

$$P_{Total} = P_{atm} + P_{Height} + P_{Speed} \tag{F.4}$$

The pressures can be found in Figure F.2.
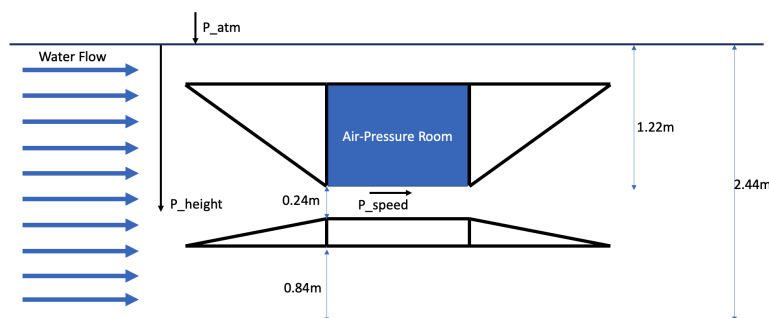
Figure F.2: Pressure overview - Own Work

Let's assume that the air inside can be approximated by an ideal gas; we will then have:

$$P_{in} = \frac{nRT}{V} \qquad\qquad (F.5)$$

Where V is the volume of air inside the air chamber, the mechanical equilibrium requires that:

$$P_{out} = P_{in} \qquad\qquad (F.6)$$

From which we obtain:

$$V(z) = \frac{nRT}{P_{atm} + \rho g z} \qquad\qquad (F.7)$$

The initial volume is:

$$V^* = \frac{nRT}{P_{atm}} \qquad\qquad (F.8)$$

From which:

$$V(z) = V^* \cdot \left(1 + \frac{\rho g z}{P_{atm}}\right)^{-1} \qquad\qquad (F.9)$$

This equation tells us how the volume of air inside the chamber decreases with depth. For water, we have $\rho = 10^3$ kg/m^3 and this value can be considered independent from z since water is almost incompressible. Atmospheric pressure is $P_{atm} = 10^5$ Pa. We round up g to 10 m/s^2. Therefore we obtain:

$$V(z) \simeq V^* \cdot \left(1 + \frac{z}{10\text{m}}\right)^{-1} \qquad\qquad (F.10)$$

The air chamber must be pressurized to prevent water inside. By creating an air chamber, the water will be held out because of the air pressure inside the lock. This air pressure should be sufficient to create a boundary between the water flow and the air chamber.

G

Drawings Prototypes

G.1. Drawings Prototype

In Figure G.1, the drawing of the side view of the Van Rompay Turbine prototype is presented. In Figure G.2, the 3D drawing for the prototype can be found.
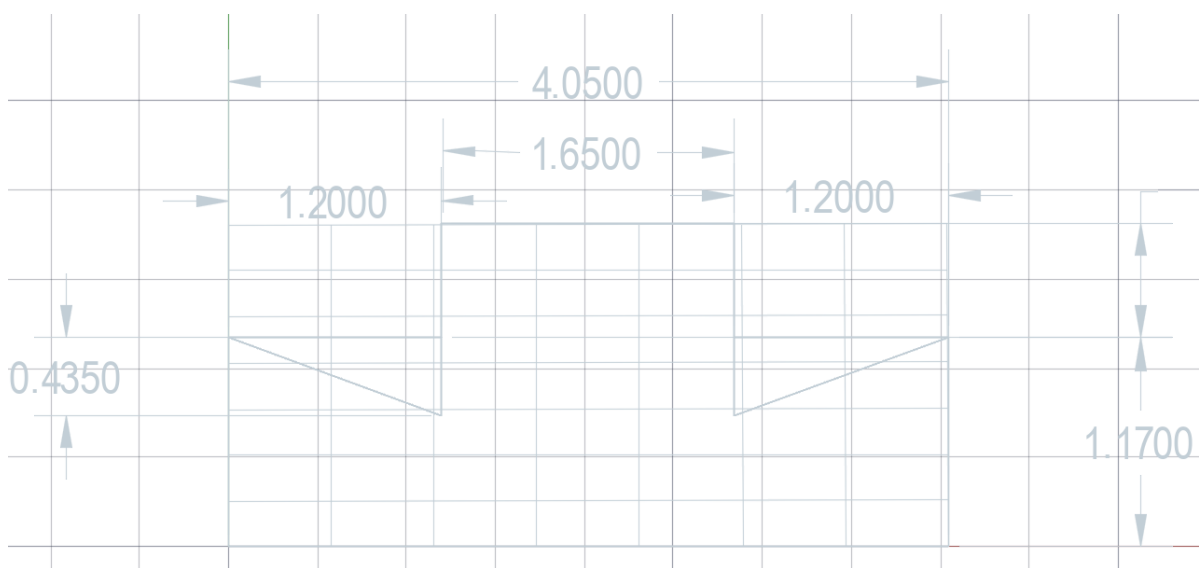
Figure G.1: Side view drawing prototype
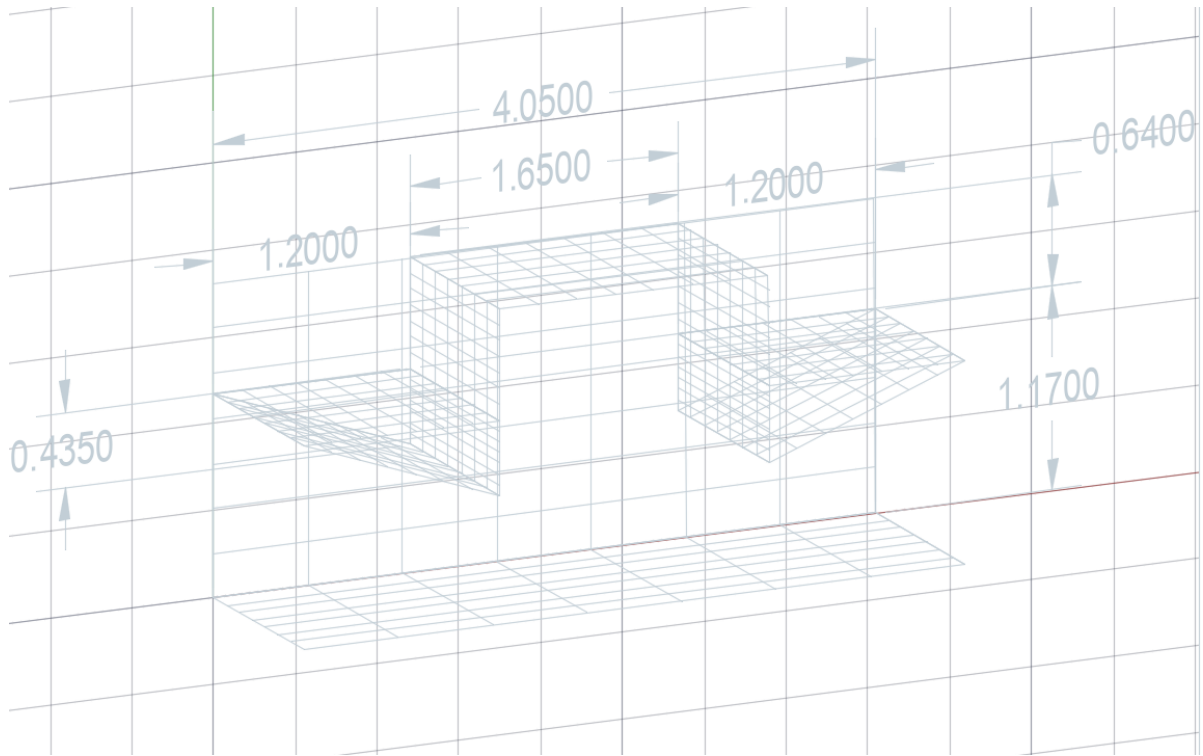
Figure G.2: SE Isometric drawing prototype

H
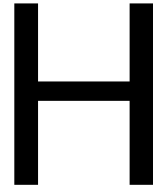
Specs C31 Universal Current Meters

In Figure H.1, a drawing of a C31 Universal Current Meter is shown. In Figure H.2, an image of a current meter on a rod of 20 mm diameter is shown. And in Figure H.3, the functioning is explained and the measuring range is given. This is necessary to gain and process data into reliable results.
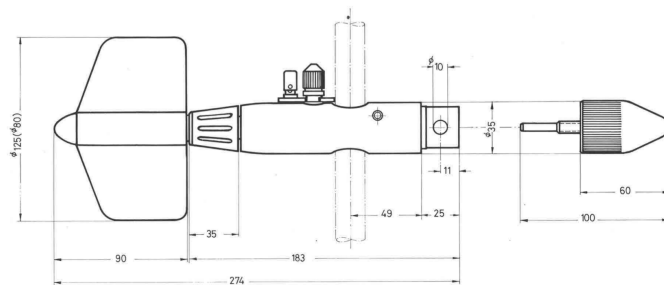
Figure H.1: Dimensional Drawing (OTT, n.d.)
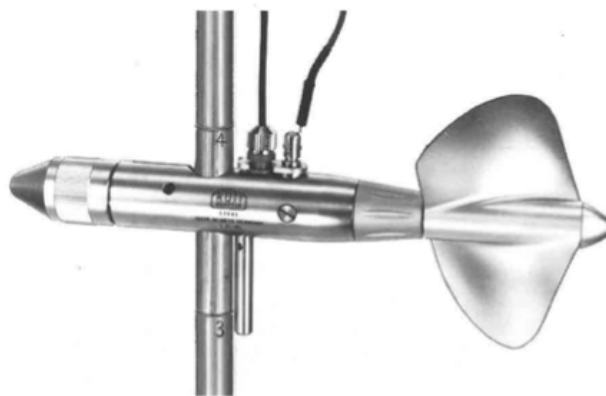
Figure H.2: C31 Current meter on rod of 20 mm diameter (OTT, n.d.)

Functioning

The meter propeller gets turned by the flow. A magnet turning with the propeller actuates, once per revolution, the built-in Reed contact which is watertight under pressure. The pulse sequence is nearly proportional to the water velocity in the measuring point.

The exact relation between the number of propeller revolutions per second and the water velocity is determined by the equation

$$v = k \cdot n + \Delta.$$

n = propeller revolution per second

k = hydraulic pitch (m), determined by test runs in the rating tank

Δ = meter constant (m/sec), determined by test runs in the rating tank.

Since among current meters there are mechanical differences in the propellers as well as in the bearings, the constants k and Δ are found by specific tests in our rating tank (certificate of calibration BARGO).

If desired, the calibration equation (relation between n and v) can also be supplied with fully calculated values and compiled in a table (velocity table BAREL).

For more particulars regarding the calibration of current meters, see folder HLe 120/14.

If the requirements of accuracy are not so high it is also possible to supply an average equation for the plastic propellers, which is established on the base of several individual calibration equations.

Measuring Range

Depending on the pitch of the propeller chosen, the current meter can be used for different velocity measuring-ranges.

In case of oblique water currents it is possible to measure the component of the flow within an angular range which depends on the type of propeller (see table).

Propeller number engraved	Propeller size	Maximum water velocity * (m/sec)	Starting speed (m/sec)	Range of component effect	Material
1	125 mm dia., 0.25 m pitch	5.0	0.025	5°	Brass
1	125 mm dia., 0.25 m pitch	5.0	0.035	5°	Plastic
2	125 mm dia., 0.50 m pitch	6.0	0.040	5°	Brass
2	125 mm dia., 0.50 m pitch	6.0	0.060	5°	Plastic
3	125 mm dia., 1.00 m pitch	10.0	0.055	5°	Brass
4	80 mm dia., 0.125 m pitch	3.0	0.040	5°	Brass
A	100 mm dia., 0.125 m pitch	2.5	0.030	45°	Brass
R	100 mm dia., 0.25 m pitch	5.0	0.035	15°	Aluminium

* This maximum velocity can only be measured by means of the Z 215 counter set which has a counting rate of up to 20 revolutions per second.

Figure H.3: Functioning and Measuring range (OTT, n.d.)

Accuracy Ramp Design Simulations

I.1. Mesh

A mesh covers a given shape or form, and subdivides it into non-overlapping elements. Functions are assigned to the specific elements. These functions can be calculated for the entire model by assembling the collection of all elements. The block represents the free water flow and the inner geometry represents the ducted system of the "Van Rompay Turbine".

I.1.1. Mesh Size

The mesh sizes are kept the same overall the simulations of the designs. The ducted system's mesh size is selected as fine, whereas the block mesh size is selected as normal. The difference in mesh size is due to the fact that hydrodynamic behaviour close to and inside the Van Rompay Turbine is more of interest and therefore it should be calculated with more accuracy.

I.1.2. Mesh Elements

In Figures I.1a, I.1b, I.1c, I.1d and I.1e, the information about the elements is presented. The minimum element quality is ±0.2225, ±0.1952 and ±0.0.1851 for the factor 1, factor 2 and factor 10 simulations respectively. This is sufficient as the rule of thumb says that a minimum element quality of at least 0.1 is necessary. For the waved designs, the minimum element quality is lower because more the design has more detailed and smaller curvatures.

(a) Straight ramp

(b) Curved ramp

(c) High Frequency Waved ramp

(d) Mid Frequency Waved ramp

(e) Low Frequency Waved ramp
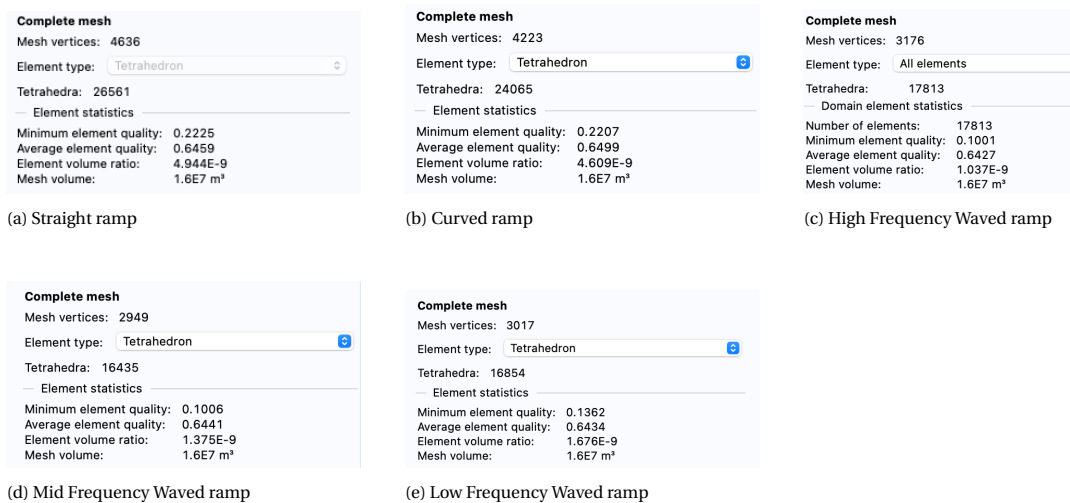
Figure I.1: Mesh elements CFD simulations ramp designs

I.1.3. Mesh Histogram

In Figures I.2a, I.2b, I.2c, I.2d and I.2e, the statistics of the mesh are shown using a histogram plot. In the histogram plot, the element quality is presented. The x-axis represents the element quality, ranging from 0 to 1. '0' represents a degenerated element and '1' represents the most optimal element quality. The y-axis represents the number of elements of similar quality. The shapes of the histograms are similar which is necessary to compare the different results.

(a) Mesh Histogram Straight

(b) Mesh Histogram Curved

(c) Mesh Histogram High Frequency Waved

(d) Mesh Histogram Mid Frequency Waved

(e) Mesh Histogram Low Frequency Waved
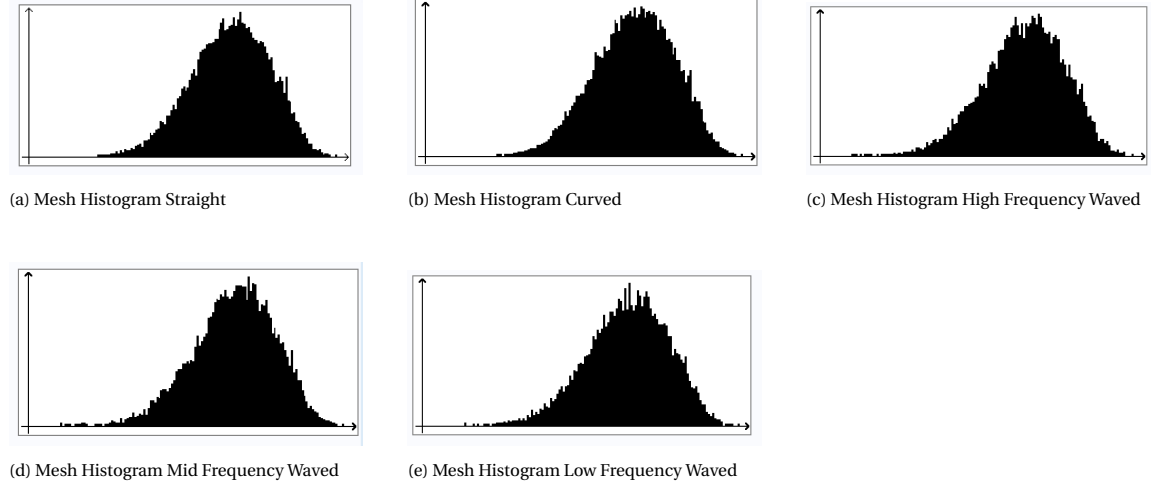
Figure I.2: Mesh Histogram CFD simulations ramp designs

I.2. Time Integration

In Table 5.3, the volume entering the inflow plane and the flow leaving the outflow plane of the ducted system are shown over time. As can be seen, there is a minimal loss of volume present in the model. The error is 1.56%, 1.83%, 0.93%, 1.82% and 2.1% for the straight, curved and high, mid & low frequency waved ramps, respectively.

Table I.1: Time Integration Volume Check - Scaling Up CFD Simulations

Factor	Volume in [m_3/s]	Volume Out [m_3/s]	Error
Straight	3.91	3.85	1.56%
Curved	3.89	3.82	1.83%
High frequency Waved	3.95	3.92	0.93%
Mid frequency Waved	3.92	3.85	1.82%
Low frequency Waved	3.90	3.82	2.1%

I.3. Convergence Plot

I.3.1. Convergence Plot 1

In Figures I.3a, I.3b, I.3c, I.3d and I.3e, the converging plots are shown for the five simulations. The x-axis represents the time step of the simulation. The y-axis represents the reciprocal of the time step, which is one divided by the time step size. A convergence plot with decreasing reciprocal of the time step, indicates that the time steps increases. This entails that the simulation converges well. The last reciprocal of step size is between $\pm 10^{-1}$ and 10^{0}. The simulation converges well as the time steps increase, and thus the reciprocal of the time step decreases, over time and therefore, the accuracy of the simulations is acceptable.
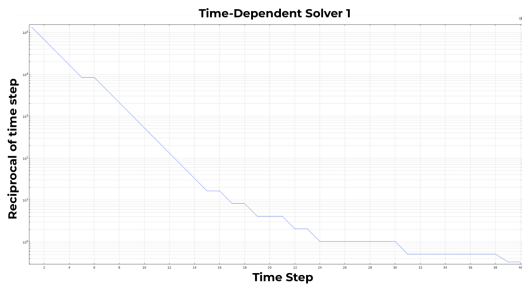
(a) Convergence Plot 1 Straight
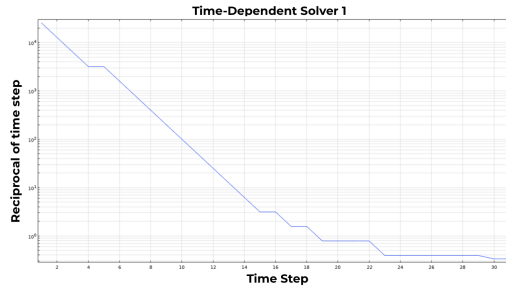
(b) Convergence Plot 1 Curved
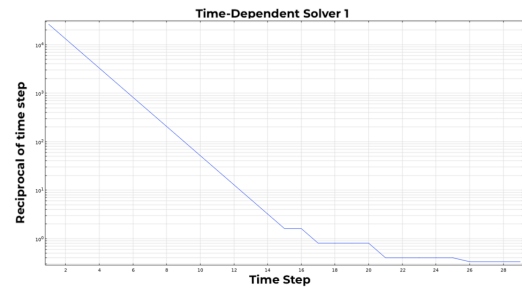
(c) Convergence Plot 1 high Frequency Waved
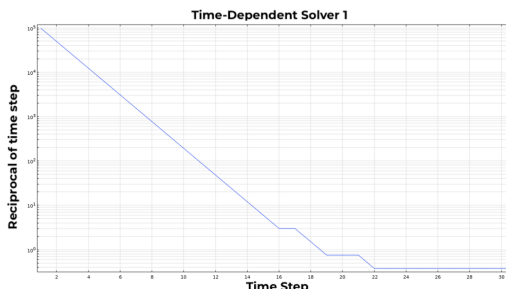
(d) Convergence Plot 1 Mid Frequency waved
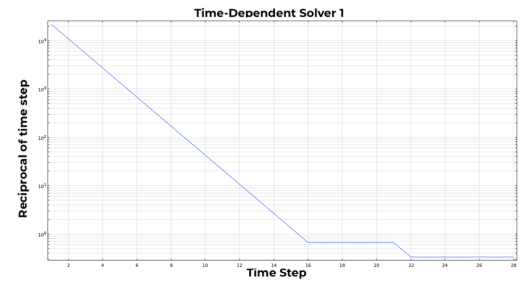
(e) Convergence Plot 1 Low Frequency waved

Figure I.3: Convergence plot 1 CFD simulations ramp designs

I.3.2. Convergence Plot 2

In Figures I.4a, I.4b, I.4c, I.4d and I.4e, the segregated solver plots are shown of the five simulations. A segregated solver solves all the unknown parameters separate. Hence, the problem is subdivided into the velocity u, u2, pressure p, p2 and the turbulence variables. This results in less required memory to solve the problem. For the last iteration numbers, the error is between $\pm 10^{-5}$ and 10^{-2}. The simulation converges well and therefore, the accuracy of the simulations is acceptable.
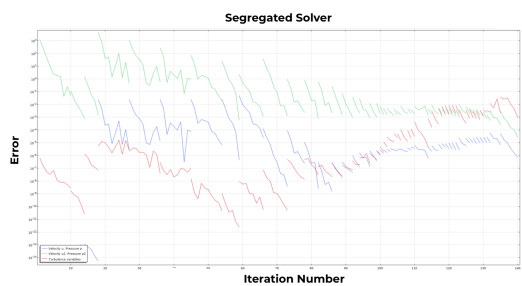
(a) Convergence Plot 2 Straight
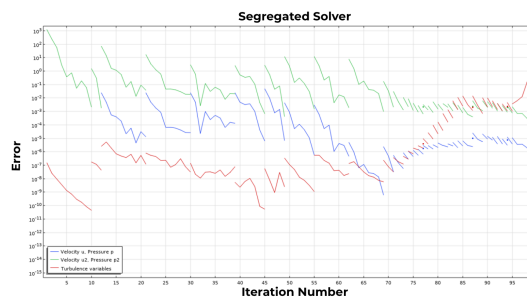
(b) Convergence Plot 2 Curved
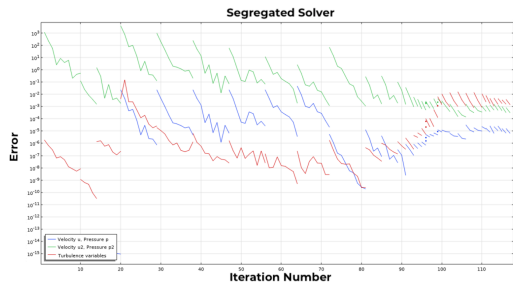
(c) Convergence Plot 2 High Frequency waved
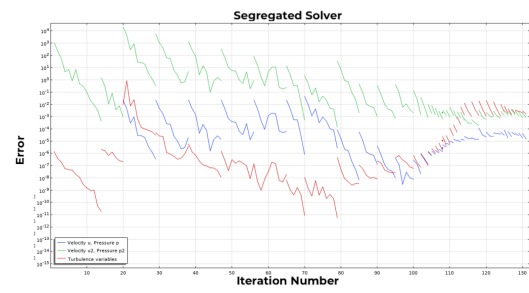
(d) Convergence Plot 2 Mid Frequency waved
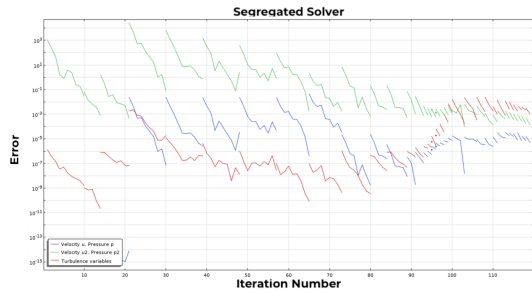
(e) Convergence Plot 2 Low Frequency waved

Figure I.4: Convergence plot 2 CFD simulations ramp designs

J

Accuracy Scaling Up Simulations

J.1. Mesh

A mesh covers a given shape or form, and subdivides it into non-overlapping elements. Functions are assigned to the specific elements. These functions can be calculated for the entire model by assembling the collection of all elements. The block in represents the turbulent water flow and the inner geometry represents the "Van Rompay Turbine".

J.1.1. Mesh Size

In Figure J.1a, J.1b and J.1c, the mesh of the three simulations are shown. As can be seen, the mesh of the block is coarser than the mesh of the inner geometry. Note that the air chamber isn't modelled. The difference in mesh size is due to the fact that hydrodynamic behaviour close to the Van Rompay Turbine is more of interest and therefore it should be calculated with more accuracy.

| (a) Mesh Factor 1 | (b) Mesh Factor 2 | (c) Mesh Factor 10 |
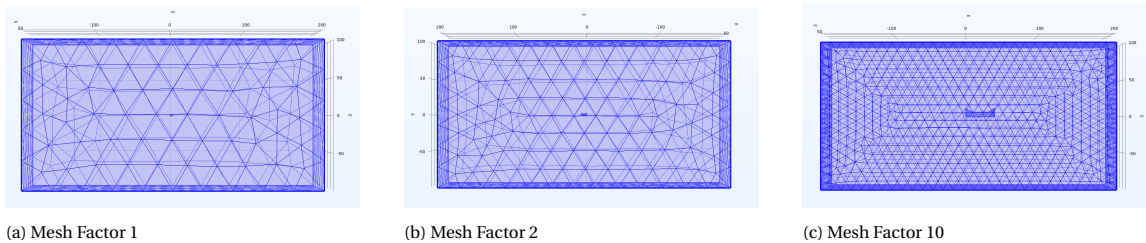
Figure J.1: Mesh size scaled up turbines CFD simulations

In Table J.1, an overview of the mesh sizes are shown for each simulation.

Table J.1: Mesh Size Scaling Up CFD Simulations

Factor	Turbine Mesh Size	Block Mesh Size
Factor 1	Fine	Normal
Factor 2	Finer	Normal
Factor 10	Extra Fine	Normal

J.1.2. Mesh Elements

In Figure J.2a, J.2b and J.2c, the information about the elements is presented. The minimum element quality is ±0.2225, ±0.1952 and ±0.0.1851 for the factor 1, factor 2 and factor 10 simulations, respectively. This is sufficient as the rule of thumb says that a minimum element quality of at least 0.1 is necessary.

Complete mesh
Mesh vertices: 4636
Element type: Tetrahedron
Tetrahedra: 26561
— Element statistics
Minimum element quality: 0.2225
Average element quality: 0.6459
Element volume ratio: 4.944E-9
Mesh volume: 1.6E7 m³

Partial mesh
Mesh vertices: 5416
Element type: Tetrahedron
Tetrahedra: 28982
— Element statistics
Minimum element quality: 0.1952
Average element quality: 0.6496
Element volume ratio: 8.399E-8
Mesh volume: 1.6E7 m³

Complete mesh
Mesh vertices: 22402
Element type: Tetrahedron
Tetrahedra: 126777
— Element statistics
Minimum element quality: 0.1851
Average element quality: 0.6576
Element volume ratio: 1.015E-4
Mesh volume: 1.6E7 m³

(a) Mesh Elements Factor 1   (b) Mesh Elements Factor 2   (c) Mesh Elements Factor 10

Figure J.2: Mesh Elements scaled up turbines CFD simulations

J.1.3. Mesh Histogram

In Figure J.3a, J.3b and J.3c,the statistics of the mesh are shown using a histogram plot. In the histogram plot, the element quality is presented. The x-axis represents the element quality, ranging from 0 to 1. '0' represents a degenerated element and '1' represents the most optimal element quality. The y-axis represents the number of elements of similar quality. The shapes of the histograms are similar which is necessary to compare the different results.

(a) Mesh Histogram Factor 1   (b) Mesh Histogram Factor 2   (c) Mesh Histogram Factor 10
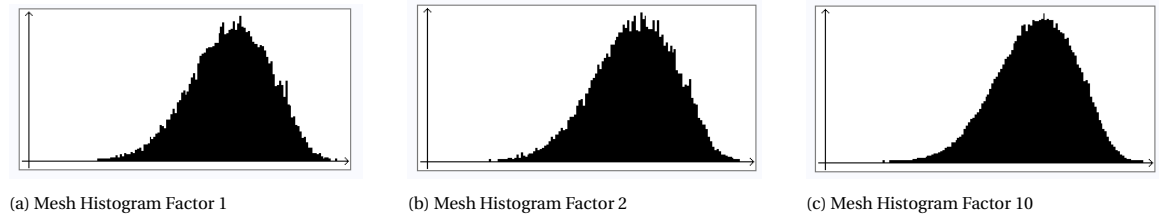
Figure J.3: Mesh Histogram scaled up turbines CFD simulations

J.2. Time Integration

In Table J.2, the volume entering the inflow plane and the flow leaving the outflow plane of the ducted system are shown over time. As can be seen, there is a minimal loss of volume present in the model. The error is 1.56%, 2.05% and 3.80% for the scaling factor 1, 2 & 10, respectively.

Table J.2: Time Integration Volume Check - Scaling Up CFD Simulations

Factor	Volume in [m$_3$/s]	Volume Out [m$_3$/s]	Error
Factor 1	3.91	3.85	1.56%
Factor 2	15.43	15.12	2.05%
Factor 10	377.89	364.06	3.80%

J.3. Convergence Plot

J.3.1. Convergence Plot 1

In Figure J.4a, J.4b and J.4c, the converging plots are shown for the five simulations. The x-axis represents the time step of the simulation. The y-axis represents the reciprocal of the time step, which is one divided by the time step size. A convergence plot with decreasing reciprocal of the time step, indicates that the time steps increases. This entails that the simulation converges well. The last reciprocal of step size is between $\pm 10^{-1}$ and 10^0. The simulation converges well as the time steps increase over time and therefore, the accuracy of the simulations is acceptable.
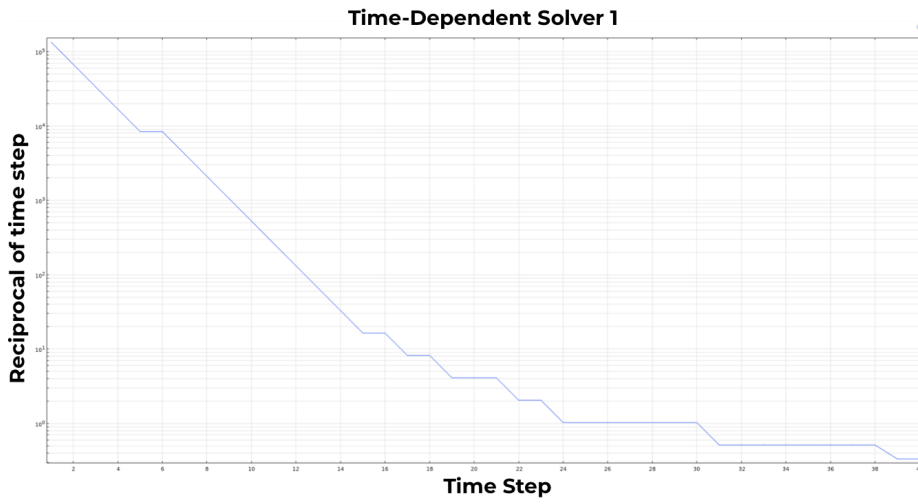
(a) Convergence Plot 1 Factor 1
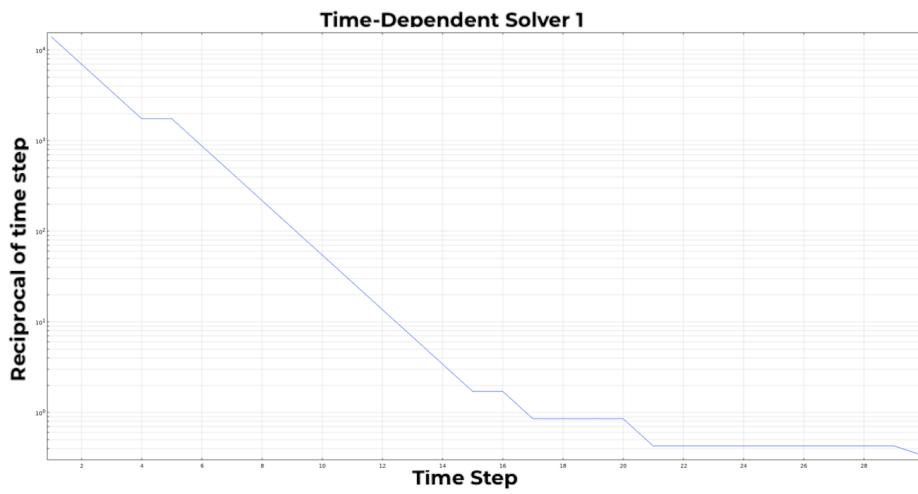
(b) Convergence Plot 1 Factor 2
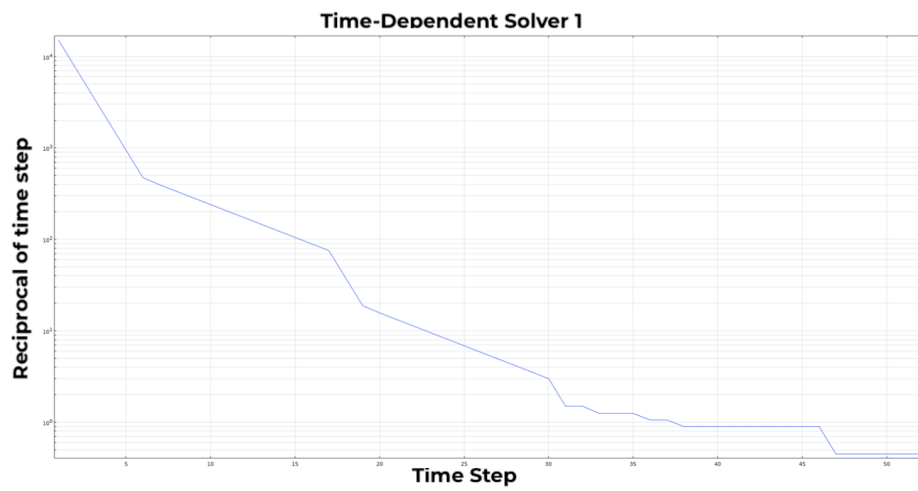
(c) Convergence Plot 1 Factor 10

Figure J.4: Convergence Plot 1 scaled up turbines CFD simulations

J.3.2. Convergence Plot 2

In Figure J.5a, J.5b and J.5c, the segregated solver plots are shown of the five simulations. A segregated solver solves all the unknown parameters separate. Hence, the problem is subdivided into the velocity u, u2, pressure p, p2 and the turbulence variables. This results in less required memory to solve the problem. For the last iteration numbers, the error is between $\pm 10^{-5}$ and 10^{-2}. The simulation converges well and therefore, the accuracy of the simulations is acceptable.
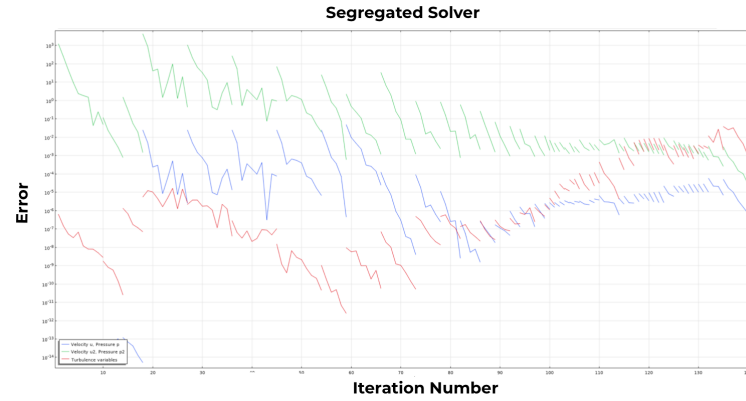
(a) Convergence Plot 2 Factor 1
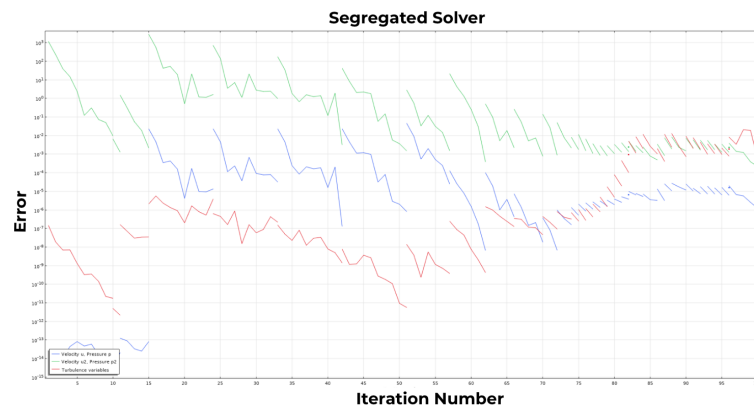
(b) Convergence Plot 2 Factor 2
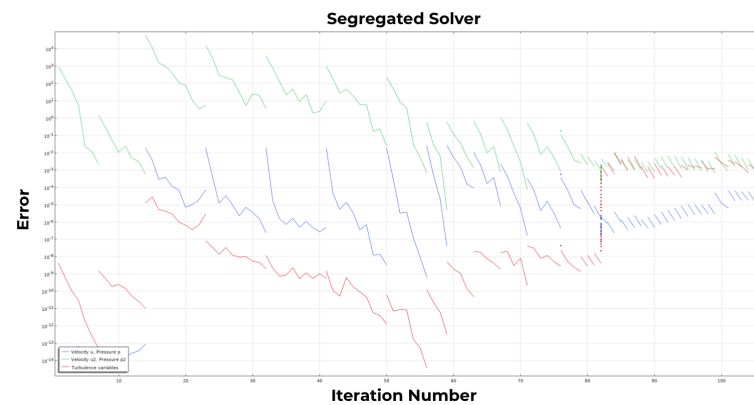
(c) Convergence Plot 2 Factor 10

Figure J.5: Convergence Plot 2 scaled up turbines CFD simulations

K

Streamwise Wavy Walls

Streamwise wavy walls are designed and attached to the straight inflow ramp to minimise the turbulence levels in the inflow of the turbine. This choice is based on prior literature where an experimental investigation of the flow over large-scale wavy walls was performed (Hamed et al., 2015).

The Mechanism of drag reduction is illustrated in Figure K.1 and is described by Tomiyama and Fukagata in 2013. Tomiyama and Fukagata in 2013 found that the induced flow caused by the wavy motion creates a pumping effect close to the wall: above the trough, a strong flow is induced in the same direction as the travelling flow; above the crest, a weaker flow is induced in the opposite direction. This pumping effect causes that the quasi-streamwise vortices are removed from the wall and therefore weakened. These weakened vortices produces less shear stresses which results in a drag reduction (Tomiyama and Fukagata, 2013).
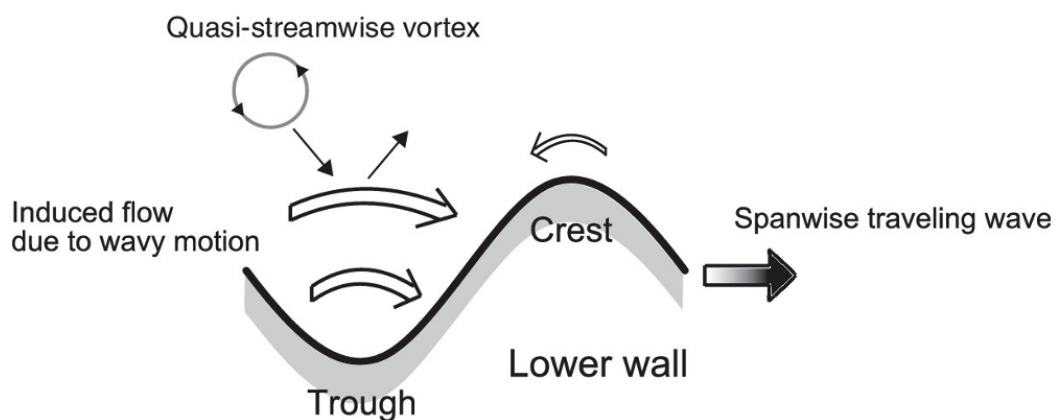
Figure K.1: Schematic of the mechanism of drag reduction due to the spanwise traveling wave-like wall deformation